

ABSTRACT

Title of dissertation: ENGINEERING TOPOLOGICAL MATTER
WITH ULTRA-COLD ATOMS

Ana Valdés-Curiel,
Doctor of Philosophy, 2019

Dissertation directed by: Professor Ian Spielman
Joint Quantum Institute,
National Institute of Standards and Technology and
University of Maryland College Park

This thesis describes some of the work I did. It doesn't include work I didn't do. It mentions some of the work I had others do for me and finally some of the work others had me do for them.

EGINEERING TOPOLOGICAL MATTER WITH ULTA-COLD
ATOMS

by

Ana Valdés Curiel

Dissertation submitted to the Faculty of the Graduate School of the
University of Maryland, College Park in partial fulfillment
of the requirements for the degree of
Doctor of Philosophy
2019

Advisory Committee:
Dr. Ian Spielman, Advisor
Rattata, cites Meowth
Meowth, cites Pikachu
Squirtle, cites self
Pikachu, cites Meowth

© Copyright by
Ana Valdés Curiel
2019

Preface

Lapras

Foreword

Farfetch'd

Dedication

Clefairy

Acknowledgments

Charmander

Table of Contents

List of Figures	ix
List of Abbreviations	xiv
1 Introduction	1
1.1 Thesis overview	1
2 Basic theory of Bose-Einstein condensation	3
2.1 The Bose-Einstein distribution	3
2.2 BEC transition and critical temperature	3
2.3 BEC in a harmonic potential	3
2.4 BEC with interactions	3
2.4.1 GPE equation	3
2.4.2 Thomas-Fermi approximation	3
2.4.3 Expansion of atomic cloud in 3D harmonic potential	3
3 The Rubidium Lithium apparatus	4
3.1 Laser systems	4
3.1.1 Master and cooling laser systems	4
3.1.2 1064nm laser system	4
3.1.3 Raman laser system	4
3.1.3.1 Tapered amplifier laser system	4
3.1.3.2 Ti:Saphire and 532 nm laser system	4
3.2 Imaging systems	4
3.2.1 The xy imaging system	4
3.2.2 The zx imaging system	4
3.2.3 Measuring magnification and focus?	4
3.3 Water cooling	4
3.4 Magnetic field control	4
3.4.1 Bias coils	4
3.4.2 Gradient cancelation coils	4
3.5 RF electronics	4

3.5.1	RF evaporation antenna	4
3.5.2	High power RF antenna	4
3.6	Microwave electronics	5
3.7	Computer control and data acquisition	5
3.8	Experimental sequence to make BECs	5
4	Manipulation and detection of ultra-cold atoms	6
4.1	Electronic structure of ^{87}Rb	6
4.2	Magnetic interaction	7
4.2.1	Static magnetic fields	7
4.2.2	Oscillatory magnetic fields	7
4.2.3	Selection rules	7
4.3	Applications	7
4.3.1	Quantum coherent dynamics?	7
4.3.2	Adiabatic rapid passage	7
4.3.3	The Rabi cycle	7
4.3.4	Ramsey interferometry	7
4.4	Atom-light interaction	7
4.4.1	Light induced spin-orbit coupling	8
4.5	Rashba SOC in condensed matter	8
4.6	Absorption imaging	8
4.6.1	Time of flight imaging	8
4.6.2	Partial transfer absorption imaging: magnetic field stabilization	8
4.7	Floquet	8
5	Fourier Transform Spectroscopy	9
5.1	Operating principle of Fourier spectroscopy	10
5.2	Measuring the SOC dispersion with Fourier transform spectroscopy .	11
5.2.1	System	11
5.2.2	Tunable SOC	13
5.2.3	Application of Fourier spectroscopy	14
5.2.4	Effective mass	15
5.2.5	Measured dispersion	17
6	Synthetic clock transitions through continuous dynamical decoupling	23
6.1	Basic principles of CDD	24
6.2	CDD of a spin-1 system	24
6.3	The $ xyz\rangle$ states	25
6.3.1	State decomposition	25
6.3.2	Energies	26
6.3.3	Transition matrix elements	27
6.4	$ xyz\rangle$ state preparation	27
6.5	Initial characterization of Ω	29
6.6	Spectroscopy	30
6.7	Robustness	31

6.7.1	Optimal response to noise	32
6.8	Driving dressed state transitions	32
6.9	Concatenated CDD	33
6.10	Conclusions	37
7	Topological order in quantum systems	39
7.1	Topology in mathematics	39
7.2	Topological order in condensed matter	40
7.3	Berry phase and Berry curvature	42
7.3.1	Aharonov-Bohm phase as an example of a Berry's phase	43
7.3.2	Chern number	44
7.4	The bulk-edge correspondence principle	45
7.5	Example: two-level model	46
7.6	Monopoles and Dirac strings	47
7.7	Conclusions	48
8	Unconventional topology with a Rashba SOC quantum gas	49
8.1	Rashba spin-orbit coupling	50
8.2	Rashba SOC for neutral atoms	51
8.3	Experimental implementation of Rashba SOC	53
8.3.1	Raman coupling the $ xyz\rangle$ states	54
8.3.1.1	Floquet and off resonant coupling effects	55
8.3.1.2	Lifetime	56
8.3.2	Measuring quasimomentum distributions	57
8.3.2.1	Correcting shears from gradients	58
8.4	Fourier spectroscopy of the Rashba dispersion	59
8.5	Quantum state tomography with Ramsey interferometer	61
8.5.1	Wave function evolution in Ramsey interferometer	63
8.5.2	Combining phases from different measurements	66
8.5.3	Measuring the topological index	67
8.6	Conclusion	67
9	Conclusions and outlook	70
9	Realization of a fractional period adiabatic superlattice	71
A	Full derivation of the Hamiltonian for Raman coupled $ xyz\rangle$ states	72
B	New Apparatus	73
B.1	Water cooling stuff	73
B.2	Electrical installation	73
B.3	New Rb 'oven'	73
	Bibliography	75

List of Figures

5.1 a. Eigenenergies of a three-level system described by $\hat{H}'(\Omega_1, \Omega_2, \Omega_3)$.
 b. The system is prepared in $|\psi_2\rangle$ and subjected to \hat{H}' at time t_i . The three panels show the occupation probabilities of the states $|\psi_1\rangle$ (blue), $|\psi_2\rangle$ (black), and $|\psi_3\rangle$ (red) in the measurement basis, for evolution times up to t_f . c. Power spectral density of the occupation probabilities from panel b. The three peaks in the Fourier spectra correspond to the energy differences present in panel a. 10

5.2 a. Setup. A bias magnetic field $B_0\mathbf{e}_z$, with $B_0 = 1.9893$ mT splits the hyperfine energy levels of the $f = 1$ manifold of ^{87}Rb by $\omega_Z/2\pi = 14$ MHz. A pair of cross polarized Raman beams propagating along $\mathbf{e}_x + \mathbf{e}_y$ and $\mathbf{e}_x - \mathbf{e}_y$ couple the atoms' momentum and spin states. b. The Raman frequencies are set to $\omega_A = \omega_L + \delta$ and $\omega_B = \omega_L + \omega_Z$. We add frequency sidebands to ω_B , separated by $\pm\delta\omega$. The amplitude modulation from the interference between the multiple frequency components results in tunable SOC. c. SOC dispersion for Raman coupling strength $\Omega_0 = 12E_L$ and $\Omega = 0$, on four photon resonance. 12

5.3 a. Floquet quasi-energies of a three level Hamiltonian with SOC and time periodic coupling strength. The quasi-energies are grouped into manifolds consisting of three levels that get repeated with a periodicity equal to $\hbar\delta\omega$. b. Energy differences of the Floquet quasi-energies. Each color represents the energy difference, separated by a fixed number of neighboring levels. When the number of neighboring levels is a multiple of 3, the energy differences are straight lines, a result of the periodic structure of the Floquet manifolds. 13

5.4 Oscillation of the BEC in the dipole trap along the recoil directions \mathbf{e}_x and \mathbf{e}_y for (top) bare atoms, and the three parameter regimes that we explored (i), (ii), and (iii). We believe that the observed low amplitude oscillations along \mathbf{e}_y are due to the initial detuning ramp not being fully adiabatic. 16

5.5	a. Occupation probability for the three states in the measurement basis $ m_f = -1, q = q_x + 2k_L\rangle$ (blue), $ m_f = 0, q = q_x\rangle$ (black), and $ m_f = +1, q = q_x - 2k_L\rangle$ (red), following unitary evolution under \hat{H}_{SOC} for times up to 100 μs at different spin-orbit coupling regimes: (i) $\Omega_0 = 9.9E_L$, $\Omega = 04$, $\delta = 5.8E_L$, (ii) $\Omega_0 = 0$, $\Omega = 8.6E_L$, $\delta = -0.7E_L$, $\delta\omega = \epsilon + 12E_L$, and (iii) $\Omega_0 = 1.5E_L$, $\Omega = 8.4E_L$, $\delta = -4.7E_L$, $\delta\omega = \epsilon + 17E_L$. b. Occupation probability for long pulsing up to 800 μs for parameters as in (iii). c. Power spectral density of the occupation probability. We subtract the mean value of each probability before taking the Fourier transform to remove peaks at $f = 0$. The peaks in the PSD then correspond to the relative eigenenergies of \hat{H}_{SOC} .	19
5.6	Power spectral density of the time dependent occupation probability for each state in the measurement basis for three coupling regimes: (Left) $\Omega_0 = 9.9E_L$, $\Omega = 0$, (Center) $\Omega_0 = 0$, $\Omega = 8.6E_L$, $\delta\omega = \epsilon + 12E_L$, and (Right) $\Omega_0 = 4.9E_L$, $\Omega = 8.4E_L$, $\delta\omega = \epsilon + 17E_L$. Each panel is normalized to peak amplitude to highlight small amplitude features in the PSD of the periodically driven SOC, and the highest value on the frequency axis corresponds to the FFT bandwidth.. b. Spin-dependent SOC dispersion for three different coupling regimes. We combine the PSD of the occupation probability of the states $ m_F = \pm 1, q_x = \mp 2k_L\rangle$, and shift each frequency by an amount proportional to the squared quasimomentum and the effective mass. The dashed lines are the calculated Floquet energies for the Hamiltonian using our calibration parameters.	20
5.7	Spin-dependent SOC dispersion for three different coupling regimes. We combine the PSD of the occupation probability of the states $ m_F = \pm 1, q_x = \mp 2k_L\rangle$, and shift each frequency by an amount proportional to the squared quasimomentum and the effective mass. The dashed lines are the calculated Floquet energies for the Hamiltonian using our calibration parameters.	21
5.8	a Floquet quasi-energy spectrum of a SOC Hamiltonian with periodic coupling strength. The red line represents the eigenstate that has the largest overlap with the initial $ m_F = 0\rangle$ state. The arrows indicate the energies of the states that have non-zero overlap with the initial state and can be measured with Fourier transform spectroscopy. b PSD of the occupation probability and numerically calculated energy differences between the levels indicated by the arrows on panel a. c PSD shifted by a quadratic term $-\hbar^2 q_x^2 / 2m^*$. The red box indicates the region of interest where we can recover the SOC spectrum. d We invert the frequency axis and shift it by $\delta\omega$.	22
6.1	Implementing CCD.	24
6.2	State decomposition of the $ xyz\rangle$ states	26
6.3	Experimental CCD protocol	28

6.4	Calibration of Ω	29
6.5	Spectroscopy of the $ xyz\rangle$ states	30
6.6	The $ z\rangle \rightarrow x\rangle$ transition as a function of Ω_{RF}	31
6.7	Optimal response of the zx transition	33
6.8	Coherent driving of dressed state transitions	34
6.9	Loss of contrast of coherent oscillations	35
6.10	Concatenated CDD protocol	37
6.11	Concatenated CCD	38
7.1	The quantum Hall effect	41
7.2	The Aharonov-Bohm experiment	44
7.3	Graphical representation of Chern number	46
7.4	Graphical representation of Chern number	47
7.5	Different topological invariants	48
8.1	Rashba dispersion relation	50
8.2	The Rashba ring coupling	51
8.3	Rashba ring coupling eigenenergies	52
8.4	Rashba ring coupling ground state dispersion	53
8.5	a Our engineered dispersion consisted of a two-level Rashba subspace (red and blue) with a single Dirac point linking the lowest two branches and a topologically trivial higher branch (gray). b We generated $ xyz\rangle$ states by combining a bias magnetic field along \mathbf{e}_3 with an RF magnetic field oscillating along \mathbf{e}_1 . These states were coupled by three cross-polarized Raman laser beams propagating along \mathbf{e}_1 , $\mathbf{e}_2 - \mathbf{e}_1$ and $-\mathbf{e}_1 - \mathbf{e}_2$. c Each pair of Raman lasers was in two-photon resonance with a single transition between the $ xyz\rangle$ states which we coupled strengths $(\Omega_{zx}, \Omega_{xy}, \Omega_{yz})/2\pi = (12.6(5), 8.7(8), 10(1))$ kHz.	54
8.6	Effect of neighboring Floquet manifolds on Rashba dispersion	56
8.7	Lifetime of Raman dressed states	57
8.8	Mapping momentum into quasimomentum	58
8.9	We measured the standard deviation of the momentum distribution along the axis perpendicular to the SG for 10 shots on each m_f state. From the slope of the linear fit we obtain a shearing parameter $\alpha \approx \pm 0.067$ for $m_f = \pm 1$.	59
8.10	a Fourier spectroscopy protocol. We applied the Raman lasers for a variable time t_p : a Rabi-type atomic interferometer analogous to a three-port beam splitter. b Probabilities as a function of quasimomentum for a fixed Raman pulse time $t_p = 420 \mu\text{s}$ c Dynamics of the final populations of the $ xyz\rangle$ states with quasimomentum $(q_1, q_2) = (-0.55, -0.18) \text{ k}_L$ (blue star in panels b) after initializing the system in the $ z\rangle$ state.	60

8.11 PSD of all the analyzed states as a function of q_2 for fixed $q_1 = 0.18 k_L$. The different overlaps between the initial state, the Raman dressed states and the measured final state result in peaks with different amplitudes.	61
8.12 a Predicted dispersion relation as a function of q_2 for fixed $q_1 = -0.09 k_L$ (left) and $0.65 k_L$ (right), computed for the experiment parameters. The energy differences between the branches enclosing the vertical arrows appear as peaks in the spectral maps below. b Power spectral density (PSD) for the same parameters as above which we obtained by Fourier transforming the populations in the $ xyz\rangle$ states with respect to t_p . The dashed lines correspond to the energy differences computed using the dispersion curves on the top panel.	62
8.13 Experimental protocol for three-arm Ramsey interferometer (not to scale). (Top) We started with atoms in state $ z, y, \mathbf{q}_i = \mathbf{k} + \mathbf{k}_j\rangle$ and with detuning $\delta_y = \pm 5 E_L$ and $\delta_z = \pm 5 E_L$. We ramped the Raman lasers on in $750 \mu s$ and then ramped the detuning to nominally zero. We let the system evolve in the dark for times between $5 \mu s$ and $400 \mu s$, followed by a $25 \mu s$ Raman pulse. (Bottom) The implemented experimental protocol was equivalent to a three-arm interferometer that split an initial state into three final states with amplitudes related to the initial wave function phases.	63
8.14 Dragging the Dirac point through the atoms	64
8.15 a Probabilities as a function of quasimomentum for the three output ports of the interferometer at $t_{\text{free}} = 160 \mu s$ b Probabilities as a function of free evolution time t_{free} for an input state with quasimomentum $(q_1, q_2) = (0.55, -0.92) k_L$ indicated by the blue star on a and in the topological ground branch ($n = 1$)	65
8.16 Weight arrays used for combination of interferometer phases	66
8.17 Topological invariants from quantum state tomography, for the non-topological branch ($n = 3$, left) and the topological branch ($n = 1$, right). a Phase differences as a function of quasimomentum from the the $z \rightarrow x$ transition b Phase differences as a function of polar angle for a loop radius $0.77 k_L$ from the $z \rightarrow x$ (top), $x \rightarrow y$ (middle) and $y \rightarrow z$ (bottom) transitions. The phases associated to the topological branch are characterized by two π valued discontinuities. Each row of phases was shifted by a constant value so that the three rows of phases share the same vertical axis. All phases shown here were binned and averaged using the fit uncertainties as weights. c Inferred Chern number as a function of loop radius. For loops with $q > 0.4 k_L$ we obtained an integrated Berry phase and asymptotic Chern number of $\Phi_B/2\pi = 0.01(1)$ for the non-topological branch and $\Phi_B/2\pi = 0.5(5)$ for the topological branch.	69

B.1	a Probabilities as a function of quasimomentum for the three output ports of the interferometer at $t_{\text{free}} = 160 \mu\text{s}$ b Probabilities as a function of free evolution time t_{free} for an input state with quasimomentum $(q_1, q_2) = (0.55, -0.92) k_L$ indicated by the blue star on a and in the topological ground branch ($n = 1$)	73
B.2	a Probabilities as a function of quasimomentum for the three output ports of the interferometer at $t_{\text{free}} = 160 \mu\text{s}$ b Probabilities as a function of free evolution time t_{free} for an input state with quasimomentum $(q_1, q_2) = (0.55, -0.92) k_L$ indicated by the blue star on a and in the topological ground branch ($n = 1$)	74

List of Abbreviations

α alpha
 β beta

NIST National Institute of Standards and Technology
JQI Joint Quantum Institute

Chapter 1: Introduction

Why is quantum simulation important:

- Can help understand problems that are not easy to solve numerically or analytically. High temperature superconductors, frustrated systems, as good examples.
- Create analogues to systems that would otherwise not be possible to study. Example: the expanding universe, Hofstadter at large magnetic fields.
- Create new exotic systems that do not exist in nature but can help us learn or understand something... or are just fun!

Don't forget to talk about topology! It starts with condensed matter but has been relevant to many other systems. Many Nobel prizes awarded, many applications and potential applications found.

Start with topology and move into quantum simulation? Or the other way around?

1.1 Thesis overview

In Chapters 2 and 3 I will describe the basic theory of Bose-Einstein condensation and the technical details of our experimental apparatus that produces ^{87}Rb BECs. In Chapter 4 I will describe our quantum simulation toolkit, the standard techniques that we use to manipulate and detect ensembles of ultracold atoms that are necessary for all of our experiments. Chapter 5 describes a Fourier transform spectroscopy technique that exploits the relation between quantum coherent evolution and the underlying spectrum of a system and that was used to characterize experiments described later in the thesis. Chapter 6 describes an implementation of continuous dynamical decoupling that helped to both make our system more robust against environmental noise and also allowed us to couple the internal states of the atoms in new ways that were not possible before, opening the path for new kinds of quantum simulations described in Chapters 7 and 8. In Chapter 8 I describe the experimental realization of Rashba spin-orbit coupling for a quantum system without a crystalline structure and has unconventional topology characterized by non-integer topological invariants. Finally, Chapter 8 describes the experimental implementation of a fractional period adiabatic superlattice, an intermediate step

necessary for us to generate Hofstadter cylinders with non-zero magnetic flux in the future.

Appendix are experiments that I contributed to but are not included in the thesis. Also things related to new apparatus?

Chapter 2: Basic theory of Bose-Einstein condensation

2.1 The Bose-Einstein distribution

2.2 BEC transition and critical temperature

2.3 BEC in a harmonic potential

2.4 BEC with interactions

2.4.1 GPE equation

2.4.2 Thomas-Fermi approximation

Why the BEC has the shape of an inverted parabola.

2.4.3 Expansion of atomic cloud in 3D harmonic potential

How one can infer atomic densities and temperature (from thermal atoms) from time of flight images.

Chapter 3: The Rubidium Lithium apparatus

3.1 Laser systems

3.1.1 Master and cooling laser systems

3.1.2 1064nm laser system

3.1.3 Raman laser system

3.1.3.1 Tapered amplifier laser system

3.1.3.2 Ti:Saphire and 532 nm laser system

3.2 Imaging systems

3.2.1 The xy imaging system

3.2.2 The zx imaging system

3.2.3 Measuring magnification and focus?

3.3 Water cooling

3.4 Magnetic field control

3.4.1 Bias coils

3.4.2 Gradient cancelation coils

3.5 RF electronics

3.5.1 RF evaporation antenna

3.5.2 High power RF antenna

The antenna loop is Digikey part number 732 – 5646 – ND

3.6 Microwave electronics

We

3.7 Computer control and data acquisition

Cite labscrip.

3.8 Experimental sequence to make BECs

Chapter 4: Manipulation and detection of ultra-cold atoms

All of our experiments rely on the interaction of atoms with electric and magnetic fields, both for the preparation of ultra-cold atoms through laser cooling and trapping, for the engineering of interesting Hamiltonians, and for detection. In this chapter I will first describe the electronic structure of ^{87}Rb which makes all of our experiments possible and then I will review the effects of the magnetic and electric interactions that are relevant to our experiments. I will not cover laser cooling which has been covered extensively in the literature (see [1] for example).

4.1 Electronic structure of ^{87}Rb

Rb is an Alkali metal (also Li , which exists in our vacuum chamber but was never used). Alkali metals correspond to the first group (leftmost column) of the periodic table and are characterized by having a single valence electron, which makes the description of their internal structure much simpler than that of other elements. In general we can describe the state of an electron in an atom by its angular momentum \mathbf{L} and its spin \mathbf{S} . Because of Pauli's exclusion principle there can not be two electrons with the same quantum numbers and in multi-electron atoms they tend to fill 'shells' of different angular momentum values, historically labeled by the letters S , P , D , F , ...¹ (corresponding to $\mathbf{L} = 1, 2, 3, 4, \dots$). In particular Rb has 4 filled shells and one electron in the $5S$ shell (the number 5 corresponds to the principal quantum number). Figure ??a shows the energy levels of a $5S$ and $5P$ orbital.

The atomic level structure is modified by a fine structure splitting of the electronic orbitals into levels with different total electronic angular momentum $\mathbf{J} = \mathbf{L} + \mathbf{S}$. This effect arises from a spin-orbit interaction between the electron's spin and orbital angular momentum $\hat{H}_{fs} \propto \mathbf{L} \cdot \mathbf{S}$. Figure ??b show the $5^2S_{1/2}$, $5^2P_{1/2}$ and $5^2P_{3/2}$ electronic configurations that arise from this splitting. The atomic level structure gets further modified by the nuclear spin \mathbf{I} which interacts with the electron's intrinsic magnetic flux density through the magnetic dipole interaction to give rise to the hyperfine splitting. For S electrons the hyperfine splitting can be described by the Hamiltonian $\hat{H}_{hfs} = A_{hfs} \mathbf{I} \cdot \mathbf{J}$ ². Figure ??c shows the fine structure getting further split into states of total angular momentum $\mathbf{F} = \mathbf{J} + \mathbf{I}$. ^{87}Rb has

¹This terms were used to describe the lines in the emission spectra when they were first discovered. S stands for sharp, P for principal D for diffuse and F for further noted

²Notice how both the fine and hyperfine structure arise from a spin-orbit coupling interaction, we will discuss a very different type of spin-orbit coupling in future chapter.

a nuclear spin $I = 3/2$ and therefore its ground state hyperfine configuration has $F = 1$ and $F = 2$.

[Something about what we use this transitions for and how we usually ignore all other levels. (???)]

[TODO: what about matrix elements between -1 and +1?. Move to intro chapter]

4.2 Magnetic interaction

4.2.1 Static magnetic fields

Also talk about the Paschen–Back effect occurs in a strong external magnetic field. The spin and orbital angular momentum precess independently about the magnetic field.

Uniform fields: Zeeman splitting, Breit-Rabi formula Gradients: Quadrupole potentials and Stern-Gerlach

4.2.2 Oscillatory magnetic fields

RF coupling and microwave coupling

4.2.3 Selection rules

4.3 Applications

4.3.1 Quantum coherent dynamics?

4.3.2 Adiabatic rapid passage

4.3.3 The Rabi cycle

4.3.4 Ramsey interferometry

4.4 Atom-light interaction

In the presence of an electric field \mathbf{E} an atom can become polarized and therefore it's energy levels get shifted through the Stark effect [2]. If the electric field is spatially uniform with respect to the atom's size the effect of the electric field on the atom can be described by the the Hamiltonian

$$\hat{H} = -\hat{\mathbf{d}} \cdot \mathbf{E}, \quad (4.1)$$

where $\hat{\mathbf{d}} = -e \sum_j \hat{r}_j$ is the atomic dipole operator, e is the electron charge and \hat{r}_j are the position operators of the atom's electrons relative to the center of mass of the atom. This approximation, known as the dipole approximation, treats the atom as a quantum object and the electric field as a classical object. Here I will only

consider the case of oscillating electric fields $\mathbf{E} = E_0 \cos(\omega t) \boldsymbol{\epsilon}$ (i.e. plane waves of electromagnetic radiation) which are relevant to our experiments.

Can break interaction into scalar, vector and tensor part. Interaction can also be resonant or off-resonant.

[Why do you only get second order perturbation theory effects? I think it has something to do with unperturbed atomic states being eigenstates of the parity operator]

4.4.1 Light induced spin-orbit coupling

The geometry and wavelength of the Raman fields determine the natural units of the system: the single photon recoil momentum $k_L = \sqrt{2\pi}/\lambda_R$ and its associated recoil energy $E_L = \hbar^2 k_L^2 / 2m$, as well as the direction of the recoil momentum $\mathbf{k}_L = k_L \mathbf{e}_x$. The Raman wavelength was $\lambda_R = 790.032$ nm, as usual, so that the scalar light shift is zero.

4.5 Rashba SOC in condensed matter

4.6 Absorption imaging

4.6.1 Time of flight imaging

4.6.2 Partial transfer absorption imaging: magnetic field stabilization

We then apply a pair of $250\mu\text{s}$ microwave pulses that each transfer a small fraction of atoms into the $5^2\text{S}_{1/2}, f = 2$ manifold that we use to monitor and stabilize the bias field [3]. The microwave pulses are detuned by ± 2 kHz from the $|f = 1, m_F = 0\rangle \leftrightarrow |f = 2, m_F = 1\rangle$ transition and spaced in time by 33 ms (two periods of 60 Hz). We imaged the transferred atoms following each pulse using absorption imaging³, and count the total number of atoms n_1 and n_2 transferred by each pulse. The imbalance in these atom numbers $(n_1 - n_2)/(n_1 + n_2)$ leads to a 4 kHz wide error signal that we use both to monitor the magnetic field before each spectroscopy measurement and cancel longterm drifts in the field.

4.7 Floquet

How to treat systems when RWA is not valid and how to create new effective (stroboscopic) Hamiltonians.

³We did not apply repump light during this imaging, so the untransferred atoms in the $f = 1$ manifold were largely undisturbed by the imaging process.

Chapter 5: Fourier Transform Spectroscopy

The idea of using Fourier transform spectroscopy was born from a very different natured project. The project was originally conceived as a way to engineer tunable spin-orbit coupling using multiple-tone Raman transitions. The inspiration came from a previous project where we used multiple-tone Raman transitions to engineer a spin-1 spin-orbit coupled system whose ground state presented different magnetic phases [4]. Fourier spectroscopy was conceived as a new way to characterize the tunable dispersion relation resulting from our proposed coupling scheme. Unfortunately, we realized that this proposal was equivalent to another experiment that achieved tunable SOC using amplitude modulated Raman coupling [5]. We therefore decided to focus on studying Fourier spectroscopy instead, a decision that turned out to be very fruitful for our lab as we continue to use this technique to characterize the spectrum of a variety of systems to this date.

Many spectroscopy techniques in atomic physics rely on using a source of coherent electromagnetic radiation with a well known frequency that probes the internal structure of a system (atom). For example, in absorption spectroscopy [6] a coherent light source is sent through an atomic medium and if the frequency of the light is resonant with an atomic transition it will be absorbed and a reduced transmission will be measured. Other variants of spectroscopy (e.g. Rabi spectroscopy [7], spin-injection spectroscopy [8]) work under a similar principle: atoms absorb and emit photons with frequencies equal to the transition energies between internal states.

Fourier transform spectroscopy instead employs the connection between the energy spectrum of a system and its dynamics. This connection has been exploited to study the spectrum of both condensed matter [9] and cold atom systems [10,11] alike. As opposed to other techniques, Fourier spectroscopy relies only on following the unitary evolution of an initial state suddenly subjected to a Hamiltonian of interest and measuring probabilities in a basis that does not diagonalize that Hamiltonian.

The frequency resolution of Fourier transform spectroscopy is limited only by the coherent evolution timescale of the system under study and can otherwise be applied to any system. Other applications of this technique implemented in our lab that are not included in this Chapter include measuring the dispersion relation of a Rashba spin-orbit coupled gas (see Chapter 8) and the band structure of a sub-wavelength optical lattice [12].

In this Chapter I will first give a general description of the Fourier transform spectroscopy technique in Section 5.1. Then in Section 5.2 I will describe a set of experiments where we engineered a tunable spin-orbit coupled system (our original

goal) and applied Fourier transform spectroscopy . This work was published in [13].

5.1 Operating principle of Fourier spectroscopy

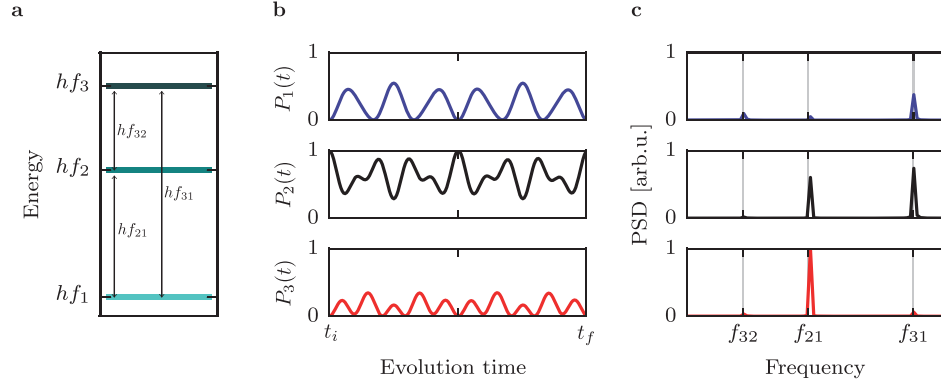


Figure 5.1: **a.** Eigenenergies of a three-level system described by $\hat{H}'(\Omega_1, \Omega_2, \Omega_3)$. **b.** The system is prepared in $|\psi_2\rangle$ and subjected to \hat{H}' at time t_i . The three panels show the occupation probabilities of the states $|\psi_1\rangle$ (blue), $|\psi_2\rangle$ (black), and $|\psi_3\rangle$ (red) in the measurement basis, for evolution times up to t_f . **c.** Power spectral density of the occupation probabilities from panel b. The three peaks in the Fourier spectra correspond to the energy differences present in panel a.

We focus on a system where we can measure the occupation probabilities of a set of orthonormal states $\{|\psi_i\rangle\}$ that fully span the accessible Hilbert space of the system. We then consider the time evolution of an arbitrary initial state $|\Psi_0\rangle = \sum_i a_i |\psi_i\rangle$ as governed by a Hamiltonian $\hat{H}'(\{\Omega_i\})$ and observe the occupation probabilities of the $\{|\psi_i\rangle\}$ states of the measurement basis as a function of time. When \hat{H}' is applied, the evolution of the initial state is $|\Psi(t)\rangle = \sum_{i,j} a_i c_{i,j} e^{-iE'_j t/\hbar} |\psi'_j\rangle$,

where E'_j and $|\psi'_j\rangle$ are the eigenenergies and eigenstates of \hat{H}' , and $c_{i,j}(t) = \langle \psi_i | \psi'_j \rangle$. The probability

$$P_k(t) = |\langle \psi_k | \Psi(t) \rangle|^2 = \left| \sum_{i,j} a_i c_{i,j} c_{j,k}^* e^{-iE'_j t/\hbar} \right|^2 \quad (5.1)$$

of finding the system in a state $|\psi_k\rangle$ of the measurement basis can be expressed as a sum of oscillatory components, with amplitude given by the magnitude of the overlap integrals between the initial state and the eigenvalues of \hat{H}'

$$P_k(t) = 1 + \sum_{i,j \neq l} 2 |a_i|^2 c_{i,j} c_{j,k} c_{i,l}^* c_{l,k} \cos(2\pi f_{j,l} t), \quad (5.2)$$

where $f_{j,l} = (E'_j - E'_l)/\hbar$ is the frequency associated with the energy difference of two eigenstates of the Hamiltonian. Fourier spectroscopy relies on measuring

the populations on each state of the measurement basis as a function of time, and extracting the different frequency components $f_{j,l}$ directly by computing the discrete Fourier transform. The bandwidth and frequency resolution of the measurement are determined by the total sampling time and the number of samples. For N samples separated by a time interval Δt , the highest resolved frequency will be $f_{\text{bw}} = 1/2\Delta t$, with resolution $\Delta f = 1/\Delta t N$. This resolution can be decreased if the Fourier transform is calculated using certain types of windowing functions that enhance signal to noise. Any higher frequency $f > f_{\text{bw}}$ will be aliased and measured in the Fourier spectrum as $f_{\text{alias}} = |f - m/\Delta t|$, where m is an integer. If interactions are present in the system, the dynamics get modified in a time scale given by the magnitude of the interactions, giving an additional constraint to the smallest frequency components of a single particle Hamiltonian that can be resolved with our technique.

Figure 5.1 illustrates the principle of Fourier spectroscopy for a three level system, initially prepared in the state $|\Psi_0\rangle = |\psi_2\rangle$, subject to the Hamiltonian

$$\hat{H}' = \begin{pmatrix} E_1 & 0 & 0 \\ 0 & E_2 & 0 \\ 0 & 0 & E_3 \end{pmatrix} + \hbar \begin{pmatrix} 0 & \Omega_1 & \Omega_2 \\ \Omega_1^* & 0 & \Omega_3 \\ \Omega_2^* & \Omega_3^* & 0 \end{pmatrix}, \quad (5.3)$$

where we measure the occupation probability as a function of time for each of the $\{|\psi_1\rangle, |\psi_2\rangle, |\psi_3\rangle\}$ states. The three eigenenergies $E'_i = hf_i$ that result from diagonalizing \hat{H}' are displayed in figure 5.1a. The three energy differences $hf_{jj'}$ between the levels determine the oscillation frequencies of the occupation probabilities, as can be seen in figure 5.1b. Finally, a plot of the power spectral densities (PSD) in figure 5.1c shows three peaks at frequencies corresponding to the three relative energies of \hat{H}' .

5.2 Measuring the SOC dispersion with Fourier transform spectroscopy

5.2.1 System

We applied the Fourier transform spectroscopy technique to measure the dispersion relation of BECs with (tunable) SOC. All of our experiments started with BECs containing about 4×10^4 atoms in the $|f = 1, m_f = -1\rangle$ hyperfine state. The experiments described in Section 5.2.3 were performed in an optical dipole trap with frequencies $(\omega_x, \omega_y, \omega_z)/2\pi = (42(3), 34(2), 133(3))$ Hz. We later modified the trapping frequencies in the xy plane to try to make them more symmetric for the experiments described in Section 5.2.4. We broke the degeneracy of the three m_F magnetic sub-levels by applying a $1.9893(3)$ mT bias field along \mathbf{e}_z that produced a $\omega_Z/2\pi = 14.000(2)$ MHz Zeeman splitting, and a quadratic Zeeman shift ϵ that shifted the energy of $|f = 1, m_F = 0\rangle$ by $-h \times 28.45$ kHz. We transferred atoms into the $|f = 1, m_F = 0\rangle$ state using ARP and then we monitored and stabilized the magnetic field using partial transfer absorption imaging as described in Chapter 4.6.2 by applying a pair of $250\ \mu\text{s}$ microwave pulses, each of them detuned by ± 2 kHz from

the $|f = 1, m_F = 0\rangle \leftrightarrow |f = 2, m_F = 1\rangle$ transition.

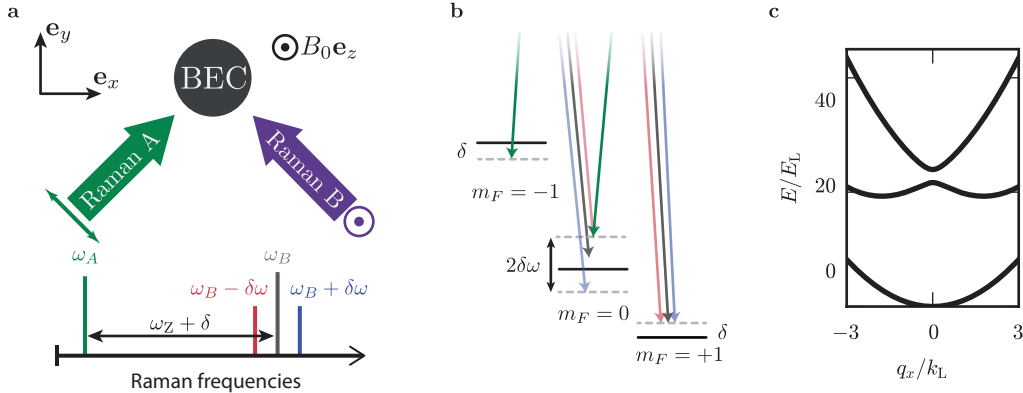


Figure 5.2: **a.** Setup. A bias magnetic field $B_0 \mathbf{e}_z$, with $B_0 = 1.9893$ mT splits the hyperfine energy levels of the $f = 1$ manifold of ^{87}Rb by $\omega_Z/2\pi = 14$ MHz. A pair of cross polarized Raman beams propagating along $\mathbf{e}_x + \mathbf{e}_y$ and $\mathbf{e}_x - \mathbf{e}_y$ couple the atoms' momentum and spin states. **b.** The Raman frequencies are set to $\omega_A = \omega_L + \delta$ and $\omega_B = \omega_L + \omega_Z$. We add frequency sidebands to ω_B , separated by $\pm \delta\omega$. The amplitude modulation from the interference between the multiple frequency components results in tunable SOC. **c.** SOC dispersion for Raman coupling strength $\Omega_0 = 12E_L$ and $\Omega = 0$, on four photon resonance.

We induced spin-orbit coupling using a pair of intersecting, cross polarized Raman laser beams propagating along $\mathbf{e}_x + \mathbf{e}_y$ and $\mathbf{e}_x - \mathbf{e}_y$, as shown in figure 5.2a and b. This beams have angular frequency $\omega_A = \omega_L + \delta$ and $\omega_B = \omega_L + \omega_Z$, where 2δ is the, experimentally controllable, detuning from four photon resonance between $m_F = -1$ and $m_F = +1$.

Our system was well described by the Hamiltonian including atom-light interaction along with the kinetic contribution

$$\hat{H}_{\text{SOC}} = \frac{\hbar^2 q_x^2}{2m} + \alpha q_x \hat{F}_z + 4E_L \hat{\mathbb{1}} + \hbar \Omega_R \hat{F}_x + (4E_L - \epsilon)(\hat{F}_z^2 - \hat{\mathbb{1}}) + \hbar \delta \hat{F}_z, \quad (5.4)$$

where q is the quasimomentum, $\hat{F}_{x,y,z}$ are the spin-1 angular momentum matrices, $\alpha = \hbar^2 k_L/m$ is the SOC strength, and Ω_R is the Raman coupling strength, proportional to the Raman laser intensity. The Raman field coupled $|m_F = 0, q = q_x\rangle$ to $|m_F = \pm 1, q = q_x \mp 2k_L\rangle$, generating a spin change of $\Delta m_F = \pm 1$ and imparting a $\mp 2k_L$ momentum. The eigenstates of \hat{H}_{SOC} are linear combinations of these states and $|m_F = 0, q = q_x\rangle$, and the set $\{|m_F, q\rangle\}$ constituted the measurement basis for Fourier transform spectroscopy.

Figure 5.2c shows a typical band structure of our spin-1 SOC system as a function of quasimomentum for a large and negative quadratic Zeeman shift $-\epsilon > 4E_L$. In this parameter regime the ground state band has a nearly harmonic dispersion

with an effective mass $m^* = \hbar^2[d^2E(k_x)/d^2x]^{-1}$, only slightly different from that of a free atom.

5.2.2 Tunable SOC

We engineered a highly tunable dispersion relation in which we can independently control the size of the gap at $q_x = 0$ as well as the SOC strength α by adding frequency sidebands to one of the Raman beams. The state of the system can change from $|m_F = -1, q = q_x + 2k_L\rangle$ to $|m_F = 1, q = q_x - 2k_L\rangle$ by absorbing a red detuned photon first followed by a blue detuned photon and vice versa, in a similar way to the Mølmer-Sørensen entangling gate in trapped ion systems [14]. When we set the angular frequencies of the sidebands to $\omega = \omega_A + \omega_Z \pm \delta\omega$, the Hamiltonian (Equation 5.4) acquired a time-dependent coupling $\Omega_R(t) = \Omega_0 + \Omega \cos(\delta\omega t)$. This periodically driven system is well described by Floquet theory [15] (see Chapter 4.7). Figure 5.3 shows the spectrum of Floquet quasi-energies for a system described by 5.4 where Ω_R oscillates with angular frequency $\delta\omega$.

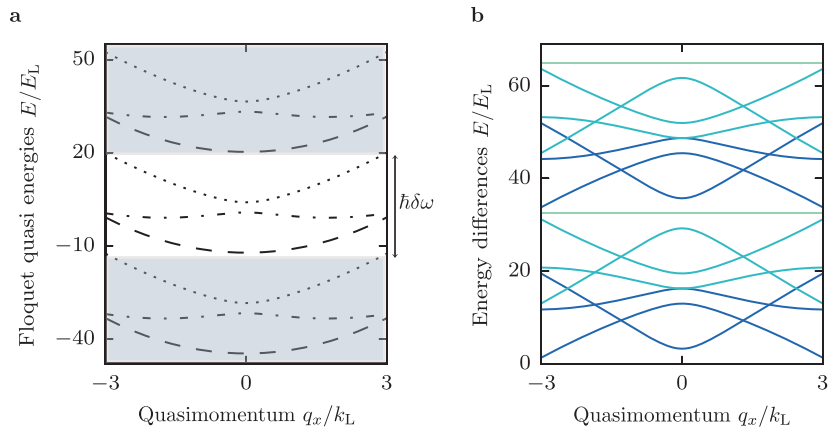


Figure 5.3: **a.** Floquet quasi-energies of a three level Hamiltonian with SOC and time periodic coupling strength. The quasi-energies are grouped into manifolds consisting of three levels that get repeated with a periodicity equal to $\hbar\delta\omega$. **b.** Energy differences of the Floquet quasi-energies. Each color represents the energy difference, separated by a fixed number of neighboring levels. When the number of neighboring levels is a multiple of 3, the energy differences are straight lines, a result of the periodic structure of the Floquet manifolds.

We defined an effective, time-independent Hamiltonian \hat{H}_{Fl} that described the evolution of the system sampled stroboscopically at an integer number of driving periods, with the time evolution operator $\hat{U}(t_0, t_0+T) = e^{-iT\hat{H}_{Fl}}$. One way of finding \hat{H}_{Fl} is to choose a clever unitary transformation $\hat{U}(t)$ such that the dynamics of the transformed wave function are described by a time independent Hamiltonian. Recall that the time evolution of a wave function in a transformed frame $|\psi'\rangle = \hat{U}^\dagger |\psi\rangle$ is given by the time dependent Schrödinger equation with a Hamiltonian

$\hat{H}' = \hat{U}^\dagger \hat{H} \hat{U} - i\hbar \hat{U}^\dagger \partial_t \hat{U}$. Here we used

$$\hat{U}(t) = \exp[-i\frac{\Omega}{\delta\omega} \sin(\delta\omega t) \hat{F}_x] \quad (5.5)$$

so that $i\hbar \hat{U}^\dagger \partial_t \hat{U} = \hbar \Omega_R(t) \hat{F}_x$. The transformed Hamiltonian $\hat{H}'(t)$ has terms proportional to $\sin(\Omega/\delta\omega \sin(\delta\omega t))$, $\sin^2(\Omega/\delta\omega \sin(\delta\omega t))$, $\cos(\Omega/\delta\omega \sin(\delta\omega t))$ and $\cos^2(\Omega/\delta\omega \sin(\delta\omega t))$ which we simplified using the Jacobi-Anger expansion for large values of θ

$$\begin{aligned} \cos(z \sin \theta) &= J_0(z) + 2 \sum_{n=1}^{\infty} J_{2n}(z) \cos(2n\theta) \approx J_0(z) \\ \sin(z \sin \theta) &= 2 \sum_{n=0}^{\infty} J_{2n+1}(z) \sin((2n+1)\theta) \approx 0, \end{aligned}$$

where J_n is the the n th order Bessel function of the first kind.

This approximation is valid for $\hbar\delta\omega > |\epsilon| + 12E_L$ and $|q_x| \leq 2k_L$ so that quasi-energy manifolds are well separated as in figure 5.3a. The Floquet Hamiltonian retained the form of Equation 5.4 with renormalized coefficients and an additional coupling term:

$$\hat{H}_{Fl} = \hat{H}_{SOC}(q, \Omega_0, \tilde{\alpha}, \tilde{\delta}, \tilde{\epsilon}) + \tilde{\Omega} \hat{F}_{xz}, \quad (5.6)$$

where $\tilde{\alpha} = J_0(\Omega/\delta\omega)\alpha$, $\tilde{\Omega} = 1/4(\epsilon + 4E_L)[J_0(2\Omega/\delta\omega) - 1]$, $\tilde{\delta} = J_0(\Omega/\delta\omega)\delta$, and $\tilde{\epsilon} = 1/4(4E_L - \epsilon) - 1/4(4E_L + 3\epsilon)J_0(2\Omega/\delta\omega)$. \hat{F}_{xz} is the $\hat{\lambda}_4$ Gell-Mann matrix that directly couples $|m_f = -1, q = q_x + 2k_L\rangle$ and $|m_f = +1, q = q_x - 2k_L\rangle$ states. The experimentally tunable parameters $\delta\omega$, Ω and Ω_0 can be used to tune the SOC dispersion.

5.2.3 Application of Fourier spectroscopy

We used Fourier transform spectroscopy to measure the spectrum of the SOC Hamiltonian (Equation 5.6) for three coupling regimes: (i) $\Omega_0 \neq 0$ and $\Omega = 0$, (ii) $\Omega_0 = 0$ and $\Omega \neq 0$ and (iii) $\Omega_0 \neq 0$ and $\Omega \neq 0$. We turned on the Raman laser non-adiabatically, in approximately 1 μ s. We let the system evolve subject to \hat{H}_{SOC} for up to 900 μ s, and then turned off the laser while releasing the atoms from the optical dipole trap. As usual, we resolved the spin and momentum distribution using Stern-Gerlach and a 21 ms TOF which allowed us to measure the fraction of atoms in each state of the measurement basis $\{|m_F, q\rangle\}$. The density of sampling points and the maximum evolution time were chosen so that the bandwidth of the Fourier transform was comparable to, or larger than, the highest frequency in the evolution of the system while maximizing resolution. Experimental decoherence resulting in loss of contrast of the oscillations, which arises from magnetic field noise and small magnetic field gradients present in our apparatus, was an additional constraint that becomes significant around 1 ms.

In order to map the full spin and momentum dependent band structure of \hat{H}_{SOC} , we measured the time dependent occupation probabilities at a fixed Raman coupling strength and different values of Raman detuning δ , for the same initial state $|m_F = 0, q_x = 0\rangle$. This detuning corresponded to the Doppler shift experienced by atoms moving relative to a light source with quasimomentum $q_x/k_L = \hbar\delta/4E_L$. We controlled the frequency and the detuning of the Raman beams using two AOMs, one of which is driven by up to three phase coherent frequencies (the carrier frequency plus two sidebands). For each of the three coupling cases that we measured, we applied the Raman beams at detuning values within the interval $\pm 12E_L$ which corresponds to quasimomentum values $\pm 3k_L$.

This approach of changing detuning rather than using atoms with non-zero quasimomentum had the advantage that the state preparation was very reliable (making BECs at rest is easy¹!) and we got very good signal to noise ratios due to the relatively high densities of the BECs. The downside is that if one is interested in looking at a large range of quasimomentum values, it takes a long time to repeat each experiment for different detuning values. In future experiments where we used Fourier transform spectroscopy we sacrificed some signal to noise for speed and used the momentum distribution of non-condensed atoms to parallelize our measurements.

5.2.4 Effective mass

Fourier transform spectroscopy only gives access to the relative energies of a Hamiltonian. If we want to recover the absolute energies we need to have an additional energy reference. For this particular set of experiments we had a ground state with a nearly quadratic dispersion and we could measure its effective mass which allowed us to obtain such reference.

We measured the effective mass of the Raman dressed atoms by adiabatically preparing the BEC in the lowest eigenstate and inducing dipole oscillations. The effective mass of the dressed atoms is related to the bare mass m and the bare and dressed trapping frequencies ω and ω^* by the ratio $m^*/m = (\omega/\omega^*)^2$. We measured this ratio following [16]; we start in $|m_F = 0, k_x = 0\rangle$ state and adiabatically turn on the Raman laser in 10 ms while also ramping the detuning to $\delta \approx 0.5 E_L$, shifting the minima in the ground state energy away from zero quasi-momentum. We then suddenly bring the field back to resonance, exciting the BEC's dipole mode in the optical dipole trap. We measured the bare state frequency by using the Raman beams to initially induce motion but subsequently turn them off in 1 ms and let the BEC oscillate. For this set of measurements, we adjusted our optical dipole trap to give new trapping frequencies $(\omega_x, \omega_y, \omega_z)/2\pi = (35.6(4), 32.2(3), 133(3))$ Hz, nominally symmetric in the plane defined by \mathbf{e}_x and \mathbf{e}_y . The Raman beams were co-propagating with the optical dipole trap beams; therefore, the primary axes of the dipole trap frequencies are at a 45° angle with respect to the direction of \mathbf{k}_L .

The kinetic and potential terms in the Hamiltonian including the contribution

¹Well, nothing in the lab is really ‘easy’...

of the Raman and optical dipole trap were

$$\begin{aligned}\hat{H}_\perp &= \frac{\hbar^2 q_x^2}{2m^*} + \frac{\hbar^2 q_y^2}{2m} + \frac{m}{2} [\omega_{x'}^2 x'^2 + \omega_{y'}^2 y'^2] \\ &= \frac{\hbar^2}{2m^*} k_x^2 + \frac{1}{2m} k_y^2 + \frac{m}{4} [(\omega_{x'}^2 + \omega_{y'}^2)(x^2 + y^2) + 2xy(\omega_{x'}^2 - \omega_{y'}^2)],\end{aligned}\quad (5.7)$$

where we have used $x' = (x + y)/\sqrt{2}$ and $y' = (x - y)/\sqrt{2}$ to rotate the dipole trap coordinates by 45° . For an axially symmetric trap with $\omega_{x'} = \omega_{y'}$, the frequency of oscillation along the Raman recoil direction is

$$\omega_x^2 = \frac{m}{2m^*} (\omega_{x'}^2 + \omega_{y'}^2). \quad (5.8)$$

Our trap had a small 3.4 Hz asymmetry and therefore there is some coupling of the motion along the axis perpendicular to \mathbf{k}_L which becomes more significant at larger values of effective mass. The sampling times for the measurements were small compared to the trap asymmetry and therefore we can locally approximate the motion of the atoms by simple harmonic function with a frequency along \mathbf{e}_x given by Equation 5.8.

Figure 5.4 shows the dipole oscillations along the \mathbf{e}_x and \mathbf{e}_y directions for the three different coupling regimes we explored, as well as the bare state motion. The resulting mass ratios for the three coupling regimes are $m/m^* =$ (i) 1.04(8), (ii) 0.71(7), and (iii) 0.62(4).

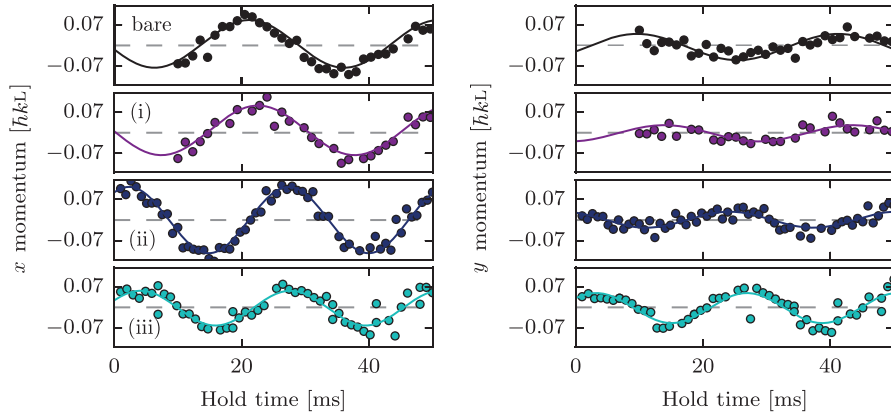


Figure 5.4: Oscillation of the BEC in the dipole trap along the recoil directions \mathbf{e}_x and \mathbf{e}_y for (top) bare atoms, and the three parameter regimes that we explored (i), (ii), and (iii). We believe that the observed low amplitude oscillations along \mathbf{e}_y are due to the initial detuning ramp not being fully adiabatic.

5.2.5 Measured dispersion

We mapped the band structure of SOC atoms for three different coupling regimes. Figure 5.5a shows representative traces of the measured occupation probabilities for short evolution times along with fits to the unitary evolution given by \hat{H}_{SOC} with δ , Ω_0 , and Ω as free parameters. The fit parameters agree well with independent microwave and Raman power calibrations. In the lower two panels, where the Raman coupling strength was periodically modulated, the occupation probabilities oscillate with more than three frequencies since the full description of the system was given by a Floquet quasi-energy spectrum. Figure 5.5b,c shows the occupation probabilities for the parameter regime (iii) for longer evolution times along with the PSD of the occupation probability of each spin state.

We used a non-uniform fast Fourier transform algorithm (NUFFT) on a square window to obtain the power spectral density of the occupation probabilities since our data points were not always evenly spaced because of imperfect imaging shots. The heights of the peaks in the PSD are related to the magnitude of the overlap integrals between the initial state and the Raman dressed states. Figure 5.5c shows the raw PSD of the time evolution of the system under \hat{H}_{SOC} for a given Raman coupling strength and detuning. We put together all the PSDs for the three coupling regimes in the spectra shown on the top three panels in figure 5.6. Each column corresponds to a different coupling regime and the colors represent the different spin states of the measurement basis. The spectra show that some overlap integrals vanish near $\delta = 0$, which is manifested as missing peaks in the PSD. The periodic structure of the Floquet quasi-energy spectrum gives rise to peaks at constant frequencies of $\delta\omega$ and $2\delta\omega$ independently of the Raman detuning, and a structure that is symmetric about the frequencies $2\pi f_1 = \delta\omega/2$ and $2\pi f_2 = \delta\omega$. If you are interested in seeing another nice experiment where the Floquet quasienergy spectrum becomes important due to breaking of the RWA see [17].

We obtained the characteristic dispersion of a SOC system after adding a quadratic term to the PSD, proportional to the measured effective mass, and after rescaling the detuning into recoil momentum units. We combined the PSD of the time evolution of the three $|m_F\rangle$ states to look at the spin dependence of the spectra. Figure 5.7 shows the measured dispersion relations as well as the Floquet quasi-energies calculated for the Hamiltonian parameters obtained from our calibrations. The spectral lines that can be resolved with our technique depend on the overlap integrals of the initial state with the target Hamiltonian eigenstates. Additional energies can be measured by repeating the experiment with different initial states. The spectral lines we were able to resolve are in good agreement with the calculated energies of the Hamiltonian.

Finally, because it is not so trivial to visualize what we did to recover the dispersion for the periodically driven SOC cases, Figure 5.8 illustrates in detail the steps that were taken. The red line in panel a represents a level within a Floquet manifold that has the largest overlap integral with the initial $|m_F = 0, q = 0\rangle$ state. The peaks in the PSD correspond to energy differences between the marked level and the levels in neighboring Floquet manifolds pointed by the colored arrows. We

show the theoretically computed energy differences on top of the measured PSD in panel b. The lowest frequency dominant peaks of the PSD correspond to energy differences with the adjacent lower Floquet manifold. To properly recover the SOC dispersion we need to shift the PSD by a negative quadratic term $-\hbar^2 q_x^2 / 2m^*$ as we show on panel c. We finally invert the frequency axis and shift it by $\delta\omega$. Including the effective mass to reconstruct the spectrum of the time-independent SOC case, amounts to shifting the PSD by a positive quadratic term.

Conclusion

We introduced the basic principles of the Fourier transform spectroscopy technique and used it to measure the spin and momentum dependent dispersion relation of a spin-1 spin-orbit coupled BEC. We additionally studied a periodically driven SOC system and found a rich Floquet quasi-energy spectrum. Our method can be applied generically to any system with long enough coherent evolution to resolve the energy scales of interest, and could prove particularly useful to study systems where it is harder to predict or compute the exact energies, such as cold atom realizations of disordered or highly correlated systems [18]. Moreover, this technique can be extended with the use of spectrograms to study time dependent spectra, such as that of systems with quench-induced phase transitions.

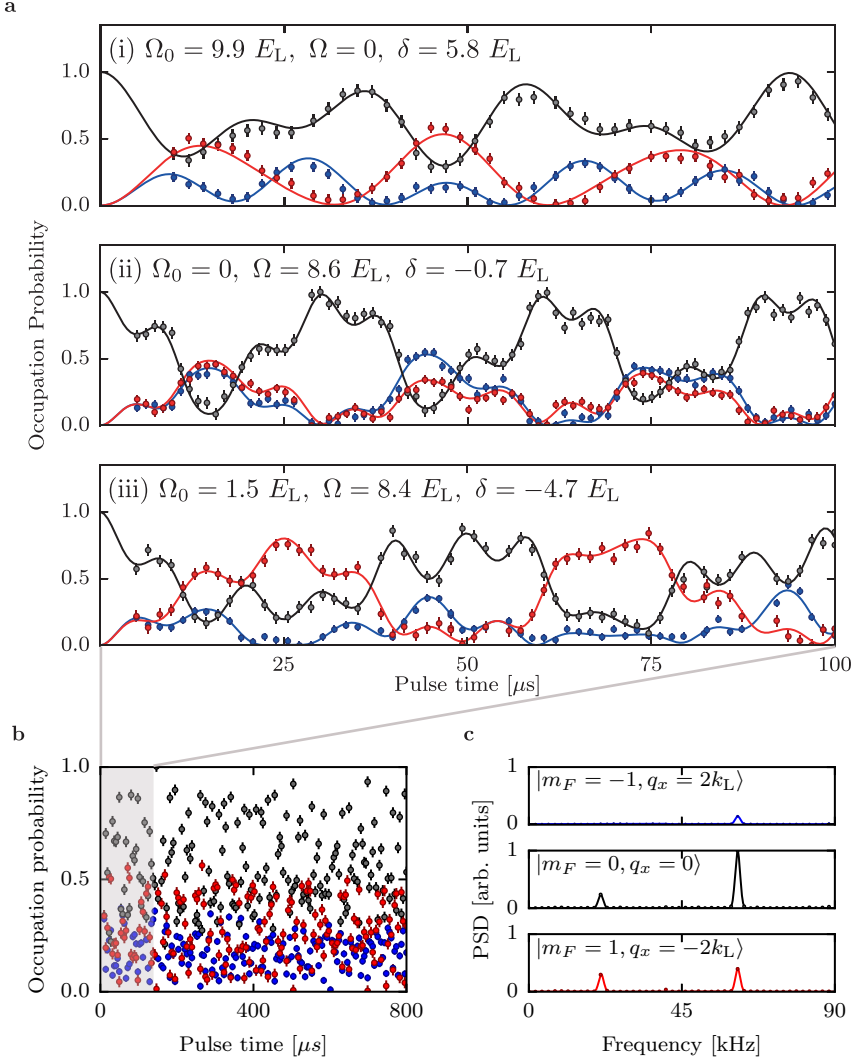


Figure 5.5: **a.** Occupation probability for the three states in the measurement basis $|m_f = -1, q = q_x + 2k_L\rangle$ (blue), $|m_f = 0, q = q_x\rangle$ (black), and $|m_f = +1, q = q_x - 2k_L\rangle$ (red), following unitary evolution under \hat{H}_{SOC} for times up to $100 \mu\text{s}$ at different spin-orbit coupling regimes: (i) $\Omega_0 = 9.9 E_L$, $\Omega = 0$, $\delta = 5.8 E_L$, (ii) $\Omega_0 = 0$, $\Omega = 8.6 E_L$, $\delta = -0.7 E_L$, $\delta\omega = \epsilon + 12 E_L$, and (iii) $\Omega_0 = 1.5 E_L$, $\Omega = 8.4 E_L$, $\delta = -4.7 E_L$, $\delta\omega = \epsilon + 17 E_L$. **b.** Occupation probability for long pulsing up to $800 \mu\text{s}$ for parameters as in (iii). **c.** Power spectral density of the occupation probability. We subtract the mean value of each probability before taking the Fourier transform to remove peaks at $f = 0$. The peaks in the PSD then correspond to the relative eigenenergies of \hat{H}_{SOC} .

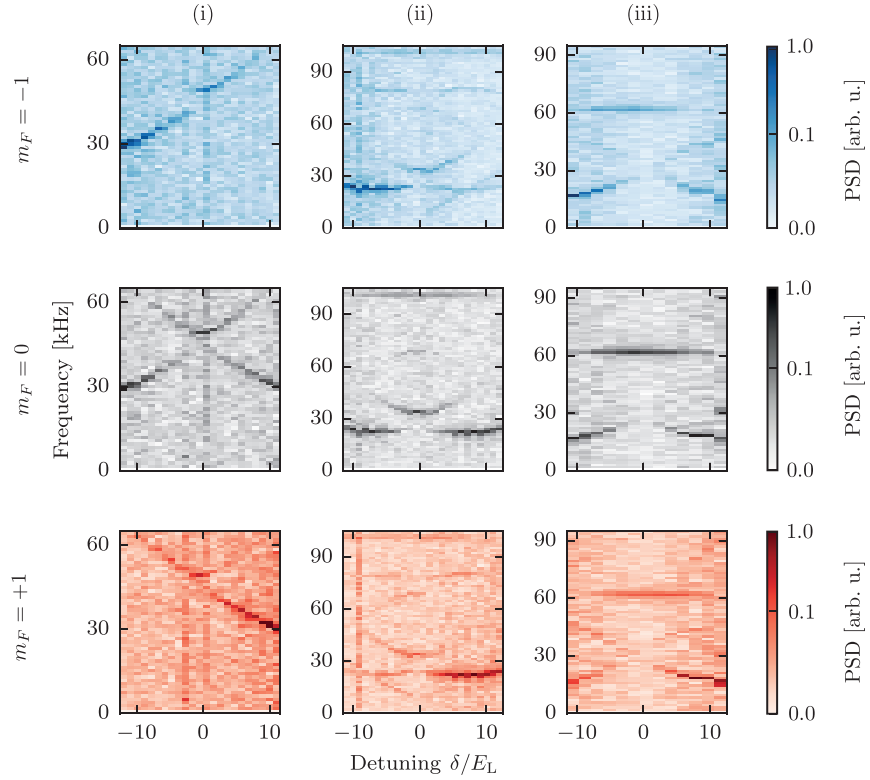


Figure 5.6: Power spectral density of the time dependent occupation probability for each state in the measurement basis for three coupling regimes: (Left) $\Omega_0 = 9.9E_L$, $\Omega = 0$, (Center) $\Omega_0 = 0$, $\Omega = 8.6E_L$, $\delta\omega = \epsilon + 12E_L$, and (Right) $\Omega_0 = 4.9E_L$, $\Omega = 8.4E_L$, $\delta\omega = \epsilon + 17E_L$. Each panel is normalized to peak amplitude to highlight small amplitude features in the PSD of the periodically driven SOC, and the highest value on the frequency axis corresponds to the FFT bandwidth.. b. Spin-dependent SOC dispersion for three different coupling regimes. We combine the PSD of the occupation probability of the states $|m_F = \pm 1, q_x = \mp 2k_L\rangle$, and shift each frequency by an amount proportional to the squared quasimomentum and the effective mass. The dashed lines are the calculated Floquet energies for the Hamiltonian using our calibration parameters.

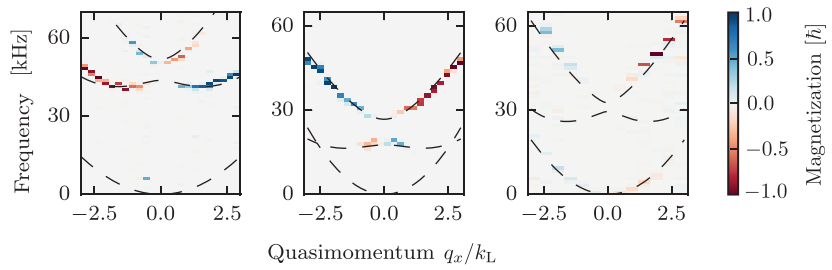


Figure 5.7: Spin-dependent SOC dispersion for three different coupling regimes. We combine the PSD of the occupation probability of the states $|m_F = \pm 1, q_x = \mp 2k_L\rangle$, and shift each frequency by an amount proportional to the squared quasimomentum and the effective mass. The dashed lines are the calculated Floquet energies for the Hamiltonian using our calibration parameters.

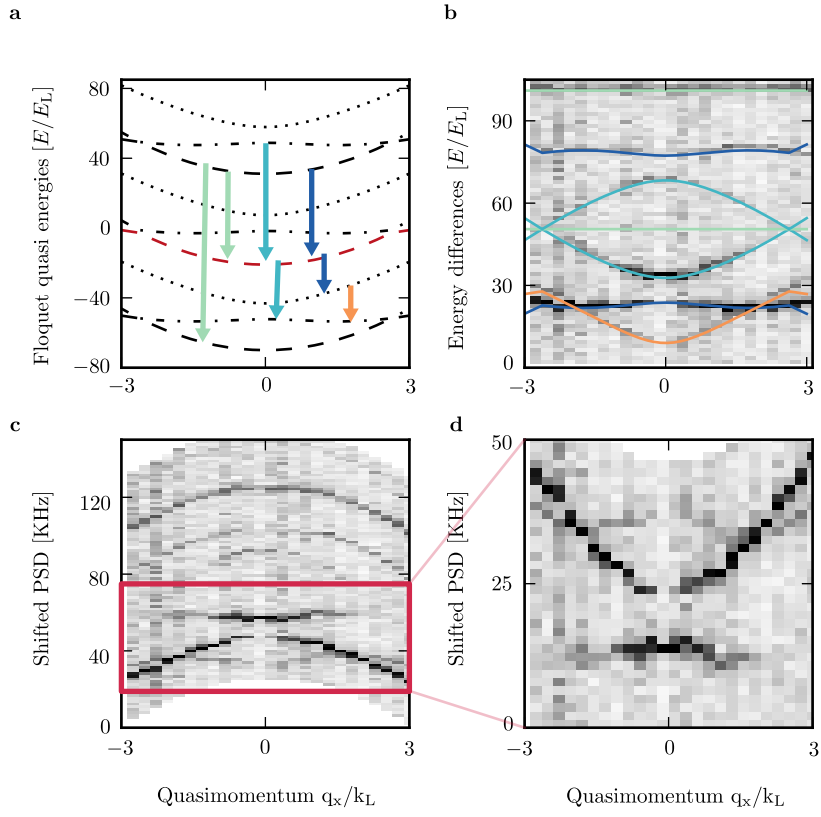


Figure 5.8: **a** Floquet quasi-energy spectrum of a SOC Hamiltonian with periodic coupling strength. The red line represents the eigenstate that has the largest overlap with the initial $|m_F = 0\rangle$ state. The arrows indicate the energies of the states that have non-zero overlap with the initial state and can be measured with Fourier transform spectroscopy. **b** PSD of the occupation probability and numerically calculated energy differences between the levels indicated by the arrows on panel a. **c** PSD shifted by a quadratic term $-\hbar^2 q_x^2 / 2m^*$. The red box indicates the region of interest where we can recover the SOC spectrum. **d** We invert the frequency axis and shift it by $\delta\omega$.

Chapter 6: Synthetic clock transitions through continuous dynamical decoupling

Most of the experiments and experimental techniques described so far have used the hyperfine $|m_F\rangle$ states as effective spins and dressed them with an RF or Raman field. However, due to the linear dependence of their energies with respect to magnetic field, and our lack of control of environmental changes we always had to take special care to stabilize the magnetic field on the lab (see Chapter 4.6.2). An alternative to doing active magnetic field stabilization is to use of ‘clock’ transitions which are first order insensitive to changes in magnetic field, however, they are not present in all systems or for arbitrary system parameters. However, under almost all circumstances, clock transitions can be synthesized using dynamical decoupling protocols. These protocols involve driving the system with an external oscillatory field, resulting in a dynamically protected ‘dressed’ system.

The idea of implementing continuous dynamical decoupling (CDD) in the lab came from a theoretical proposal to engineer Rashba type SOC using Raman beams and a strong RF field [19], the second being a necessary ingredient for CDD. We initially worked in implementing CDD protocols to create ‘synthetic clock states’ as an intermediate step towards our final goal of engineering Rashba SOC. Just like with Fourier spectroscopy, CDD became a workhorse of the lab both for the stability it provides against environmental fluctuations and because it has given us access to non-zero matrix coupling elements that we otherwise would not have when working with the bare $|m_F\rangle$ states. We have continued to use CDD not only for engineering Rashba SOC (Chapter 8) but also to engineer subwavelength optical lattices [12] and Hofstadter [20] cylinders (work in preparation). On the theory side, we also worked on a proposal that uses them as a platform for emulating \mathcal{PT} symmetric Hamiltonians [21].

This Chapter discusses the implementation of CDD in our system of ultra-cold atoms. First I will give a general overview of dynamical decoupling and continuous dynamical decoupling. Then I will describe the technical details and characterization of our CDD protocol which produces a protected three-level system of dressed-states and whose Hamiltonian is fully controllable. Finally I discuss an implementation of concatenated CDD that renders the system first-order insensitive to both magnetic field noise and noise in the control field. This work was published in [22] and was done in parallel with [23].

6.1 Basic principles of CDD

Dynamical decoupling (DD) protocols consist in applying an external control Hamiltonian, generally implemented by a series of pulses, which has the effect of canceling out the dynamics that arise from a quantum system coupling to the environment. DD was first introduced in the context of nuclear magnetic resonance (NMR) with the discovery of spin-echoes [24], where a ‘refocusing’ pulse was applied to eliminate dephasing of spins resulting from variations in magnetic field. These ideas were later generalized in [25] to protect a system from decoherence induced by interactions with a quantum environment. Continuous dynamical decoupling (CDD) relies on the application of time-periodic continuous control fields, rather than a series of pulses. Unlike conventional dynamical decoupling, CDD does not require any encoding overhead or quantum feedback measurements.

A number of dynamical decoupling protocols, pulsed or continuous, have been shown to isolate quantum systems from low-frequency environmental noise [26–34]. Thus far, CDD has inoculated multi-level systems in nitrogen vacancy centers in diamond, nuclear magnetic resonance experiments, and trapped atomic ions [35–42], from spatiotemporal magnetic field fluctuations.

6.2 CDD of a spin-1 system

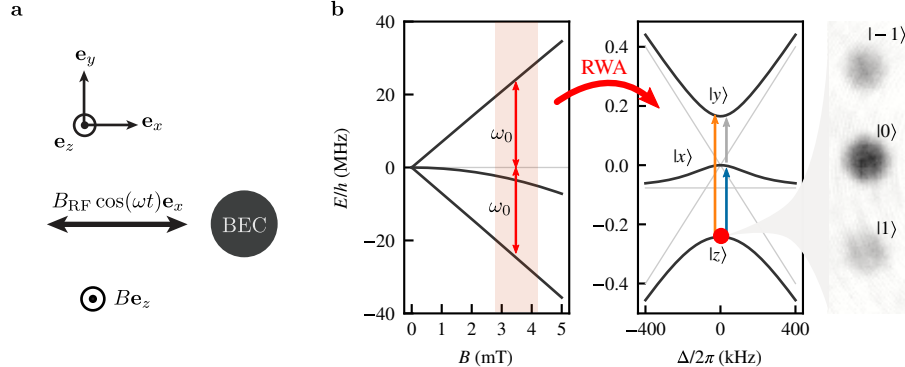


Figure 6.1: **a.** Setup for implementing CDD using a strong RF magnetic field. **b.** Left: dependence of the $5^2S_{1/2}$, $F = 1$ ground state of ^{87}Rb on magnetic field, where the quadratic dependence of the $|m_F = 0\rangle$ state’s Zeeman shift has been exaggerated so it is visible on the same scale. Center: energies of the $|xyz\rangle$ eigenstates, for $\Omega/2\pi = 200$ kHz (black curves) and $\Omega = 0$ (grey curves). Right: TOF absorption image of $|z\rangle$ at $\Delta = 0$, showing the constituent $|m_F\rangle$ states.

We implemented CDD using a strong RF magnetic field with strength Ω , that linked the three $|m_F\rangle$ states comprising the $F = 1$ electronic ground state manifold of ^{87}Rb . The RF field was linearly polarized along \mathbf{e}_x , and had angular frequency ω close to the Larmor frequency $\omega_0 = g_F\mu_B B_0$ from a magnetic field $B_0\mathbf{e}_z$; g_F is the Lande g -factor and μ_B is the Bohr magneton. Using the rotating frame

approximation for the frame rotating at ω (which is valid for $\omega \gg \Omega$), the system is described by

$$\hat{H} = \hbar\Delta\hat{F}_z + \hbar\epsilon(\hat{F}_z^2 - \hat{\mathbb{1}}) + \hbar\Omega\hat{F}_x, \quad (6.1)$$

with detuning $\Delta = \omega - \omega_0$; quadratic Zeeman shift ϵ ; spin-1 angular momentum operators $\hat{F}_{x,y,z}$; and identity operator $\hat{\mathbb{1}}$. For a detailed derivation of Equation 6.1 see Section 4.2.2.

6.3 The $|xyz\rangle$ states

The eigenstates of Equation 6.1 correspond to the CDD basis. In this section I describe their properties and show that they are first order insensitive to magnetic field fluctuations.

6.3.1 State decomposition

We denote the eigenstates of Equation 6.1 by $|x\rangle$, $|y\rangle$ and $|z\rangle$. They are linear combinations of the $|m_F\rangle$ basis states, and for $\Delta = 0$ the (non-normalized) eigenvectors are:

$$\begin{aligned} |x\rangle &= |-1\rangle - |1\rangle, \\ |y\rangle &= |-1\rangle - \frac{\epsilon + \tilde{\Omega}}{\sqrt{2}\Omega} |0\rangle + |1\rangle, \\ |z\rangle &= |-1\rangle - \frac{\epsilon - \tilde{\Omega}}{\sqrt{2}\Omega} |0\rangle + |1\rangle. \end{aligned} \quad (6.2)$$

Figure 6.2 shows the full state decomposition as a function of Δ , where it can be seen that the $|xyz\rangle$ states adiabatically map to the $|m_F\rangle$ states for $\Delta \gg \Omega$: for positive (negative) detuning $|z\rangle$ maps to $|1\rangle$ ($|-1\rangle$); $|y\rangle$ maps in the exact opposite way to $|z\rangle$; and $|x\rangle$ always maps to $|0\rangle$.

We labeled our dressed states $|xyz\rangle$ since for $\Omega \rightarrow 0^+$ and $\Delta = 0$, they continuously approach the $|XYZ\rangle$ states familiar from quantum chemistry [43]:

$$\begin{aligned} |X\rangle &= \frac{|1\rangle - |-1\rangle}{\sqrt{2}}, \\ |Y\rangle &= i\frac{|1\rangle + |-1\rangle}{\sqrt{2}}, \\ |Z\rangle &= |0\rangle. \end{aligned} \quad (6.3)$$

which transform under the application of the spin-1 operators as $\epsilon_{jkl}\hat{F}_j|k\rangle = i\hbar|l\rangle$, so that a resonant probe field can induce transitions between at least one pair of states, irrespectively of its polarization.

Finally, when $\Omega \rightarrow \infty$ they are independent of the driving field amplitude and

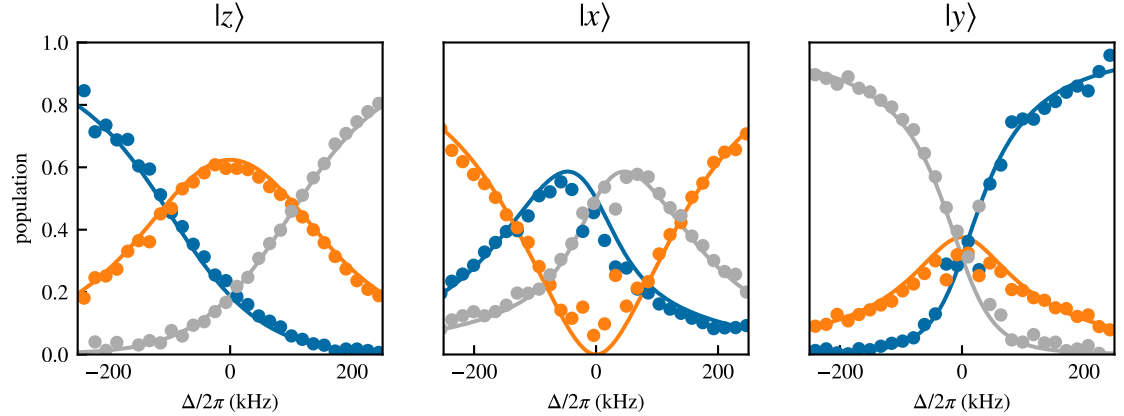


Figure 6.2: Decomposition of the $|xyz\rangle$ states on the $|m_F\rangle$ basis for $\Omega/2\pi = 145(1)$ kHz. The $|m_F = -1, 0, 1\rangle$ states correspond to blue, orange, gray respectively.

continuously approach the eigenstates of the \hat{F}_x operator

$$\begin{aligned} |x\rangle &= |1\rangle - |-1\rangle, \\ |y\rangle &= |1\rangle + \sqrt{2}|0\rangle + |-1\rangle, \\ |z\rangle &= |1\rangle - \sqrt{2}|0\rangle + |-1\rangle. \end{aligned} \quad (6.4)$$

6.3.2 Energies

We can understand the clock-like nature of these states by looking at their eigenvalues which are even functions with respect to Δ as can be seen by the leading order expansion of the eigenenergies $E_i = \hbar\omega_i$ for $\Delta \rightarrow 0$

$$\begin{aligned} \omega_x &= -\frac{\epsilon}{\Omega^2}\Delta^2 + \mathcal{O}(\Delta^4), \\ \omega_y &= \frac{1}{2}(-\epsilon + \tilde{\Omega}) - \frac{(\epsilon + \tilde{\Omega})}{-\epsilon^2 - 4\Omega^2 + \epsilon\tilde{\Omega}}\Delta^2 + \mathcal{O}(\Delta^4), \\ \omega_z &= \frac{1}{2}(-\epsilon - \tilde{\Omega}) + \frac{(\epsilon - \tilde{\Omega})}{\epsilon^2 + 4\Omega^2 + \epsilon\tilde{\Omega}}\Delta^2 + \mathcal{O}(\Delta^4), \end{aligned} \quad (6.5)$$

where we have defined $\tilde{\Omega} = \sqrt{4\Omega^2 + \epsilon^2}$. The energy differences $\hbar\omega_{xy}$, $\hbar\omega_{zy}$ and $\hbar\omega_{zx}$ are only quadratically sensitive to Δ for $\Delta \ll \Omega$ ¹ so that detuning fluctuations $\delta\Delta$ are suppressed to first order, making these a trio of synthetic clock states. For the zx transition, the curvature of ω_x and ω_z has the same sign for $\epsilon < \tilde{\Omega}$ (Equation 6.5). Since the quadratic term changes curvature it can be made arbitrarily small. However, this cancellation does not take place when we consider the dependence of ϵ

¹The energies are quadratic in Δ for $\Delta \ll \Omega$, and linear for $\Delta \gg \Omega$ with a slope of 7 MHz/mT.

on Δ from the Breit-Rabi expression. However one can still find an optimal Ω for which ω_{zx} depends quartically on Δ .

6.3.3 Transition matrix elements

Unlike the $|m_F\rangle$ basis, an oscillatory magnetic field with the right polarization can drive transitions between all pairs of the $|xyz\rangle$ states with non-zero transition matrix elements. The transition matrix elements between the $|xyz\rangle$ have a dependence on both Ω and Δ . For the $\Delta = 0$ case they can be read from the representation of the spin-1 matrices in the $|xyz\rangle$ basis

$$\begin{aligned}\hat{F}_x &\rightarrow \begin{pmatrix} \frac{2\Omega}{\tilde{\Omega}} & 0 & -\frac{\epsilon}{\tilde{\Omega}} \\ 0 & 0 & 0 \\ -\frac{\epsilon}{\tilde{\Omega}} & 0 & -\frac{2\Omega}{\tilde{\Omega}} \end{pmatrix} \\ \hat{F}_y &\rightarrow \begin{pmatrix} 0 & -\frac{i(\tilde{\Omega}-\epsilon)}{\Omega\sqrt{\frac{(\epsilon-\tilde{\Omega})^2}{\Omega^2}+4}} & 0 \\ \frac{i(\tilde{\Omega}-\epsilon)}{\Omega\sqrt{\frac{(\epsilon-\tilde{\Omega})^2}{\Omega^2}+4}} & 0 & -\frac{i(\tilde{\Omega}+\epsilon)}{\Omega\sqrt{\frac{(\tilde{\Omega}+\epsilon)^2}{\Omega^2}+4}} \\ 0 & \frac{i(\tilde{\Omega}+\epsilon)}{\Omega\sqrt{\frac{(\tilde{\Omega}+\epsilon)^2}{\Omega^2}+4}} & 0 \end{pmatrix} \\ \hat{F}_z &\rightarrow \begin{pmatrix} 0 & -\frac{\sqrt{\frac{\epsilon+1}{\tilde{\Omega}}}}{\sqrt{2}} & 0 \\ -\frac{\sqrt{\frac{\epsilon+1}{\tilde{\Omega}}}}{\sqrt{2}} & 0 & -\frac{2}{\sqrt{\frac{(\tilde{\Omega}+\epsilon)^2}{\Omega^2}+4}} \\ 0 & -\frac{2}{\sqrt{\frac{(\tilde{\Omega}+\epsilon)^2}{\Omega^2}+4}} & 0 \end{pmatrix},\end{aligned}\quad (6.6)$$

where the states have been ordered by decreasing energy ($|y\rangle$, $|x\rangle$, $|z\rangle$). We can therefore see that a term in a Hamiltonian that is proportional to \hat{F}_x can only drive transitions between $|z\rangle$ and $|y\rangle$ and that coupling terms proportional to \hat{F}_y and \hat{F}_z can drive both drive transitions between $|z\rangle$ and $|x\rangle$ or $|x\rangle$ and $|y\rangle$ with different strengths. It can be seen from Equation 6.6 that when Ω and ϵ are comparable in magnitude there exists at least one non-zero transition matrix element for each pair of dressed states and they can all be coupled cyclically.

6.4 $|xyz\rangle$ state preparation

We implemented CCD to BECs with $N \approx 5 \times 10^4$ atoms. For all of the experiments described in this Chapter the dipole trap had trapping frequencies of $(f_x, f_y, f_z) = (42(3), 34(2), 133(3))$ Hz. We applied a $B_0 \approx 3.27$ mT bias field that lifted the ground state degeneracy, giving an $\omega_0/2\pi = 22.9$ MHz Larmor frequency,

with a quadratic shift $\epsilon/2\pi = 76.4$ kHz. We determined that the ambient magnetic field fluctuations were dominated by contributions from line noise giving an rms uncertainty $\delta\Delta/2\pi = g_F\mu_B\delta B/h = 0.67(3)$ kHz.

The state preparation consisted of two stages of ARP. On the first stage we followed the usual protocol described in Chapter 4.3.2 to prepare the BEC in any of the $|m_F = 0, -1, 1\rangle$ states. On the second stage we adiabatically transformed the $|m_F\rangle$ states into the $|xyz\rangle$ states. We started with the bias field far from resonance ($(\Delta(t=0)/2\pi \approx -450$ kHz) and with all coupling fields off. Then we ramped on Ω in a two-step process. We first ramped from $\Omega = 0$ to an intermediate value Ω_{mid} , approximately half its final value in 1 ms. We then ramped Δ to zero in 3 ms by increasing the magnetic field B_0 . After allowing B_0 to stabilize for 30 ms, we ramped the RF dressing field to its final value Ω in 1 ms, yielding the dynamically decoupled $|xyz\rangle$ states. It was important that the wait for the field to stabilize was performed at an intermediate Ω_{mid} as we found several times that the capacitors on the impedance matching network of the antenna used to generate the RF field would burn if we kept the power on for too long. After performing any experiment with the $|xyz\rangle$ states we measured their populations by adiabatically deloading them back into the $|m_F\rangle$ basis. We first ramped B_0 so that Δ approached its initial detuned value in 2 ms, and then ramped off the dressing RF field in 1 ms. A typical experimental sequence for Δ and Ω can be visualized in Figure 6.4. As usual, we obtained the spin-resolved momentum distribution using absorption imaging after TOF, with a Stern-Gerlach field to spatially separate the spin components. The right panel of Figure 6.1b shows a TOF image of the $|m_F\rangle$ state decomposition of the $|z\rangle$ state. For this image as well as for the measurement of the dressed state decomposition shown in Figure 6.2 we suddenly (not-adiabatically) turned the RF coupling off, thereby projecting the $|xyz\rangle$ states back into the $|m_F\rangle$ basis.

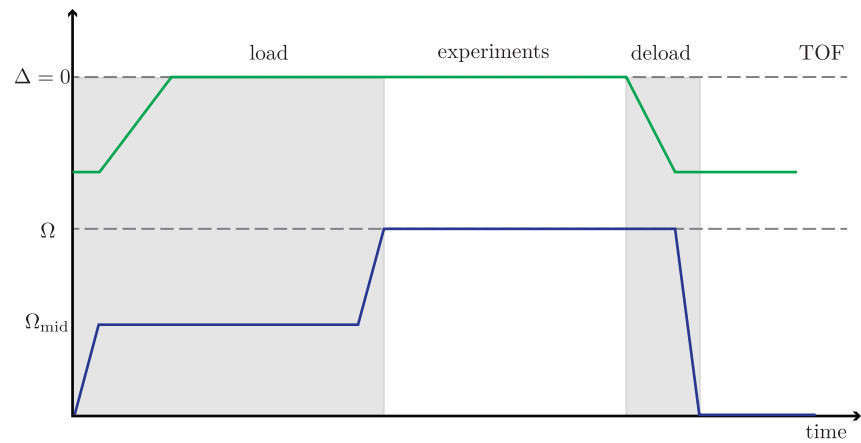


Figure 6.3: Detuning and RF coupling strengths ramps (not to scale) performed to adiabatically prepare the $|xyz\rangle$ states starting in the $|m_F\rangle$ states and vice versa.

6.5 Initial characterization of Ω

Producing RF fields with large coupling strength was not a trivial task and when testing different antenna designs it was important to have an easy and quick way of characterizing them. We mostly relied on two different techniques to get an initial estimate of Ω : first, we prepared atoms in $|m_F = -1\rangle$ and pulse on the RF to drive transitions between the three $|m_F\rangle$ states. We would then fit the populations in the three states as a function of pulsing time to the time evolution given by propagating the time dependent Schrödinger equation using the RF Hamiltonian (Equation 6.1) with Ω and Δ as free parameters.

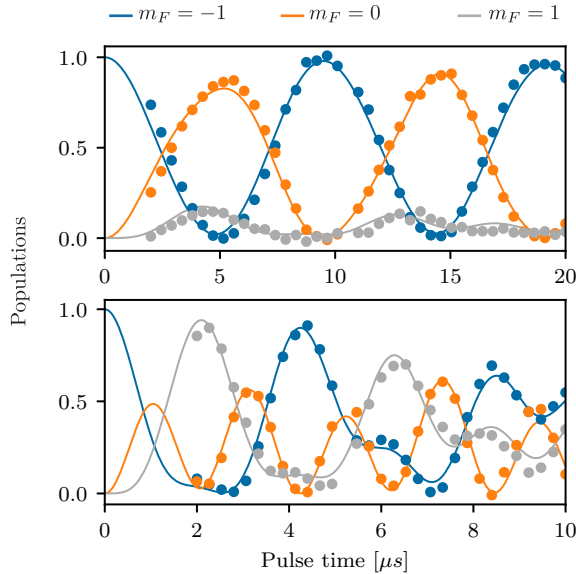


Figure 6.4: We prepared the system in the $|m_F = 0\rangle$ state and pulsed Ω and fit the populations in the $|m_F\rangle$ states as a function of pulsing time to get an initial estimate of Ω . The top panel shows the time evolution of $\Omega/2\pi \approx 76$ kHz and the bottom panel shows the evolution for $\Omega/2\pi \approx 238$ kHz

Alternatively, we followed the loading procedure described in Section 6.4 but suddenly turned Ω off for different values of Δ to get the decomposition of the $|xyz\rangle$ states in terms of $|m_F\rangle$ states. We then fit the populations to the eigenstates of the Equation 6.1 with Ω and Δ as free parameters. Figure 6.2 is an example of such type of calibration.

For an antenna with a high quality factor such as ours ($q \sim 20$) we could not ‘suddenly’ turn Ω on or off as it takes some time for power to build up and to die out when the RF fields are turned on or off. If we did not include this into the model used to calibrate Ω we could get some results that were slightly off. In the end we only used this measurements as initial estimates and once we found an antenna design that could produce a large enough Ω we used the spectroscopy techniques described in next section to fully characterize the system.

6.6 Spectroscopy

We confirmed our control and measurement techniques spectroscopically by measuring the energy differences between the $|xyz\rangle$ states with an additional probing field with angular frequency $\omega + \omega_p$, coupling strength Ω_p and polarized along \mathbf{e}_y . In the frame rotating with angular frequency ω and after using a RWA the system was described by the Hamiltonian

$$\begin{aligned}\hat{H} = & \Delta\hat{F}_z + \hbar\epsilon(\hat{F}_z^2/\hbar^2 - \hat{\mathbb{I}}) + \Omega\hat{F}_x \\ & + \Omega_p(\sin(\omega_p t)\hat{F}_x + \cos(\omega_p t)\hat{F}_y).\end{aligned}\quad (6.7)$$

In this rotating frame the probe field initially polarized along \mathbf{e}_y has components along \mathbf{e}_x and \mathbf{e}_y , resulting in at least one non-zero transition matrix element for all transitions between pairs of dressed states. If the probing field was polarized along \mathbf{e}_z we would not be able to drive the zy transition as can be seen from the matrix elements in Equation 6.6.

To probe the dependence on detuning of the $|xyz\rangle$ state energies, we pulsed Ω_p on for a constant time and scanned ω_p for different values of Δ . Figure 6.1b shows the spectroscopically resolved values of $\omega_{xy}/2\pi$, $\omega_{yz}/2\pi$, and $\omega_{zx}/2\pi$ for $\Omega/2\pi = 194.5(1)$ kHz and the side panel shows a sample spectra measured with coupling strength $\Omega_p/2\pi \approx 1$ kHz and $\Delta/2\pi \approx 9$ kHz. The dashed curves were computed by diagonalizing Equation 6.1, and they clearly depart from our measurements for the zx transition. This departure results from neglecting the weak dependence of the quadratic shift ϵ on bias field B_0 . In near-perfect agreement with experiment, the solid curves from the full Breit-Rabi expression account for this dependency.

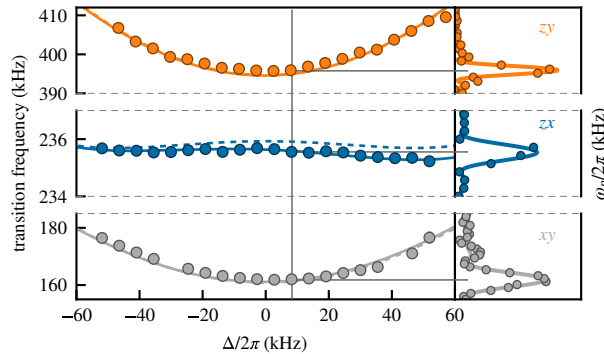


Figure 6.5: Left: spectroscopic data showing transitions between the $|xyz\rangle$ states for $\Omega/2\pi = 194.5(1)$ kHz. The vertical scale of the center panel (zx transition) has only 10% the range of the other panels. The dashed lines correspond to the Hamiltonian of Equation 6.1 while the solid lines include the dependence of the quadratic shift on Δ . Right: representative spectra.

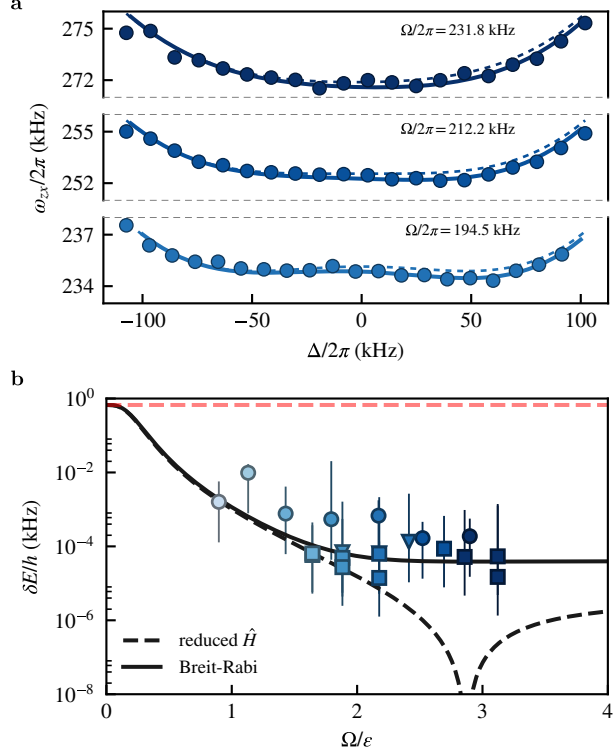


Figure 6.6: **a.** Transition frequency $\omega_{zx}/2\pi$ for three values of $\Omega/2\pi$. The dashed curves correspond to Equation 6.7, while the solid curves use the Breit-Rabi expression. **b.** The change in energy from our experimental detuning fluctuations as measured in the $|m_F\rangle$ basis is $\delta\Delta/2\pi = 0.67$ kHz (red dashed line). Triangles correspond to $|xyz\rangle$ spectroscopy data, squares to side-of-peak π -pulse data, and circles to double-dressed data. The black dashed (solid) curve was calculated using Equation 6.7 (the Breit-Rabi expression). The shading of the data points corresponds to the Rabi frequencies in Figure 6.8.

6.7 Robustness

To characterize the robustness of the $|xyz\rangle$ states, we focus on the zx transition which can be made virtually independent of magnetic field variations due to the similar curvature of $\omega_z(\Delta)$ and $\omega_x(\Delta)$ (see the middle panel of Figure 6.1b). We quantified the sensitivity of this transition to field variations with three methods corresponding to the different markers in Figure 6.6b: (1) Triangles denote data using full spectroscopic measurements similar to Figure 6.6a. (2) Squares denote data in which a detuned π -pulse of the probe field transferred approximately half of the atoms from $|z\rangle$ to $|x\rangle$. This ‘side-of-peak’ technique overcomes the limitation of Rabi spectroscopy being first-order insensitive to changes in ω_{zx} . (3) Circles describe data using a double dressing technique that will be described in Section 6.9. In each case we measured the energy shift from resonance as a function of detuning (magnetic field) and then used a fourth order polynomial fit to extract the rms

residuals $\delta\omega_{zx}$ due to the known detuning noise ². The results are not consistent with the theory simple from Equation 6.7 (dashed) and instead require the Breit-Rabi expression (solid) to obtain full agreement ³.

Even at our smallest coupling $\Omega/2\pi = 69(1)$ kHz the typical magnetic field noise was attenuated by two orders of magnitude, rendering it essentially undetectable. Ideally, the radius of curvature of $\omega_{zx}(\Delta)$ changes sign at about $\Omega/2\pi = 220$ kHz, leaving only a Δ^4 contribution, however, in practice the small dependence of ϵ on B prevents this perfect cancellation.

6.7.1 Optimal response to noise

The sensitivity of the zx transition to detuning fluctuations can be optimized further by working at $\Delta \neq 0$ as shown in Figure 6.7. This behavior can only be captured by including the dependence of the quadratic shift on Δ as given by the Breit-Rabi expression.

For small values of Ω the optimum value of Δ corresponds to one of the concave features of the zx transition energy that arise due to the asymmetry introduced by the quadratic shift. As Ω gets larger, these features merge into a single one and the optimum value is $\Delta \approx 0$. The deviation from $\Delta = 0$ is due to an overall tilt of the transition energy coming from the dependence of the quadratic shift on Δ . At the optimum point $\Omega/\epsilon \approx 3$ the sensitivity of the synthetic clock transition is 1.9×10^{-7} kHz, c.f. the ^{87}Rb clock transition which scales as 57.5 kHz/mT² and gives 5.8×10^{-7} kHz.

6.8 Driving dressed state transitions

We explored the strength of the probe-driven transitions between these states by observing coherent Rabi oscillations (Figure 6.8a) where our BEC was prepared in $|z\rangle$ and the probe field had strength $\Omega_p/2\pi \approx 1$ kHz. The top panel shows Rabi oscillations between $|m_F = 0\rangle$ and $|m_F = -1\rangle$ states for reference, and the remaining panels show oscillations between $|z\rangle$ and $|x\rangle$. The observed Rabi frequency between dressed states decreased with increasing Ω indicating a dependence of the zx transition matrix elements on Ω . We repeated this experiment driving all possible pairs of dressed state transitions at fixed Ω_p for, and Figure 6.8b shows the dependence of these matrix elements on Ω for $\Delta = 0$.

The coherence of the Rabi oscillations for longer times was limited by gradients in Ω that lead to phase separation of the dressed states, and therefore loss of contrast in the oscillations. This effect was faster for smaller frequency Rabi oscillations. For example for $\Omega_p/2\pi = 5$ kHz we observed coherent Rabi oscillations with almost full contrast for more than 10 ms while for the $\Omega_p/2\pi = 870$ Hz oscillation shown in

²Our procedure also quantifies the small fluctuations that survive for spectra that are flat beyond second order, as in Equation 6.1.

³The fluctuations can be even smaller for a given Ω if we allow for $\Delta \neq 0$.

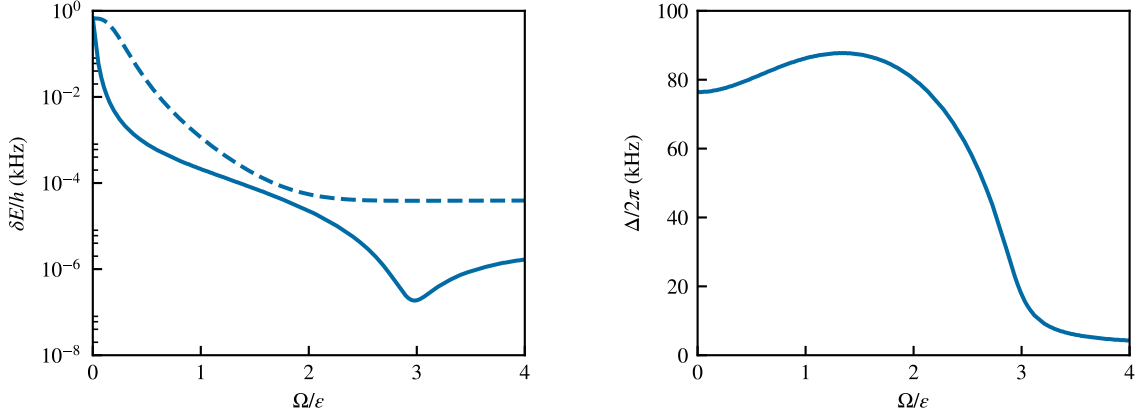


Figure 6.7: Left: The optimum response (solid) of the zx transition to detuning fluctuations allowing for finite Δ compared to $\Delta = 0$ (dashed) for the full Breit-Rabi model. Right: The values of Δ that correspond to the minimum derivative of ω_{zx} .

Figure 6.9 the contrast was significantly reduced after 5 ms. The loss of contrast was even worse when we tried performing a Ramsey sequence where the time evolution is most sensitive to the environment. One solution to this problem would be to change the experimental setup to a double loop antenna to generate a more spatially uniform magnetic field.

In comparison, we found that for both Rabi and Ramsey oscillations between the $|m_F\rangle$ states the phase started deteriorating after a few hundreds of μs , this is not surprising due to bias magnetic field temporal noise. We cancelled gradient magnetic fields so that no phase separation of the bare states was observed for > 10 sec. As a result, the system can in principle undergo coherent evolution without loss of contrast for a long time but because of field fluctuations between shots what we actually observe is full contrast noise.

6.9 Concatenated CDD

The driving field Ω coupled together the $|m_F\rangle$ states, giving us the $|xyz\rangle$ synthetic clock states that were nearly insensitive to magnetic field fluctuations. However, the spectrum of these states is first-order sensitive to fluctuations $\delta\Omega$ of the driving field. Reference [30] showed that an additional field coupling together with these $|xyz\rangle$ states can produce doubly-dressed states that are insensitive to both $\delta\Omega$ and $\delta\Delta$: a process called concatenated CDD. In our experiment, the probe field provided the concatenating coupling field. Because $\Omega_p \ll \Omega$, we focus on a near-resonant two-level system formed by a single pair of dressed states, here $|z\rangle$ and $|x\rangle$, which we consider as pseudospins $|\uparrow\rangle$ and $|\downarrow\rangle$. These are described by the

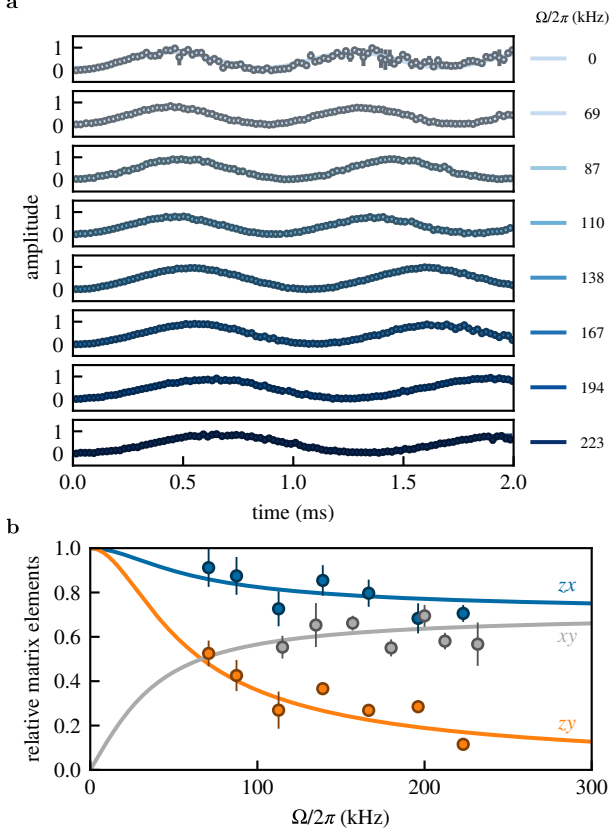


Figure 6.8: **a.** Rabi oscillations. Phase coherence is maintained throughout the oscillations in the dressed basis, while it is quickly lost in the $|m_F\rangle$ basis. The marker size reflects the typical uncertainties on the dressed basis oscillations. **b.** Transition matrix elements for zx (blue) and zy (orange) transitions decrease monotonically with increasing Ω for $\Delta = 0$, while they increase for xy .

effective two-level Hamiltonian

$$\hat{H}_p = \frac{\hbar\Delta'}{2}\hat{\sigma}_3 + \hbar\Omega' \cos(\omega_p t)\hat{\sigma}_1, \quad (6.8)$$

with energy gap $\Delta' \approx \omega_{z,x}$ (shifted by off-resonant coupling to the zy and xy transitions) and coupling strength $\Omega' \propto \Omega_p$, as set by the matrix elements displayed in Figure 6.8b. Here $\hat{\sigma}_{1,2,3}$ are the three Pauli operators.

We perform a second transformation into a frame rotating with angular frequency ω_p and use a RWA to compute the eigenenergies of Equation 6.8. For large values of Ω' the energies take the values $E_{\uparrow,\downarrow} \approx \pm\Omega'/2 + (\Delta')^2/2\Omega'$. Even though $E_{\uparrow,\downarrow}$ are still first order sensitive to Ω because $\Delta' \approx \omega_{z,x} \propto \Omega$, its effect is suppressed by a factor of $1/\Omega'$. Thus, the concatenated CDD field protects from the fluctuations $\delta\Delta'$ of the first dressing field in a similar way that CDD provided protection from detuning noise $\delta\Delta$. Table 6.1 summarize the dependence of the $|xyz\rangle$ and $|\uparrow\downarrow\rangle$ energies on Δ , Ω and Ω' .

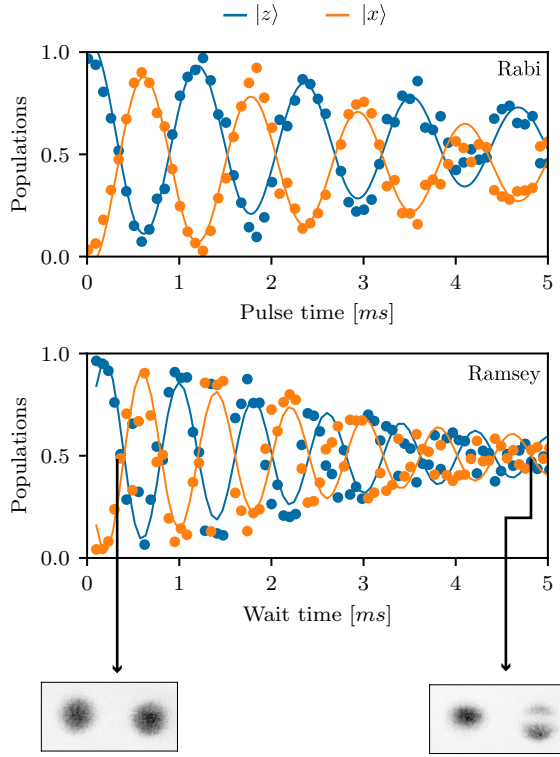


Figure 6.9: Loss of contrast in coherent oscillations. A Rabi oscillation (top) between the $|z\rangle$ and $|x\rangle$ states with $\Omega_p/2\pi = 870$ Hz decays by $1/e$ in 4.6 ms and a Ramsey oscillation (middle) with about 1 kHz frequency decays in about 3 ms. The gradients in Ω lead to phase separation of dressed states and loss of contrast for longer pulse/wait times.

We produced doubly-dressed states by doing (one more!) ARP sequence. We initialized the system in the $|\Downarrow\rangle$ state with RF coupling strength Ω_i . We set the probe frequency to be ~ 20 kHz off resonant with respect to the $|\downarrow\rangle \rightarrow |\uparrow\rangle$ transition and ramped it on in 10 ms. We then ramped $\Omega_i \rightarrow \Omega_f$ in 30 ms. The experimental sequence can be visualized in Figure 6.10. We chose the value of Ω_f such that it would bring ω_p to resonance at $\Delta = 0$, creating double dressed states that were equal superposition of $|\downarrow\rangle$ and $|\uparrow\rangle$. We quantified the sensitivity of this transition to large changes in the detuning Δ in terms of the fractional population imbalance $\langle \hat{\sigma}_3 \rangle = P_{\downarrow}(\Delta) - P_{\uparrow}(\Delta)$, shown in Figure 6.11a for $\Omega_f/2\pi = 138.2(1)$ kHz⁴. This signal is first-order sensitive to $\omega_{\downarrow,\uparrow}$, and provided our third measurement of sensitivity to detuning in Figure 6.6b denoted by circles.

We compared the fidelity of preparing a superposition of the $|\downarrow\rangle$ and $|\uparrow\rangle$ states to adiabatically preparing a similar superposition of the the $|m_F = 0\rangle$ and $|m_F = -1\rangle$ states using a single ARP (no dressed states involved), both with a probe

⁴We chose the maximum value of Δ such that the population of $|y\rangle$, was negligible after de-loading.

Table 6.1: Energies of the CDD and CCDD states as a function of Δ , Ω and Ω' . The dependence on parameters not relevant to the expansion is given by the functions f_1 , f_2 , g_1 and g_2 .

	CDD	concatenated CDD
Δ dependence	$f_1(\epsilon, \Omega)\Delta^2$	$f_2(\Omega, \epsilon)\frac{\Delta^2}{\Omega'}$
Ω, Ω' dependence	$\Omega + g_1(\Delta, \epsilon)\frac{1}{\Omega}$	$\left[\Omega^2 + \epsilon\Omega + g_2(\Delta, \epsilon)\frac{1}{\Omega}\right]\frac{1}{\Omega'}$

field strength of ≈ 1 kHz. Figure 6.11b shows the rms deviation of the population imbalance measured over a few hundred repetitions of the experiment. The rms deviation for the dressed basis is 0.024(1) and is an order of magnitude smaller than for the $|m_F\rangle$ basis 0.29(1), where it practically impossible to prepare a balanced superposition for the parameters used here ⁵.

Figure 6.11c shows the response of the $|\downarrow\rangle \rightarrow |\uparrow\rangle$ transition to small changes $\delta\Omega$ for different values of Ω_p . We prepared an equal superposition of $|\downarrow\rangle$ and $|\uparrow\rangle$ following the same procedure as before for $\Omega_f/2\pi = 138.2(1)$ kHz. We then measured how the population imbalance changes for small variations of Ω — the effective detuning in the ‘twice-rotated frame’ — for different probe amplitudes Ω_p . We defined a sensitivity parameter $d\langle\hat{\sigma}_3\rangle/d\Omega$, obtained from the linear regime of the population imbalance measurements (see inset in Figure 6.11c). The robustness of the doubly-dressed states against $\delta\Omega$ fluctuations increased with Ω_p , thus verifying the concatenating effect of CDD in the $|xyz\rangle$ basis.

However promising the application of multiple concatenating fields might seem, this procedure has a fundamental limitation. Each time a new coupling field is applied the energies of the dressed states are reduced to something on the order of magnitude of the applied concatenating field. For example, in the experiments we have described here we started with $|m_F\rangle$ with transition frequencies on the order of MHz. The transition frequencies of the $|xyz\rangle$ states are reduced to hundreds of kHz (or in general the magnitude of Ω). After applying the second concatenating RF field the transition frequencies of the $|\uparrow\downarrow\rangle$ are of the order of Ω_p which needs to be smaller than Ω in order for the second RWA to be valid. Therefore we see that after applying multiple concatenating fields we are at the risk of having some very robust states that are also very closely spaced in energy which might not be desirable for some applications.

⁵In Figure 6.11b, the noise in the $|m_F\rangle$ basis is not Gaussian distributed as is typical of line noise in these experiments.

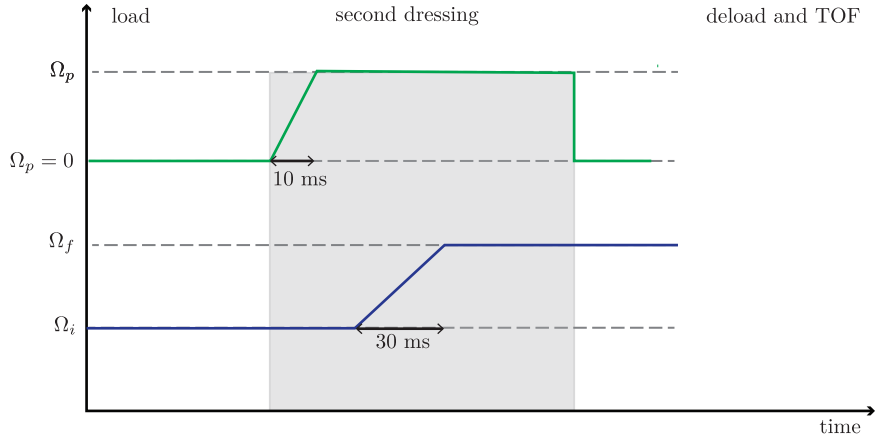


Figure 6.10: Experimental protocol for implementing concatenated CDD. We started an initial RF coupling strength Ω_i and ramped on the probe field Ω_p in a few ms with $\omega_p = \omega_{z,x}(\Omega_f)$ so that it was initially slightly off resonant with the zx transition. We then ramped the the RF field to Ω_f , brining ω_p to resonance.

6.10 Conclusions

We realized a three-level system that is dynamically decoupled from low-frequency noise in magnetic fields, measured now-allowed transitions between all three states, and demonstrated control techniques for creating arbitrary Hamiltonians. These techniques add no heating or loss mechanisms, yet within the protected subspace retain the full complement of cold-atom coherent control tools such as optical lattices and Raman laser coupling, and permit new first-order transitions that are absent in the unprotected subspace. These transitions enable experiments requiring a fully connected geometry as for engineering exotic states, e.g., in cold-atom topological insulators, and two-dimensional Rashba spin-orbit coupling in ultracold atomic systems [19, 44].

The synthetic clock states form a decoherence-free subspace that can be used in quantum information tasks where conventional clock states might be absent, or incompatible with other technical requirements [45]. Moreover, their energy differences are proportional to the amplitude of the dressing field, and hence tunable, so they can be brought to resonance with a separate quantum system. The effective quantization axis can be arbitrarily rotated so that the two systems can be strongly coupled, pointing to applications in hybrid quantum systems [46, 47]. Introducing a second coupling field shields the system from fluctuations of the first, a process which can be concatenated as needed. More broadly, synthetic clock states should prove generally useful in any situation where fluctuations of the coupling field can be made smaller than those of the environment.

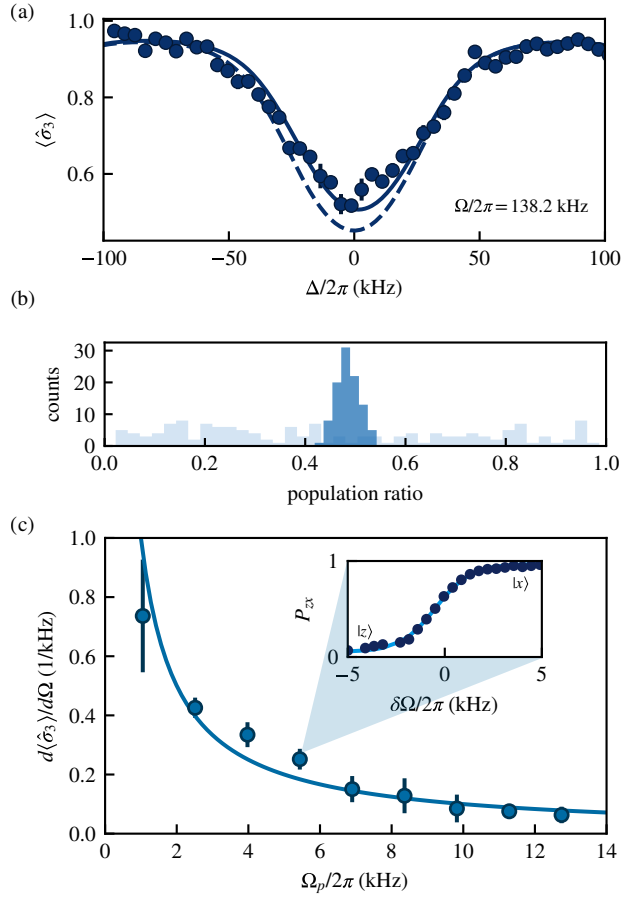


Figure 6.11: (a) The fractional population imbalance of the $\downarrow\uparrow$ transition for $\Omega/2\pi = 138.2(1)$ kHz over detuning Δ . The dashed curve is calculated using Equation 6.7 and the solid one using the full Breit-Rabi expression. (b) The fidelity of preparing a balanced superposition of $|\downarrow\rangle$ and $|\uparrow\rangle$ (dark blue) states compared to $|m_F = 0\rangle$ and $|m_F = -1\rangle$ states (light blue). (c) The robustness of \downarrow, \uparrow transition against fluctuations $\delta\Omega$ for different probe field coupling strengths. The points represent the slope of the fitted curves to the fractional population imbalance (inset).

Chapter 7: Topological order in quantum systems

Topological order can be found in a wide range of physical systems, from crystalline solids [48], photonic meta-materials [49] and even atmospheric waves [50] to optomechanic [51], acoustic [52] and atomic systems [53]. Topological systems are a robust foundation for creating quantized channels for transporting electrical current, light, and atmospheric disturbances. These topological effects can be quantified in terms of integer-valued invariants such as the Chern number, applicable to the quantum Hall effect [54, 55], or the \mathbb{Z}_2 invariant suitable for topological insulators [56].

The topology of Bloch bands defines integers that serve to both classify crystalline materials and precisely specify properties, such as conductivity, that are independent of small changes to lattice parameters [48]. Topologically non-trivial materials first found application in metrology with the definition of the von Klitzing constant as a standard of resistance, which is now applied in the realization of the kilogram [57]. Today, topological systems have found applications in the engineering of low loss optical waveguides [49] and present a promising path to quantum computation [58]. [Not sure if I want to keep this paragraph as it is.]

We got interested in topology when working on engineering Rashba [59] type spin-orbit coupling in the lab. Our system had non-trivial topology but it broke from the usual mold of topological materials as it didn't have an underlying crystalline structure that conventionally yields to integer Chern numbers.

Before describing our experiments that characterize the unconventional topology of a Rashba spin-orbit coupled gas, in this Chapter I take a step back to describe the basic concepts of topology and its applications to the band theory of solids. The ideas of topology and how exactly one can connect donuts with band structures might feel a bit obscure and complicated for non-experts in the field. I wrote this Chapter with that in mind, with the hope that it can be followed by non-experts and provide some insight and intuition about this field. The concepts introduced in this Chapter will be necessary for understanding the results presented in Chapter 8.

7.1 Topology in mathematics

Topology is a branch of mathematics that studies continuity [60]. The most familiar example might be that of objects being continuously deformed into one another. For example, a donut can be continuously deformed into a coffee mug but if we want to deform it into a pretzel we need to poke more holes in it. This gives us some intuition that the donut and the mug must share the same topology, which is different from that of the pretzel. Topology also studies more abstract objects but

I will limit the discussion to closed two-dimensional surfaces in three dimensions, which will be enough to provide some intuition when we define topological invariants for band structures in the following sections.

The topology of 2D surfaces can be classified by the Euler characteristic, and it is related to the local Gaussian curvature of a surface by the Gauss-Bonet theorem. The Gaussian curvature can be interpreted in the following way: at any point in a surface we can find a normal vector which is orthogonal to the tangent plane of the surface. We can then define a family of planes containing the normal vector and their intersection with the surface defines a family of curves. The curvature of any of these curves at the point where the planes intersect, which is equal to the quadratic coefficient in a Taylor expansion around that point, is called the normal curvature κ . When we consider all the normal curvatures, the minimum and maximum of these are called the principal curvatures and are used to define the Gaussian curvature at any point of a surface $K = \kappa_{\min}\kappa_{\max}$ [60]

The Gauss-Bonnet theorem states that the integral of the local Gaussian curvature over the whole surface is equal to the integer valued Euler characteristic

$$\chi = \frac{1}{2\pi} \int_S K dA, \quad (7.1)$$

which is related to the genus g (number of holes or handles in the surface) by $\chi = 2(1 - g)$. The Gauss-Bonnet theorem is a very powerful result as it relates the local properties of a surface, the Gaussian curvature, with a global topological invariant, the Euler characteristic. [Add picture to describe principal curvatures?]

In the following sections I will introduce topological invariants in the context of condensed matter physics, which even though might seem a bit more abstract, their interpretation can be closely related to the concepts just defined in this section.

7.2 Topological order in condensed matter

Just like topology classifies properties of geometric objects, one important task of condensed matter physics has been to classify phases of matter. Many of these phases, for example magnetic or conducting phases, can be described in terms of order parameters related to spontaneously broken symmetries [61]. However, in the past few decades and increasing number of systems have been found where it is only possible to understand their phases and properties in terms of the underlying topology of their quantum states. This new paradigm of physics has been so important that in 2016 the Nobel prize in physics was awarded to David J. Thouless, F. Duncan M. Haldane and J. Michael Kosterlitz for the theoretical discoveries of topological phase transitions and topological phases of matter

The effects of topology in condensed matter systems were first observed when von Klitzing and colleagues [62] measured the quantized Hall resistance in two-dimensional electron gases subjected to a strong perpendicular magnetic field. The effect can be understood semi-classically by thinking of the electrons' quantized

cyclotron orbits¹ that give rise to Landau levels. If the Landau levels are filled then there is an energy gap separating two consecutive levels and the material acts as an insulator but if an electric field is applied the orbits drift and the electrons will be ‘skipping orbits’ in the edge as can be seen in Figure 7.1, giving rise to what is known as edge states.

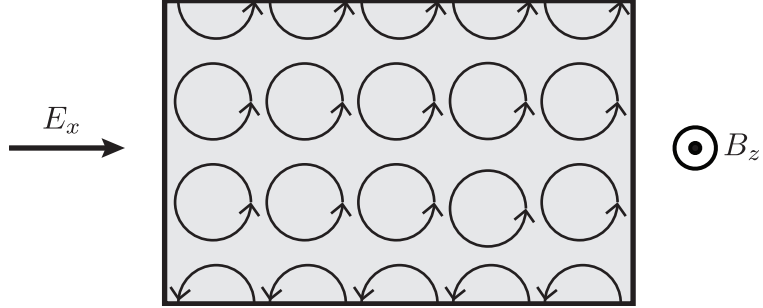


Figure 7.1: The quantum Hall effect. An electron gas is confined in a two-dimensional material and a strong magnetic field is applied perpendicular to the plane. The electrons on the bulk travel in cyclotron orbits while the electrons on the edge travel ‘skipping orbits’.

In a seminal paper Thouless, Kohomoto, Nightingale, and den Nijs [54] explained that the quantization of the Hall conductivity is determined by the underlying topology of the band structure. Just like the Euler characteristic defined in Equation 7.1 classifies 2D solids that can be continuously deformed without opening or closing holes, there is a topological invariant that classifies band structures that can be deformed into one another without opening or closing an energy gap. This invariant, initially known as the ‘TKNN invariant’, was later recognized by the mathematical physicist Barry Simon as the ‘first Chern class invariant from $U(1)$ fiber bundles’ [64]² and the TKNN invariant became what is known today as the Chern number or Chern invariant. Another very valuable contribution from Simon’s work was that he made the connection between the Chern number and the Berry’s geometrical phase [66] which will be defined in the following sections and will allow us to make a physical interpretation of this otherwise abstract seeming topological invariant.

¹This is an intuitive but not very complete explanation of the quantum Hall effect, see [63] if you want to learn more about this subject.

²See [65] if you want to dive into hardcore topology.

7.3 Berry phase and Berry curvature

A Berry or geometric phase is used to describe the phase acquired by a quantum state as it moves through a closed trajectory in parameter space. It plays a key role in topological band theory and can help provide a physical interpretation of the Chern number.

Consider a Hamiltonian \hat{H} that depends on a set of parameters $\mathbf{r} = (r_1, r_2, \dots)$. If the parameters are slowly changed in time, the corresponding change in the system can be described by a path in parameter space $\mathbf{r}(t)$. The state $|\psi(t)\rangle$ evolves according to the time dependent Schrödinger equation and at any given time t there is a basis that satisfies

$$\hat{H}(\mathbf{r}) |n(\mathbf{r})\rangle = E_n(\mathbf{r}) |n(\mathbf{r})\rangle \quad (7.2)$$

for $\mathbf{r} = \mathbf{r}(t)$. Suppose the system is initially in state $|n(\mathbf{r}(t=0))\rangle$, if the parameters are changed slowly such that the adiabatic theorem is valid, then at time t the state of the system can be written as

$$|\psi(t)\rangle = \exp \left\{ -\frac{i}{\hbar} \int_0^t dt' E_n(\mathbf{r}(t')) \right\} \exp(i\gamma_n(t)) |n(\mathbf{r}(t))\rangle, \quad (7.3)$$

where the first exponential term corresponds to a dynamical phase factor, and the second term is a geometric phase. By imposing that $|\psi(t)\rangle$ satisfies the time-dependent Schrödinger equation one finds that

$$\gamma_n(t) = i\langle n(\mathbf{r}) | \nabla_{\mathbf{r}} n(\mathbf{r}) \rangle \cdot \dot{\mathbf{r}}(t), \quad (7.4)$$

where the term

$$\mathbf{A}_n(\mathbf{r}) = i\langle n(\mathbf{r}) | \nabla_{\mathbf{r}} n(\mathbf{r}) \rangle \quad (7.5)$$

is usually referred to as the Berry connection³ or the Berry vector potential for reasons that will become apparent. Because eigenvectors can only be defined up to a global phase, \mathbf{A} is a gauge dependent quantity. If we make a gauge transformation such that $|n(\mathbf{k})\rangle \rightarrow e^{i\xi(\mathbf{k})} |n(\mathbf{k})\rangle$ then the Berry connection is also transformed as $\mathbf{A}_n(\mathbf{k}) \rightarrow \mathbf{A}_n(\mathbf{k}) - \nabla_{\mathbf{k}} \xi(\mathbf{k})$. However if we integrate the Berry connection on a closed loop

$$\gamma_n(\mathcal{C}) = \oint_{\mathcal{C}} \mathbf{A}_n(\mathbf{r}) \cdot d\mathbf{l}, \quad (7.6)$$

we obtain the Berry phase which, unlike the Berry connection, is gauge independent (modulo 2π).

An alternative way to compute Berry's phase uses Stokes's theorem from vector

³This is related to the connection defined in differential geometry that is used to describe things like parallel transport.

calculus

$$\oint_C \mathbf{A}_n \cdot d\mathbf{l} = \int_S \nabla \times \mathbf{A}_n \cdot d\mathbf{S} \\ = \int_S \boldsymbol{\Omega}_n \cdot d\mathbf{S}, \quad (7.7)$$

where the vector field $\boldsymbol{\Omega}_n = \nabla \times \mathbf{A}_n$ is known as the Berry curvature or Berry fieldT. By rewriting the Berry phase in this way, its resemblance with the definition of the Euler characteristic from Equation 7.1 becomes apparent.

Using some vector calculus identities the Berry curvature can be rewritten as

$$\begin{aligned} \boldsymbol{\Omega}_n &= i[\nabla_{\mathbf{r}} \langle n |] \times [\nabla_{\mathbf{r}} |n \rangle] \\ &= \sum_{j \neq n} i[\langle n | \nabla_{\mathbf{r}} |j \rangle] \times [\langle j | \nabla_{\mathbf{r}} |n \rangle] \\ &= i \sum_{j \neq n} \frac{\langle n | \nabla_{\mathbf{r}} \hat{H} |j \rangle \times \langle j | \nabla_{\mathbf{r}} \hat{H} |n \rangle}{(E_j - E_n)^2}, \end{aligned} \quad (7.8)$$

where $\langle n | \nabla_{\mathbf{r}} |j \rangle$ was replaced with $\langle n | \nabla_{\mathbf{r}} \hat{H} |j \rangle / (E_j - E_n)$ by differentiating Equation 7.2. This expression shows that $\boldsymbol{\Omega}_n$ is a gauge independent quantity as it does not depend on the derivatives of a particular gauge choice for $|n\rangle$ but rather on $\nabla_{\mathbf{r}} \hat{H}$ which is gauge independent. Also we can see that $\boldsymbol{\Omega}_n$ becomes singular when there are degeneracies present in the Hamiltonian, and these degeneracies act as ‘sources’ for the Berry connection. Finally, even though the system may remain in state $|n\rangle$ during the adiabatic evolution, this expression for the Berry curvature makes it explicit that other eigenstates of the Hamiltonian have an influence in the Berry phase acquired.

7.3.1 Aharonov-Bohm phase as an example of a Berry’s phase

A familiar example of geometric phases is the Aharonov-Bohm phase [67] gained by an electrons moving along closed trajectories around a solenoid. This phase was initially conceived as a way of showing that in quantum mechanics magnetic vector potentials, typically conceived only as mathematical objects, can have a physical effect on the wave function. They considered a coherent electron beam split into two paths around a solenoid that produces a magnetic field \mathbf{B} as shown in Figure 7.2. Outside the solenoid the magnetic field $\mathbf{B} = 0$, but there can be a non-zero magnetic vector potential such that $\mathbf{B} = \nabla \times \mathbf{A}$. The two beams are later recombined. Even though the electron’s trajectories are not modified, when looking at the interference pattern one finds that the two paths acquired different phases, and their difference is remarkably equal to magnetic flux piercing the area enclosed by the electrons path $\Delta\varphi = 2\pi\Phi_B/\Phi_0$, where $\Phi_0 = h/e$ is the flux quantum.

This Aharonov-Bohm phase can be interpreted as an example of a Berry phase in real space. For a charged particle in the presence of a vector potential the mo-

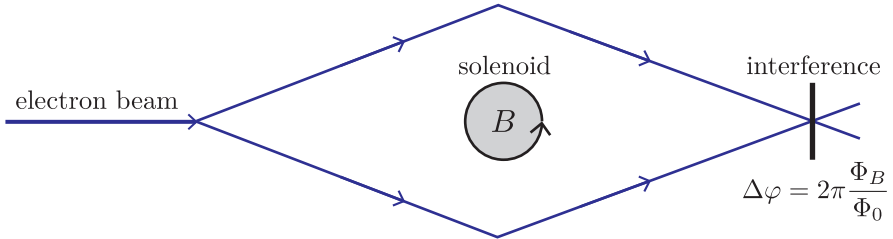


Figure 7.2: The Aharonov-Bohm experiment. A coherent electron beam is split into two paths surrounding a solenoid which produces a non-zero magnetic field \mathbf{B} inside the gray region and $\mathbf{B} = 0$ outside. The two beams are later recombined and an interference pattern reveals a phase difference $\Delta\varphi = 2\pi\Phi_B/\Phi_0$ equal to the magnetic flux enclosed by the electron's path.

momentum dependence of the free-particle Hamiltonian is modified $\mathbf{p} \rightarrow \mathbf{p} - q\mathbf{A}$ so that the wave function will depend on the magnetic vector potential as well. Using Equations 7.6 and 7.7 it can be shown that the Berry phase associated to a closed path around the solenoid is exactly equal to the Aharonov-Bohm phase:

$$\begin{aligned}\gamma_n(\mathcal{C}) &= \frac{e}{\hbar} \oint_C \mathbf{A}(\mathbf{r}) \cdot d\mathbf{r} \\ &= \frac{e}{\hbar} \int_S \nabla \times \mathbf{A} \cdot d\mathbf{S} \\ &= \frac{e\Phi_B}{\hbar},\end{aligned}\tag{7.9}$$

For this particular example, the Berry connection is exactly equal to the magnetic vector potential and the Berry curvature is the magnetic field. This gives us a very physical intuition for interpreting the Berry phase in terms of the ‘magnetic flux’ from abstract sources of ‘magnetic fields’ in parameter space.

7.3.2 Chern number

The Chern number is conventionally used to describe the topology of materials which have an underlying crystalline structure. According to Bloch’s theorem, the wave functions of a space periodic Hamiltonian can be written as $|\psi(\mathbf{k})\rangle = e^{i\mathbf{k}\cdot\mathbf{r}} |u(\mathbf{k})\rangle$, where $|u(\mathbf{k})\rangle$ are periodic wave functions. If we define the Bloch Hamiltonian

$$\hat{H}(\mathbf{k}) = e^{i\mathbf{k}\cdot\mathbf{r}} \hat{H}(\mathbf{r}) e^{-i\mathbf{k}\cdot\mathbf{r}},\tag{7.10}$$

their eigenvectors are given by $|u(\mathbf{k})\rangle$ and the eigenvalues define the band structure. Translational symmetry implies that $\hat{H}(\mathbf{k} + \mathbf{a}) = \hat{H}(\mathbf{k})$ where \mathbf{a} is a reciprocal lattice vector. The crystal momentum or quasimomentum is only defined within the periodic Brillouin zone and therefore can be mapped into a torus in d dimensions if we glue the edges together.

The Chern number of the n th band is defined as

$$C_n = \frac{1}{2\pi} \int_{BZ} \Omega_n d\mathbf{k}, \quad (7.11)$$

where the relevant parameter space is crystal momentum and the surface of integration corresponds to the BZ (a torus). The definition of Chern number is closely related to the definition of the Berry phase from Equation 7.7. For our previous example of a quantum Hall system, the integer proportionality factor in the quantized conductance is exactly equal to the Chern number.

Just like two-dimensional surfaces are classified by the integral of their Gaussian curvature, the topology of Bloch bands and of quantum systems in general is determined by the integral of the Berry curvature. In a similar way, the integral connects local properties of a quantum system, the Berry connection, with a global topological invariant, the Chern number. One subtle difference is that the Euler characteristic is only determined by the surface (and its intrinsic Gaussian curvature) while the Chern number is defined both by a surface (the BZ) and an additional local curvature (the Berry curvature). By studying different Hamiltonians one can obtain a different Berry curvature, but the geometry of the BZ and thereby the surface of integration is typically defined by a torus⁴. This difference will be important later on when we describe the experiments performed to study a system with Rashba spin-orbit coupling and an unconventional topology.

7.4 The bulk-edge correspondence principle

Earlier I mentioned that topological systems provide very robust channels for transporting things like electrical current and light. This transport phenomena typically arises when there is a spatial interface between two topologically distinct phases. The electrons skipping orbits at the interface of a (topological) quantum Hall material and (trivial) vacuum are one example of this. Notice that for this particular example the modes propagate along a given direction, they are chiral. In general one can expect to have modes moving along two directions, and the difference between the number of these modes $N_L - N_R$ is fixed and determined by the topology of the bulk states. The bulk-edge correspondence principle relates the difference in the number of these modes with the bulk topology of the materials at the interface:

$$\Delta C = N_R - N_L \quad (7.12)$$

where ΔC is the difference of Chern number on the interface.

⁴In next chapter we consider a case where this breaks down.

7.5 Example: two-level model

Many of the concepts introduced in the previous section can be readily applied and understood using a two-level model

$$\hat{H}(\mathbf{k}) = \mathbf{h}(\mathbf{k}) \cdot \hat{\boldsymbol{\sigma}} \quad (7.13)$$

where $\hat{\boldsymbol{\sigma}} = (\sigma_x, \sigma_y, \sigma_z)$ are the Pauli matrices and $\mathbf{h}(\mathbf{k}) = (h_x(\mathbf{k}), h_y(\mathbf{k}), h_z(\mathbf{k}))$ are functions of \mathbf{k} . This model has been used to describe a number of physical systems like graphene [55] and spin-orbit coupled systems [59, 68]. Let us now consider the simple case $h(\mathbf{k}) = \mathbf{k}$, for which $\nabla_{\mathbf{k}} \hat{H} = \boldsymbol{\sigma}$ and using Equation 7.8 it can be shown that

$$\boldsymbol{\Omega} = -\frac{\mathbf{h}}{2h^3} \quad (7.14)$$

which can be recognized as the field of a Dirac monopole [69] with charge $-1/2$. The degeneracy in the energies that gives rise to the monopole is known as a Dirac point as the energies in that vicinity resemble the dispersion of a massless Dirac particle. It follows from Equation 7.14 that the Berry phase gained by moving in a closed path \mathcal{C} is equal to the flux from the monopole in the surface enclosed by \mathcal{C} as is shown in Figure 7.3. This connects nicely with our intuition from the Aharonov-Bohm effect. For a closed surface enclosing the Dirac point, the Chern number is an integer equal to 1.

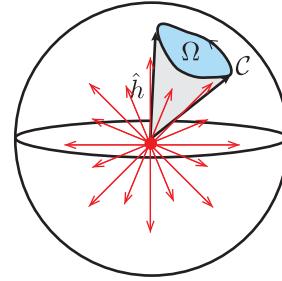


Figure 7.3: For a two-level system, the Berry curvature from a Dirac point can be viewed as a Dirac monopole in momentum (parameter) space. The Chern number can be interpreted as the flux from the monopole on the solid angle subtended by the vector $\hat{h}(\mathbf{k})$ or alternatively as the number of times $\hat{h}(\mathbf{k})$ wraps around a unit sphere.

For a Hamiltonian with arbitrary $\mathbf{h}(\mathbf{k})$ we can define a normalized vector $\hat{h} = \mathbf{h}/|\mathbf{h}|$ and the Chern number takes the form

$$C = \frac{1}{4\pi} \int (\partial_{k_x} \hat{h} \times \partial_{k_y} \hat{h}) \cdot \hat{h} d\mathbf{k} \quad (7.15)$$

and can be interpreted as the number of times that the vector $\hat{h}(\mathbf{k})$ wraps around a unit sphere [70], a quantity that is known as the winding number.

7.6 Monopoles and Dirac strings

We just gained some intuition about interpreting the Chern number as the flux from Dirac monopoles. But if we stick to our knowledge of electromagnetism we might remember that monopoles are forbidden since

$$\int_S \mathbf{B} \cdot d\mathbf{S} = \int_V (\nabla \cdot \mathbf{B}) dV \quad (7.16)$$

and $\nabla \cdot \mathbf{B} = \nabla \cdot (\nabla \times \mathbf{A}) = 0$. So how is this possible? The solution to this problem was envisioned by Dirac [69] and is now called a Dirac string. If we consider a semi-infinitely long and infinitesimally thin solenoid, the magnetic field in the finite end will resemble that of a monopole as can be seen in Figure 7.4. This tiny solenoid corresponds to the Dirac string. A more mathematical interpretation of

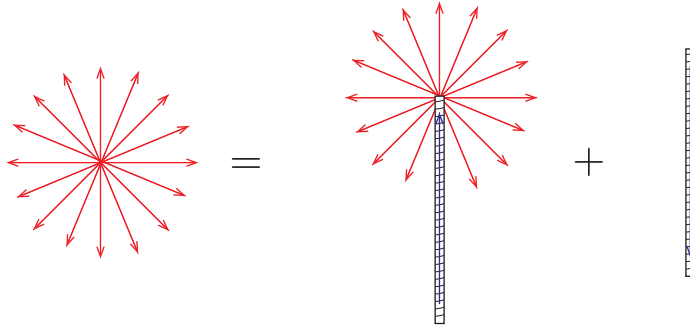


Figure 7.4: For a two-level system, the Berry curvature from a Dirac point can be viewed as a Dirac monopole in momentum (parameter) space. The Chern number can be interpreted as the flux from the monopole on the solid angle subtended by the vector $\hat{h}(\mathbf{k})$ or alternatively as the number of times $\hat{h}(\mathbf{k})$ wraps around a unit sphere.

these strings comes from the fact that the vector potential of a monopole has ‘lines’ where it becomes singular. For example for a particular gauge we can write

$$\mathbf{A}(\mathbf{r}) = g \frac{-y\mathbf{e}_x + x\mathbf{e}_y}{r(r+z)} \quad (7.17)$$

which is singular for the negative z axis where $z = -r$. The orientation of the Dirac string is gauge dependent, something that should not surprise or bother us at this point. However, the physical effects of the Dirac string should be gauge independent, or in other words, the Aharonov-Bohm phase gained by a charged particle moving in a path that encloses the string should be an integer multiple

of 2π . This argument gives rise to the Dirac charge quantization [69], and in the context of topology, it guarantees that when we calculate the Berry phase by integrating the Berry connection (vector field) along a path that enclose a Dirac string, its effect will be indistinguishable.

7.7 Conclusions

Topology plays a very important role both in math and in physics. In this Chapter I reviewed the basic concepts of topology in the context of condensed matter physics that will be relevant for our experiments with unconventional topology. As a closing remark, Figure 7.5 summarizes the main concepts that were introduced and is a reminder that topological invariants are global properties defined in terms of integrals of local properties. Furthermore, we can use our intuition from electromagnetic theory to interpret topological invariants in quantum mechanics.

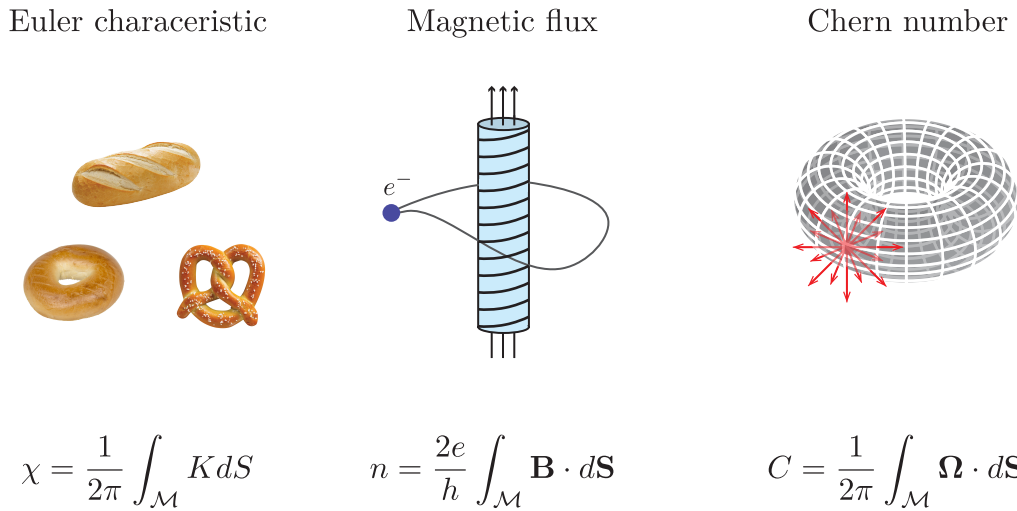


Figure 7.5: The Euler characteristic and the Chern number are topological invariants defined by integrals of local curvatures. The Aharonov-Bohm phase gives us physical intuition to interpret the Chern number as the flux from a ‘Berry field’.

Chapter 8: Unconventional topology with a Rashba SOC quantum gas

As I mentioned in the previous Chapter topological order is present in a wide range of physical systems and is quantified by integer valued topological invariants such as the Chern number. In this Chapter I describe the experiments to engineer and characterize the topology of a quantum gas with Rashba-type SOC. Our system broke from the conventional mold of topological materials and I show that its resulting topological indices can take both integer and half-integer values. If the concept of half-integer invariants does not sound odd to you should think of a donut with half a hole.

Ultracold atomic systems are an emerging platform for engineering topological lattices, from the Harper-Hofstadter model [71, 72], the Haldane model [73], to the Rice-Mele model [74, 75] as well as assembling spin-orbit coupled lattices without analogues in existing materials [76, 77].

Experimental realizations of topological materials have mostly focused on engineering different topological bands (with different Berry curvatures) in lattice systems, where the BZ is always a torus. Here I show that by eliminating the lattice potential and thereby changing the BZ from \mathbb{T}^2 to \mathbb{R}^2 , i.e. from a torus to a Cartesian plane, it is possible to create topological branches of the dispersion relation with half-integer Chern number. In our experiments we created both topological and non-topological dispersion branches by introducing Rashba-like SOC [78–80] to a cold quantum gas.

This Chapter is organized in the following way: First I will give a general overview of Rashba SOC and will describe theoretical proposals for engineering this type of coupling in ultracold atom systems. Then I will describe our experimental implementation of Rashba SOC in the lab using a trio of Raman coupled CDD states (Chapter 6) and validate our quantum engineering using Fourier transform spectroscopy (Chapter 5). Finally I will describe a quantum state tomography procedure to measure the eigenstates of our system, and directly obtain the Chern number.

To avoid confusion between dressed state xyz labels and Cartesian coordinates, in this Chapter I will use the numbers 1, 2, 3 to label the coordinates $\mathbf{e}_x, \mathbf{e}_y, \mathbf{e}_z$ and the letters x, y, z to label dressed state parameters.

8.1 Rashba spin-orbit coupling

Rashba SOC [59] appears in condensed matter systems where electrons are confined in a 2D plane and experience an intrinsic out-of-plane electric field. If the electron's momentum is given by $\hbar\mathbf{k} = \hbar(k_x\mathbf{e}_x + k_y\mathbf{e}_y)$ and the electric field is $\mathbf{E} = E\mathbf{e}_z$, in the electron's moving frame there will be a momentum dependent magnetic field $\mathbf{B}_{\text{SOC}} = -\hbar\mathbf{k}/m \times \mathbf{E}/c^2 = \hbar E/mc^2(-k_y, k_x, 0)$. The interaction between the electron's spin with this field through the magnetic Zeeman interaction $-\mu \cdot \mathbf{B}_{\text{SOC}}$ gives rise to the SOC Hamiltonian

$$\hat{H}_{\text{SOC}} = \frac{2\alpha}{m}(k_y\hat{\sigma}_x - k_x\hat{\sigma}_y) \quad (8.1)$$

where $\alpha = g\mu_B E/c^2$, g is the electrons gyromagnetic ratio, μ_B is the Bohr magneton and $\hat{\sigma}_i$ are the Pauli matrices.

As can be seen in Figure 8.1, the Rashba dispersion relation is characterized by having a Dirac point located at $\mathbf{k} = 0$ (see Chapter 7.5) and a degenerate ground state that is described by the ring $k_x^2 + k_y^2 = \alpha^2$. If we combine Equation 8.1 with the free particle Hamiltonian the Hamiltonian can be written as $\hat{H} = (\hbar\mathbf{k} - \hat{\mathbf{A}})^2/2m$ where $\hat{\mathbf{A}} = \alpha(\hat{\sigma}_y\mathbf{e}_x - \hat{\sigma}_x\mathbf{e}_y)$ can be interpreted as a (matrix valued) non-abelian gauge potential whose elements do not commute. This term is closely related to the Berry connection discussed in Chapter 7.3. This in combination with the presence of the Dirac point hints to us that a system with Rashba SOC has non-trivial topology.

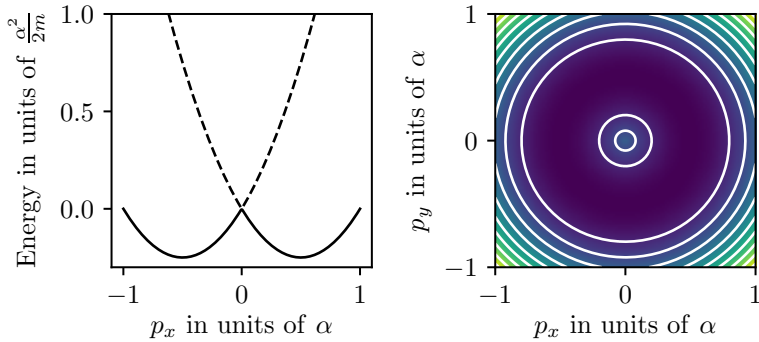


Figure 8.1: The Rashba dispersion relation has a Dirac point located at $\mathbf{k} = 0$ and

SOC is also a necessary ingredient for realizing \mathbb{Z}_2 topological insulators and the quantum spin-Hall effect. Furthermore, the degeneracy of the ground state single particle eigenstates could open the possibility of studying strongly correlated phases in the presence of interactions for systems of both fermions and bosons [81–83]. SOC systems offer the possibility of studying a wide range of interesting physics and naturally using ultracold atomic systems to engineer SOC, and in particular Rashba type SOC, has been a longstanding goal [84].

8.2 Rashba SOC for neutral atoms

Proposals for engineering Rashba type SOC in neutral atoms consist in using lasers to link internal states of an atom with its linear momentum. In order to achieve non-trivial gauge potentials it is necessary to couple $N \geq 3$ levels (see [85]). I will describe the proposal by [78] which considers a ‘ring coupling’ which is shown in Figure 8.2 for the case of $N = 3$. The states $|j\rangle$ represent internal atomic states and they are linked to each other with complex valued matrix elements $\frac{\Omega_j}{2} e^{i\mathbf{k}_j \cdot \mathbf{x}}$, where \mathbf{k}_j is a momentum transfer associated with the $|j\rangle \rightarrow |j+1\rangle$ transition and $\Omega_i = e^{i\phi_i} |\Omega|$ represents the coupling strength. We require that $\sum \mathbf{k}_i = 0$ so that no momentum is transferred when a closed loop $|1\rangle \rightarrow |2\rangle \dots \rightarrow |N\rangle \rightarrow |1\rangle$ is completed. For this case the \mathbf{k}_i momenta vectors can be written as $\mathbf{k}_j = \mathbf{K}_{j+1} - \mathbf{K}_j$, and we make $\mathbf{K}_j = k_L \sin(2\pi j/N) \mathbf{e}_x + k_L \cos(2\pi j/N) \mathbf{e}_y$, corresponding to the vertices of an N sided regular polygon. We can further make a gauge transformation such that we can replace the phases ϕ_i associated to each coupling with $\bar{\phi} = \sum_i \phi_i / N$.

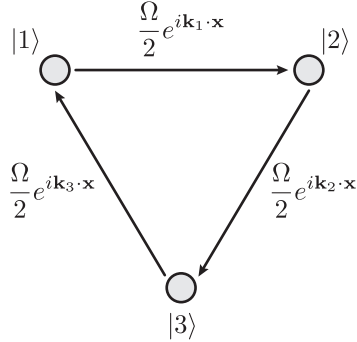


Figure 8.2: The Rashba ring coupling. To generate Rashba SOC in a system of cold atoms it is necessary to cyclically couple $N \geq 3$ internal states such that the transition $|j\rangle \rightarrow |j+1\rangle$ has a momentum transfer \mathbf{k}_j and $\sum_j \mathbf{k}_j = 0$ such that there is no momentum transfer for a closed loop $|1\rangle \rightarrow |2\rangle \dots |N\rangle \rightarrow |1\rangle$. The ring coupling combined with the free particle Hamiltonian give rise to a 2-level subspace that can be described to first order by the Rashba Hamiltonian

The Hamiltonian describing this coupling along with the kinetic term is

$$H_{j,j'} = \frac{\hbar^2 k^2}{2m} \delta_{j,j'} + \frac{\Omega}{2} (e^{i(\bar{\phi} + \mathbf{k}_j \cdot \mathbf{x})} \delta_{j,j'+1} + \text{h.c.}), \quad (8.2)$$

and after applying the unitary transformation $U_{j,j'} = \exp[i\mathbf{K}_j \cdot \mathbf{x}] \delta_{j,j'}^{\dagger}$ ¹ it gets transformed to

$$H_{j,j'} = \frac{\hbar^2}{2m} |\mathbf{q} + \mathbf{K}_j|^2 \delta_{j,j'} + \frac{\Omega}{2} (e^{i\bar{\phi}} \delta_{j,j'+1} + \text{h.c.}), \quad (8.3)$$

where I have replaced the momentum \mathbf{k} by the quasimomentum \mathbf{q} . The off diagonal

¹This transformation is equivalent to applying a state dependent momentum boost $\mathbf{k} \rightarrow \mathbf{k} + \mathbf{K}_j$

terms of Equation 8.3 can be related to a 1D periodic tight-binding Hamiltonian with hopping elements $\Omega/2$ where the internal states $|j\rangle$ represent lattice sites and completing one loop corresponds to gaining a ‘flux’ of $N\bar{\phi}$. It is helpful to write the Hamiltonian in a basis that is conjugate to the index j

$$|l\rangle = \frac{1}{\sqrt{N}} \sum_{j=1}^N e^{i2\pi jl/N} |j\rangle \quad (8.4)$$

where the index l is analogous to the crystal momentum index for a Bloch Hamiltonian. In this new basis, terms with oscillatory components (e.g. $|\mathbf{q} + \mathbf{K}_j|\rangle$) in the diagonals are displaced to the off-diagonal and oscillatory terms in the off diagonal are displaced to the diagonal. Under this basis the Hamiltonian starts looking very much Rashba-like

$$H_{l,l'} = \left[\frac{\hbar^2}{2m} (q^2 + k_L^2) + E_l \right] \delta_{l,l'} + \frac{\hbar^2 k_L}{m} [(iq_x + q_y)\delta_{l-1,l'} + \text{h.c.}] \quad (8.5)$$

where $E_L = 2\hbar\Omega \cos(2\pi l/3 + \bar{\phi})$ correspond to the eigenenergies when $q = 0$. The phase $\bar{\phi}$ can be tuned such that a pair of states with consecutive l index become degenerate, indicating the presence of a Dirac point at $q = 0$. Figure 8.3 shows the energies E_l for $N = 3$ and $\bar{\phi} = 0$.

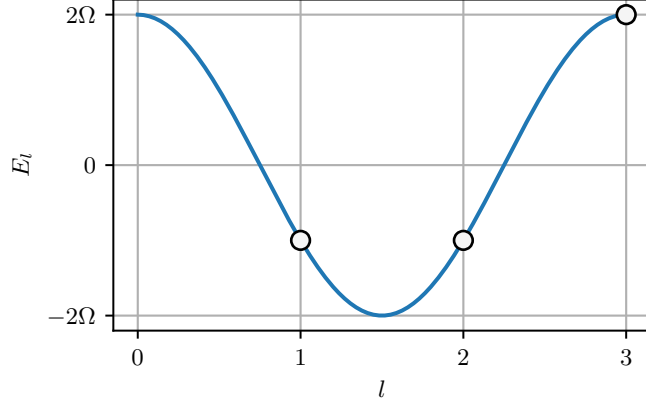


Figure 8.3: Eigenenergies of Equation 8.5 for $q = 0$ for $N = 3$ and $\bar{\phi} = 0$. For this particular choice of phase, the energies of the $l = 1$ and $l = 2$ states become degenerate

We can consider the degenerate states corresponding to two consecutive $|l\rangle$ states as pseudospins which are described to zeroth order by the Rashba plus free particle Hamiltonian

$$\hat{H}^{(0)} = \frac{\hbar^2 q^2}{2m} + \frac{\hbar^2 k_L}{m} (\hat{\sigma}_x q_y - \hat{\sigma}_y q_x), \quad (8.6)$$

with spin orbit coupling strength given by $\alpha = \hbar^2 k_L / 2$. The zeroth-order Hamiltonian has continuous rotational symmetry while we the proposed ring coupling only has only discrete rotational symmetry. The symmetry of the Hamiltonian is recovered when higher order corrections of the Hamiltonian are included. The complete expressions for the higher order terms for $N = 3$ and $N = 4$ can be found in [78], and they are reminiscent of quadratic and cubic Dresselhaus SOC [86]. The largest leading order term is inversely proportional to Ω^2 so that this ring-coupling scheme results in a more ‘Rashba-like’ Hamiltonian as one goes to higher coupling strengths. Figure 8.4 shows level curves of the ground state eigenenergies of Equation 8.5 for $N = 3$ and $\bar{\phi} = 0$ for increasing Ω . At low Ω the dispersion has discrete rotational symmetry and is characterized by three local minima. As Ω is increased the local minima start merging into each other and in the large Ω limit we recover the characteristic Rashba ring-like dispersion.

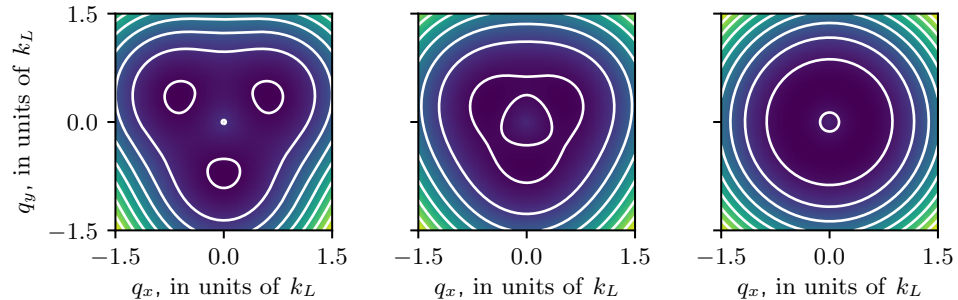


Figure 8.4: Ground state dispersion relation of Equation 8.5 for $N = 3$ and $\bar{\phi} = 0$ for $\Omega = 1.75 E_L$ (left), $\Omega = 3.5 E_L$ (middle) and $\Omega = 175 E_L$ (right). Higher order corrections to $\hat{H}^{(0)}$ decay as $1/\Omega^2$ and in the large Ω limit we recover the Rashba ring dispersion.

8.3 Experimental implementation of Rashba SOC

We implemented the ring-coupling scheme and thereby engineered Rashba SOC by resonantly coupling three internal atomic states using two-photon Raman transitions [19] as depicted in Figure 8.5. As shown in Figure 8.5a, the engineered system consisted of an effective spin-1/2 Rashba subspace, along with a topologically trivial high-energy branch. Our engineered Rashba system had a single Dirac cone near $\mathbf{q} = 0$, where the two lower dispersion branches become degenerate and the Berry curvature becomes singular. Each of these branches extend to infinite momentum, making the supporting manifold a plane rather than a torus. We characterized this system using both spectroscopy and quantum state tomography. This allowed us to measure the dispersion branches and directly observe the single Dirac point linking the lowest two branches as well as to reconstruct the Berry connection to derive the associated Chern numbers.

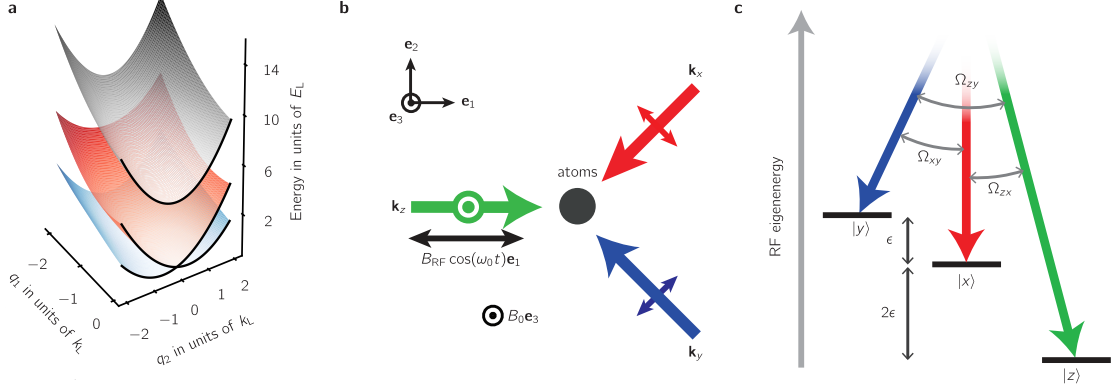


Figure 8.5: **a** Our engineered dispersion consisted of a two-level Rashba subspace (red and blue) with a single Dirac point linking the lowest two branches and a topologically trivial higher branch (gray). **b** We generated $|xyz\rangle$ states by combining a bias magnetic field along \mathbf{e}_3 with an RF magnetic field oscillating along \mathbf{e}_1 . These states were coupled by three cross-polarized Raman laser beams propagating along \mathbf{e}_1 , $\mathbf{e}_2 - \mathbf{e}_1$ and $-\mathbf{e}_1 - \mathbf{e}_2$. **c** Each pair of Raman lasers was in two-photon resonance with a single transition between the $|xyz\rangle$ states which we coupled strengths $(\Omega_{zx}, \Omega_{xy}, \Omega_{yz})/2\pi = (12.6(5), 8.7(8), 10(1))$ kHz.

All of our experiments started with about $N \approx 1 \times 10^{687}$ Rb atoms in a crossed optical dipole trap [87], with frequencies $(f_1, f_2, f_3) \approx (70, 85, 254)$ Hz, just above the transition temperature for Bose-Einstein condensation. We initially prepared the atoms in the $|F = 1, m_F = -1\rangle$ state of the $5S_{1/2}$ electronic ground state and transferred atoms to the $m_F = 0$ and $m_F = +1$ states as needed using ARP. A bias field $B_0 \mathbf{e}_3$ gave a $\omega_0/2\pi = 23.9$ MHz Larmor frequency along with a quadratic shift of $\epsilon/2\pi = 83.24$ kHz. The experiments were performed using the $|xyz\rangle$ states described in Chapter 6. We implemented CDD using an RF magnetic field oscillating at the Larmor frequency with strength $\Omega_{RF} = 1.41(2)\epsilon$. We adiabatically prepared the $|xyz\rangle$ states starting from the m_F states following the procedure described in Chapter 6.4.

8.3.1 Raman coupling the $|xyz\rangle$ states

We Raman-coupled atoms prepared in any of the $|xyz\rangle$ states using the three cross-polarized Raman laser beams shown in Figure 8.5b, tuned to the ‘magic zero’ wavelength $\lambda_L = 790$ nm. We arranged the Raman lasers into the tripod configuration shown in Figure 8.5c, bringing each pair into two-photon resonance with a single transition with strengths $(\Omega_{zx}, \Omega_{xy}, \Omega_{yz})/2\pi = (12.6(5), 8.7(8), 10(1))$ kHz. The geometry of our experimental implementation differs from [19] where all Raman lasers are perpendicular. We had to go away from this configuration because we were interested in having all of the Raman recoil vectors lying on the imaging

plane so we could image all the Raman induced \mathbf{k} dependent dynamics. As a result of this the dispersion relation no longer has discrete rotational symmetry, however the Dirac point is very robust against changes in Hamiltonian parameters.

The energies of the $|xyz\rangle$ states are $\omega_x = 0$ and $\omega_{z,y} = -(\epsilon \pm \sqrt{4\Omega_{\text{RF}}^2 + \epsilon^2})/2$. We set the frequencies of the Raman lasers to $\omega_x = \omega_L + \omega_0 + \omega_{xy}$, $\omega_y = \omega_L + \omega_0$ and $\omega_z = \omega_L - \omega_{zx}$, where $\omega_L = 2\pi c/\lambda_L$ and $(\omega_{zx}, \omega_{xy}, \omega_{zy})/2\pi = (166.47, 83.24, 249.71)$ kHz are the transition frequencies between pairs of dressed states and are integer multiples of ϵ for our coupling strength $\Omega = \sqrt{2}\epsilon$.

The Raman coupled states can be described by the combined kinetic and light-matter Hamiltonian

$$\hat{H}_{\text{R}}(\mathbf{k}) = \sum_{j \in \{xyz\}} \left(\frac{\hbar^2 k^2}{2m} + \hbar\omega_i \right) |j\rangle \langle j| + \sum_{j' \neq j} \hbar\Omega_{j,j'} e^{i(\mathbf{k}_{j,j'} \cdot \mathbf{x} - i\omega_{j,j'} t)} |j\rangle \langle j'|, \quad (8.7)$$

where $\mathbf{k}_{j,j'}$ is the recoil momentum from an $|j\rangle \rightarrow |j'\rangle$ transition and Ω_{ij} is the Raman coupling strength between a pair of RF dressed states. The Hamiltonian above only includes the matrix elements associated to resonant couplings. We apply the unitary transformation $\hat{U}_{j,j'} = \exp(-i\mathbf{k}_j \cdot \mathbf{x} - \omega_j t) \delta_{j,j'} |j\rangle \langle j'|$ so that the Hamiltonian takes the familiar form of the ring coupling scheme

$$\hat{H}_{\text{R}} = \sum_{j \in \{xyz\}} \left(\frac{\hbar^2(\mathbf{q} - \mathbf{k}_j)^2}{2m} + \hbar\delta_j \right) |j\rangle \langle j| + \sum_{j \neq j'} \hbar\Omega_{jj'} |j\rangle \langle j'|, \quad (8.8)$$

where \mathbf{k}_j are the Raman wave vectors and δ_j is the detuning from Raman resonance.

This coupling scheme simultaneously overcomes three limitations of earlier experiments [79, 80] that performed the ring coupling using a combination of states in the $F = 1$ and $F = 2$ hyperfine manifolds of ${}^4\text{OK}$: (1) working in the same hyperfine manifold eliminates spin-relaxation collisions [88]; (2) unlike m_F states, the $|xyz\rangle$ states can be tripod-coupled with lasers far detuned relative to the excited state hyperfine splitting greatly reducing spontaneous emission [43]; and (3) CDD renders the $|xyz\rangle$ states nearly immune to magnetic field noise. [TO THINK: understand what is the deal with spin-relaxation collisions, also what is the deal with coupling far detuned stuff]

8.3.1.1 Floquet and off resonant coupling effects

We operated in a regime where the transition energies between the $|xyz\rangle$ states were integer multiples of ω_{xy} : $\omega_{zx} = 2\omega_{xy}$ and $\omega_{zy} = 3\omega_{xy}$, and therefore we can use Floquet theory for a complete description of our system [89]. The Hamiltonian in Equation 8.8 is therefore an effective Hamiltonian that describes the stroboscopic dynamics of the full Floquet Hamiltonian. We observed that the effective Raman coupling strengths for the driven three level system differed from our calibrations which were performed by only driving one pair of states because of the presence of nearby quasi-energy manifolds. This effect could be mitigated for larger values of ω_{xy} as the spacing between quasi-energy manifolds is increased. Appendix A has a

full derivation of the Raman Hamiltonian starting from the $|m_F\rangle$ basis in the lab frame including the full time dependence and off resonant terms which can also modify the Hamiltonian parameters.

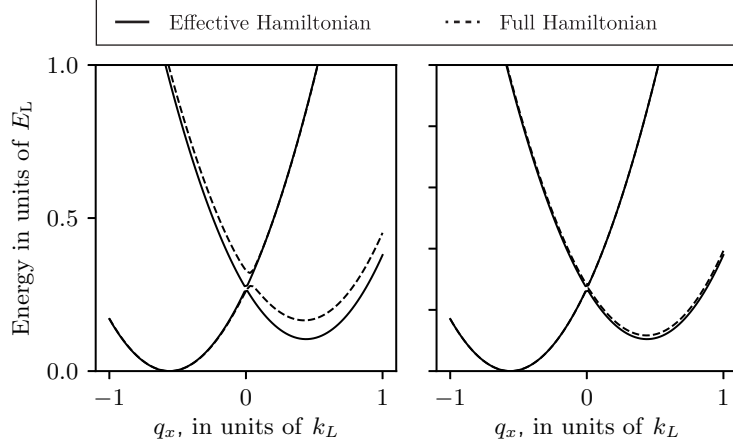


Figure 8.6: Solid lines: Dispersion relation from the effective Floquet Hamiltonian from Equation 8.8 as a function of q_x for $\Omega_{i,j} = 1.5 E_L$ and $\delta_i = 0$. Dashed lines: Dispersion relation computed for the full Floquet Hamiltonian. We considered $\omega_{zx} = 2\omega_{xy}$ and $\omega_{zy} = 3\omega_{xy}$ in both cases so the separation between Floquet manifolds is ω_{xy} . In the left panel $\omega_{xy} = 83.24$ kHz as in our experiments and in the right panel $\omega_{xy} = 416.2$ kHz. As the spacing between Floquet manifolds becomes larger, the dispersion from the effective and full Hamiltonians become closer.

8.3.1.2 Lifetime

There was a lot of concern when we first started setting up to do this experiments about the lifetime of the system due to spontaneous emission being to short. This was in part one of the reasons why we pursued the topology direction rather than trying to measure a fragile many-body phase. The measured spontaneous emission limited lifetime of our system was 320(17) ms. However it was reduced to 40(2) ms when we Raman couple the $|xyz\rangle$ states, which we attribute to technical noise in the relative phase between the RF dressing field and the Raman laser fields, which has caused considerable consternation in ongoing experiments. All the experiments reported here were short compared to this timescale so this decreased lifetime was not an issue but it is a limitation that needs to be addressed for future experiments. Figure 8.7 shows measurements of the lifetimes of Raman dressed atoms in both $|m_f\rangle$ and $|xyz\rangle$ states. We obtained the lifetime by fitting decaying exponentials to the integrated OD from TOF images of thermal atoms where the Raman was turned on in 1 ms and held on for up to $50 \mu s^2$.

²How long we could hold on the Raman was limited by the RF antenna heating up.

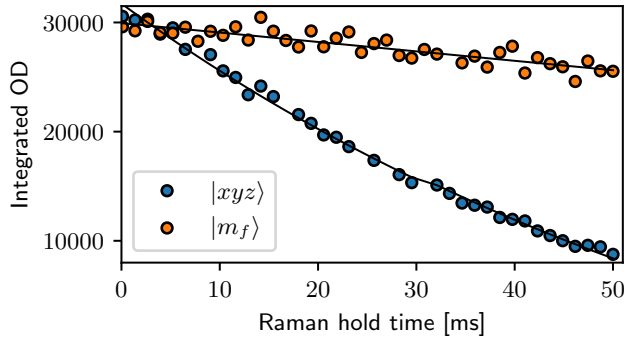


Figure 8.7: Lifetime of Raman dressed states. We Raman dressed atoms in the $|m_f\rangle$ and $|xyz\rangle$ states. The orange markers correspond to atoms initially prepared in $|m_f = -1\rangle$ (no high power RF involved) and the blue markers correspond to atoms $|xyz\rangle$ (three averaged traces). The lifetime of doubly dressed states is significantly reduced as compared to the lifetime of the Raman dressed $|m_f\rangle$ states, indicating that resonant scattering of photons is not our only loss mechanism.

8.3.2 Measuring quasimomentum distributions

Each pair of Raman lasers coupled states $|i, \mathbf{k}\rangle \rightarrow |j, \mathbf{k} + \mathbf{k}_{i,j}\rangle$ where $|i\rangle$ and $|j\rangle$ denote the initial and final $|xyz\rangle$ states, \mathbf{k} is the initial momentum and $\mathbf{k}_{i,j} = \mathbf{k}_i - \mathbf{k}_j$ is the two-photon Raman recoil momentum. Dressed states with quasimomentum \mathbf{q} are comprised of three bare states $|j, \mathbf{k}\rangle$ with momentum $\mathbf{k} = \mathbf{q} - \mathbf{k}_j$. The eigenstates of our Rashba SOC Hamiltonian take the form

$$|\Psi_n(\mathbf{q})\rangle = \sum_{j \in xyz} \sqrt{a_{n,j}(\mathbf{q})} e^{i\phi_{n,j}(\mathbf{q})} |j, \mathbf{k} = \mathbf{q} - \mathbf{k}_j\rangle, \quad (8.9)$$

where the quasimomentum \mathbf{q} is a good quantum number and the amplitudes are parametrized by $a_{n,j}(\mathbf{q})$ and $\phi_{n,j}(\mathbf{q})$. We leveraged the wide momentum distribution of a non-condensed ensemble ($T \approx 180$ nK and $T/T_c \approx 1.1$) to sample a wide range of momentum states simultaneously. By starting separately in each of the $|xyz\rangle$ states we sampled the range of quasimomentum states shown in Figure 8.8b, where the momentum distributions of an initial state $|j, \mathbf{k}\rangle$ is shifted from $\mathbf{q} = 0$ by the corresponding Raman wave vector \mathbf{k}_j .

Our measurement protocol consisted of abruptly removing the confining potential and the Raman lasers, initiating a 21 ms TOF. During this TOF we adiabatically transformed each of the $|xyz\rangle$ states back to a corresponding $|m_F\rangle$ state following the same procedure described in Chapter 6.4 and spatially separated them using a Stern-Gerlach gradient. Finally we used resonant absorption imaging to measure the resulting density distributions.

The FWHM of the cloud after TOF is about $700 \mu\text{m}$ which is much larger than the size of the in-situ cloud $\sim 50 \mu\text{m}$ and therefore the spatial density distribution

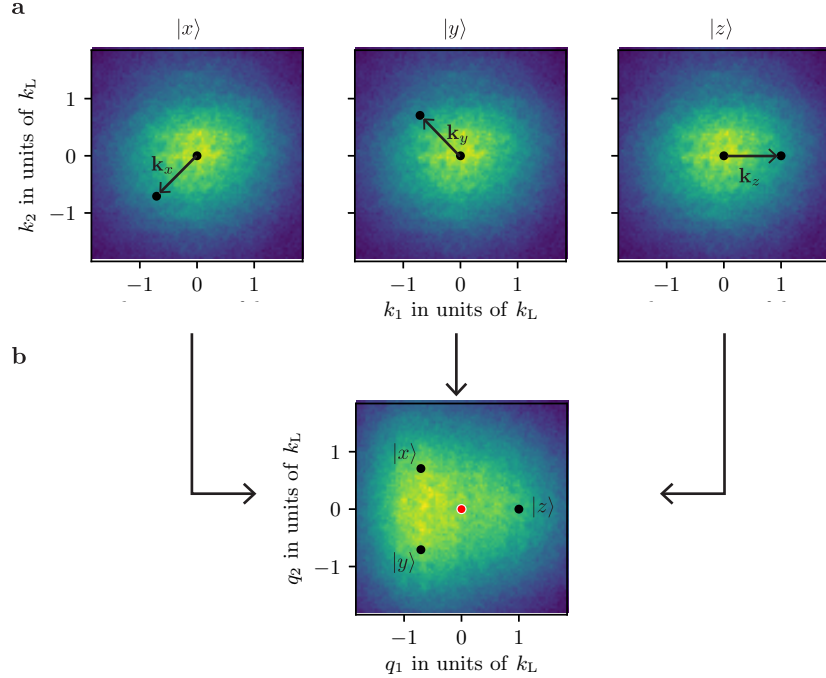


Figure 8.8: Mapping momentum into quasimomentum: **a** We used non-condensed atoms with a broad momentum distribution ($T \approx 180$ nK and $T/T_c \approx 1.1$). **b** Atoms in $|j, \mathbf{k}\rangle$ are mapped to Raman dressed states with quasimomentum $\mathbf{q} = \mathbf{k} + \mathbf{k}_j$. The black dots in the bottom panel represent the location of $\mathbf{k} = 0$ for each of the $|xyz\rangle$ states and the red dot corresponds to $\mathbf{q} = 0$. We performed our experiments starting separately in each of the $|xyz\rangle$ states, which allowed us to sample a larger range of quasimomentum states.

of the TOF images represents momentum distribution of the atoms. For the $7.4 \mu\text{m}$ pixel size of our camera and the 3.283 magnification of our imaging system, the momentum resolution of our images was $0.018 k_L$ and the momentum distributions after TOF had a FWHM of $\sim 2.2 k_L$.

8.3.2.1 Correcting shears from gradients

The SG field had a non-zero curvature which caused a compression (or expansion) of the $m_f = -1$ (+1) cloud in the direction perpendicular to the SG direction. The projections of a given momentum state \mathbf{k} along the SG axis and perpendicular to it were transformed as $k_{\parallel} \rightarrow k_{\parallel}$ and $k_{\perp} \rightarrow (1 + \alpha)k_{\perp}$, where $\alpha = 0$ for $m_f = 0$ and $\text{sign}(\alpha) = \pm 1$ for $m_f = \pm 1$. Since all our measurements were momentum dependent we had to take special care to quantify and correct this effect on the TOF images.

We used two different methods to quantify these shears. First we prepared thermal atoms in all three of the m_f states and fit 2D Gaussians rotated by the angle of the SG displacement; 63.8 degrees for our images. Figure 8.9 shows the

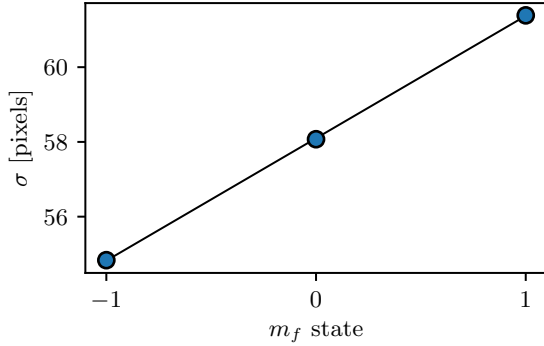


Figure 8.9: We measured the standard deviation of the momentum distribution along the axis perpendicular to the SG for 10 shots on each m_f state. From the slope of the linear fit we obtain a shearing parameter $\alpha \approx \pm 0.067$ for $m_f = \pm 1$.

standard deviation extracted from the Gaussian fits along the axis perpendicular to the SG deviation as a function of m_f state. We performed a liner fit of σ and found that the $m_f = \pm$ states are expanded/contracted by about $\pm 6.7\%$.

Alternatively we performed the Ramsey interferometer described in Section 8.5 but coupling only 2 states, either $|z\rangle \leftrightarrow |x\rangle$ or $|x\rangle \leftrightarrow |y\rangle$ (mapped to $| -1 \rangle \leftrightarrow | 0 \rangle$ and $| 0 \rangle \leftrightarrow | +1 \rangle$ after TOF). We looked at the oscillation frequencies on each pixel and fit them to Equation 8.16 for fixed value of the recoil momentum $\mathbf{k}_{i,j}$ and with a free shear parameter that modifies \mathbf{q} . Using this method we extracted a shearing of the order of 7%, in good agreement with the Gaussian fitting method.

The transformed momentum coordinates were described by a function $g(\mathbf{k}) = \mathbf{k}^{(\text{shear})}$ and our observed data $(y_i^{(\text{shear})}, \mathbf{k}^{(\text{shear})})$ was the OD in the sheared coordinate system at the i th pixel of the CCD sensor. The OD in the unsheared coordinate were estimated using

$$y_j = \frac{\sum_i \exp[-(g(\mathbf{k}_j) - \mathbf{k}_i^{(\text{shear})})^2/2\sigma^2] y_i^{(\text{shear})}}{\sum_i \exp[-(g(\mathbf{k}_j) - \mathbf{k}_i^{(\text{shear})})^2/2\sigma^2]}, \quad (8.10)$$

where we used σ as the spacing between points in the unsheared coordinate sytem. Prior to any data analysis we applied this transformation to all of our images, where we used different values of α that define $g(\mathbf{k})$ for each of the m_f states.

[TOTHINK: Need to understand origin of this...]

8.4 Fourier spectroscopy of the Rashba dispersion

We directly measured the 2D dispersion relation using Fourier transform spectroscopy [13] (see Chapter 5). In this technique we considered the evolution of an initial state $|i, \mathbf{k}\rangle$ suddenly subjected to the Raman coupling lasers. This atomic Rabi-type interferometer is analogous to the three-port beam-splitter depicted in

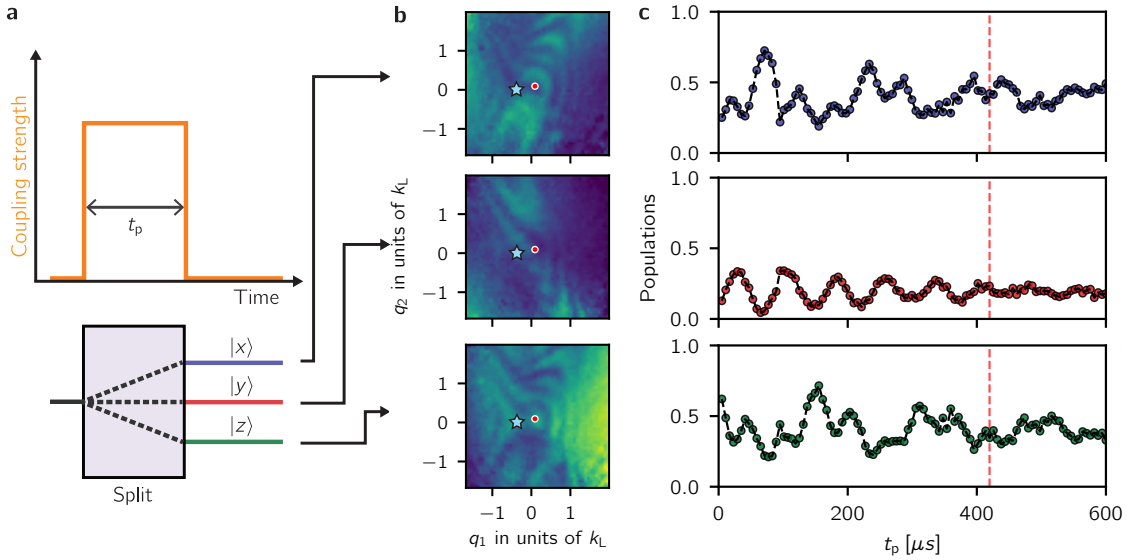


Figure 8.10: **a** Fourier spectroscopy protocol. We applied the Raman lasers for a variable time t_p : a Rabi-type atomic interferometer analogous to a three-port beam splitter. **b** Probabilities as a function of quasimomentum for a fixed Raman pulse time $t_p = 420 \mu s$ **c** Dynamics of the final populations of the $|xyz\rangle$ states with quasimomentum $(q_1, q_2) = (-0.55, -0.18) k_L$ (blue star in panels **b**) after initializing the system in the $|z\rangle$ state.

Figure 8.10b. During a pulse time t_p we followed the dynamics of the populations in the $|xyz\rangle$ states which evolved with oscillatory components proportional to $\sum_{j \neq n} a_{n,j}(\mathbf{q}) \cos([E_n(\mathbf{q}) - E_j(\mathbf{q})]t_p/\hbar)$, with frequencies determined by the eigenenergy differences $E_n - E_j$. Figure 8.10c shows the momentum dependent populations for a fixed pulse time t_p and Figure 8.10d shows representative final populations as a function of t_p for a fixed quasimomentum state. We Fourier transformed the populations with respect to t_p and for a given quasimomentum state for a total of 9 state, all of them with the same \mathbf{q} accounting for each of the three initial $|xyz\rangle$ states that was then split into 3 states. Figure 8.11 shows the PSD computed for each of the 9 states for planes of constant q_1 . The amplitude of the oscillatory components depends on the overlap integral between the initial state and the Raman dressed states as was discussed in Chapter 5 so sampling all these states gave us access to a wider range of measurable frequencies. The spectral maps in Figure 8.12b were produced by averaging the PSDs from the 9 different states using \bar{n} , the mean population in t_p , as a weight:

$$\text{PSD}^{(\text{mean})}(\mathbf{q}) = \frac{\sum_{i,j} \text{PSD}_{i,j}(\mathbf{q}) \bar{n}_{i,j}(\mathbf{q})}{\sum_{i,j} \bar{n}_{i,j}(\mathbf{q})}, \quad (8.11)$$

where the indices i, j represent the different states of the grid shown in Figure 8.11. The extrema in the spectral maps are the energy differences $E_n - E_j$ in the engineered dispersion (Figure 8.10a). The combined maps show the presence of a single Dirac point in the Rashba subspace, evidenced by the gap closing near $\mathbf{q} = 0$ and the photon-like lower branch. The dashed curves correspond to the energy differences computed for our system using the dispersions shown in Figure 8.12a, and are in clear agreement with our experiment.

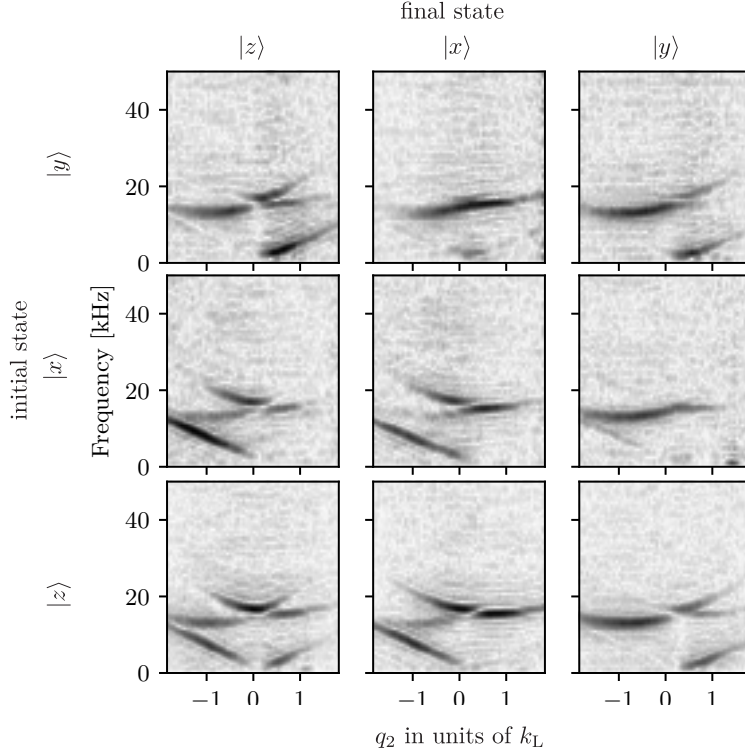


Figure 8.11: PSD of all the analyzed states as a function of q_2 for fixed $q_1 = 0.18 k_L$. The different overlaps between the initial state, the Raman dressed states and the measured final state result in peaks with different amplitudes.

8.5 Quantum state tomography with Ramsey interferometer

The Fourier spectroscopy measurement confirmed our quantum engineering of the Rashba Hamiltonian. However, the energies shed no light on the topology of the different branches of the dispersion, which instead requires knowledge of the eigenstates. The Berry curvature present in the definition of the Chern number (Equation 7.11) can be derived from the Berry's connection $\mathbf{A}_n(\mathbf{q}) = i \langle \Psi_n(\mathbf{q}) | \nabla_{\mathbf{q}} | \Psi_n(\mathbf{q}) \rangle$, which as discussed in Chapter 7 behaves much like a vector potential in classical electromagnetism. The Berry curvature $\boldsymbol{\Omega}_n(\mathbf{q}) = \nabla_{\mathbf{q}} \times \mathbf{A}(\mathbf{q})$ is the associated magnetic field and the flux through any surface is the line integral of $\mathbf{A}(\mathbf{q})$ along its

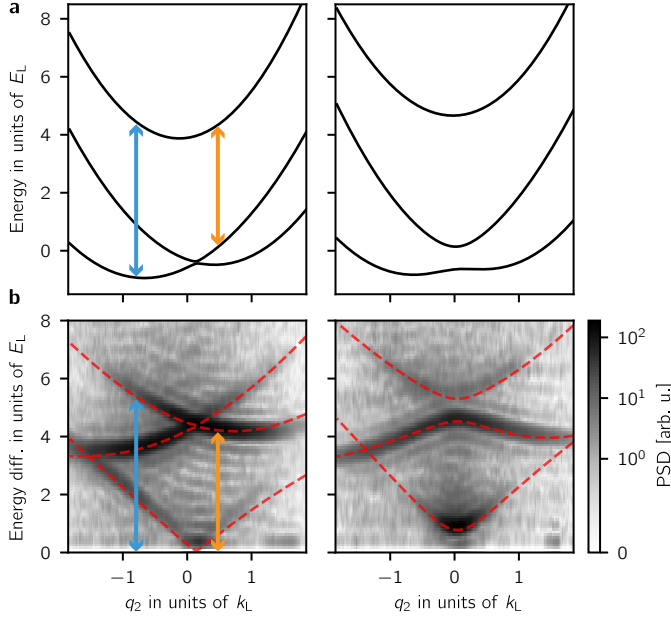


Figure 8.12: **a** Predicted dispersion relation as a function of q_2 for fixed $q_1 = -0.09 k_L$ (left) and $0.65 k_L$ (right), computed for the experiment parameters. The energy differences between the branches enclosing the vertical arrows appear as peaks in the spectral maps below. **b** Power spectral density (PSD) for the same parameters as above which we obtained by Fourier transforming the populations in the $|xyz\rangle$ states with respect to t_p . The dashed lines correspond to the energy differences computed using the dispersion curves on the top panel.

boundary, after neglecting the contributions of Dirac strings which we will discuss later. Using the expression for the Raman dressed eigenstates from Equation 8.9 we obtain

$$\mathbf{A}_n(\mathbf{q}) = - \sum_{j \in \{x,y,z\}} a_{n,j}(\mathbf{q}) \nabla_q \phi_{n,j}(\mathbf{q}), \quad (8.12)$$

which depends on both the phase and amplitude of the wave function. We obtained $a_{n,j}(\mathbf{q})$ and $\phi_{n,j}(\mathbf{q})$ using a three-arm time-domain Ramsey interferometer, implementing a variant of quantum state tomography [90, 91]. The use of a multi-path interferometer allowed us to transduce information about phases into state populations, which we readily obtained from absorption images.

Figure 8.13 shows our experimental protocol which I will describe in detail in more detail in the following section. We adiabatically mapped an initial $|j, \mathbf{k}\rangle$ state into a corresponding eigenstate $|n, \mathbf{q} = \mathbf{k} + \mathbf{k}_j\rangle$, either in the topologically trivial highest dispersion branch ($n = 3$) or in the topological ground branch ($n = 1$) by dynamically tailoring both the Raman coupling strength and detuning. We suddenly turned off the Raman coupling, thereby allowing the three bare state components of the Rashba eigenstates to undergo free evolution for a time t_{free} , constituting the three arms of our time-domain interferometer. Finally we applied a three-port beam

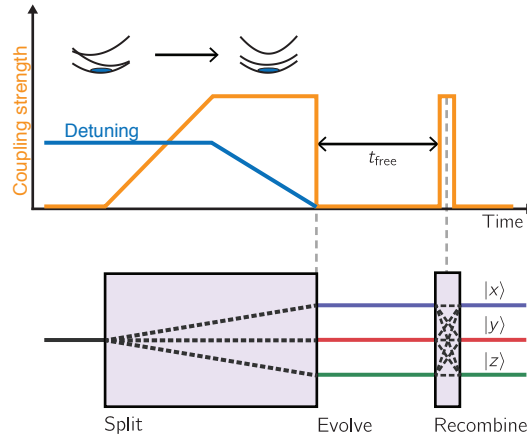


Figure 8.13: Experimental protocol for three-arm Ramsey interferometer (not to scale). (Top) We started with atoms in state $|z, y, \mathbf{q}_i = \mathbf{k} + \mathbf{k}_j\rangle$ and with detuning $\delta_y = \pm 5 E_L$ and $\delta_z = \pm 5 E_L$. We ramped the Raman lasers on in $750 \mu\text{s}$ and then ramped the detuning to nominally zero. We let the system evolve in the dark for times between $5 \mu\text{s}$ and $400 \mu\text{s}$, followed by a $25 \mu\text{s}$ Raman pulse. (Bottom) The implemented experimental protocol was equivalent to a three-arm interferometer that split an initial state into three final states with amplitudes related to the initial wave function phases.

splitter using a brief Raman ‘recombination’ pulse to interfere the three arms.

8.5.1 Wave function evolution in Ramsey interferometer

Rashba dressed state preparation: We started with $|xyz\rangle$ states at different coupling strength $\Omega_{\text{RF}}/\pi 2 \pm 20 \text{ kHz}$, such that the energies of the $|z\rangle$ and $|y\rangle$ states were shifted by about $\pm 18.8 \text{ kHz}$. We used the same Raman frequencies as described earlier and therefore the change in the $|xyz\rangle$ state eigenenergies corresponded to non-zero δ_z and δ_y in Equation 8.8. We chose the detuning such that the initial state had a large overlap with either the $n = 1$ or the $n = 3$ eigenstates of Equation 8.8. We then ramped on the Raman coupling in $750 \mu\text{s}$, adiabatically mapping the $|z\rangle$ and $|y\rangle$ states into the $n = 1$ or $n = 3$ eigenstates. Because our only experimental knob for dynamically changing the detuning was Ω_{RF} we could not control δ_x so when we initialized the system in $|x\rangle$ the the final dressed state always corresponded to the $n = 2$ branch. After turning on the Raman we ramped Ω_{RF} to its final value in 1 ms , effectively ramping δ_z and δ_y close to zero. This detuning ramp had the additional effect of moving the location Dirac point through the atoms, thereby creating a trajectory where the state preparation was not adiabatic. This trajectory depended on the sign of the detuning ramp and combining data from different initial states allowed us to exclude the Dirac point trajectories. Near the final location of the Dirac point the state preparation can not be adiabatic

regardless of the initial state or detuning used for the ground state preparation. Figure 8.14a shows and example a TOF image of atoms initially prepared in the $|y\rangle$ state with the $\delta_{\text{a},y}$ such that the state is mapped to the $n = 1$ eigenstate, the Dirac point is initially located near the lower left edge of the cloud. We ramped δ_i such that the Dirac point was dragged across the whole cloud leaving lines where non-adiabatic transitions occurred as can be seen in Figure 8.14b. The location of the Dirac point as a function of δ_i can also be directly computed by numerically diagonalizing the SOC Hamiltonian from Equation 8.8. At the end of this stage, the state of the system was described by the eigenstates in Equation 8.9.

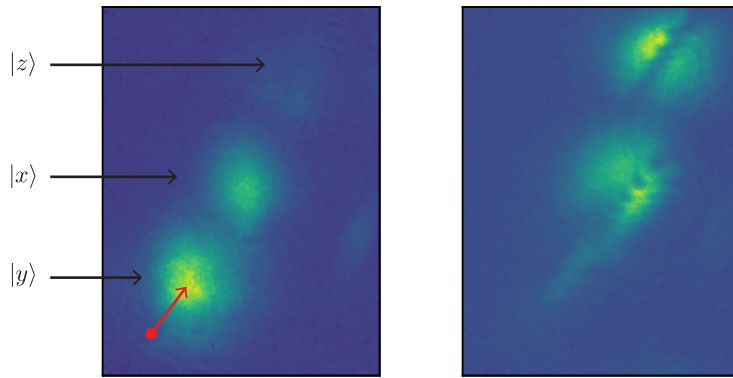


Figure 8.14: **a** We prepared atoms in the $|y\rangle$ state such that they are adiabatically mapped to the ground dispersion branch. **b** We ramped δ_i so that the Dirac point was dragged through the cloud.

Free evolution: We suddenly turned off the Raman coupling, thereby projecting the Raman dressed states back into the $|xyz\rangle$ basis. Each of the $|xyz\rangle$ state represents a different branch of the interferometer and they acquire phases that are proportional to t_{free}

$$|\Psi_n(\mathbf{q})\rangle \rightarrow \sum_{j \in xyz} \sqrt{a_{n,j}(\mathbf{q})} e^{i\phi_{n,j}(\mathbf{q})} e^{-iE_j(\mathbf{q})t_{\text{free}}/\hbar} |j, \mathbf{k} = \mathbf{q} - \mathbf{k}_j\rangle, \quad (8.13)$$

where $E_j(\mathbf{q}) = \hbar^2 \mathbf{q}^2 / 2m$ is the free particle energy. One subtle difference between our interferometer and other types of interferometers is that in our case the phase that we are interested in measuring is imprinted when the state is split. The dynamical phases $E_j(\mathbf{q})t_{\text{free}}/\hbar$ acquired in the different interferometer arms does not contribute to our knowledge of the Rashba eigenstates as they describe the evolution of the system in the absence of Raman dressing.

Recombination pulse: We applied a 25 us Raman pulse that acted as a second beam splitter in our interferometer sequence. The wave function after the

pulse is

$$|\Psi(\mathbf{q})\rangle = \sum_{j,j' \in xyz} \sqrt{a_{n,j}(\mathbf{q})} e^{i(\phi_{n,j}(\mathbf{q}) - E_j(\mathbf{q})t_{\text{free}}/\hbar)} U_{j,j'}(\mathbf{q}) |j, \mathbf{k} = \mathbf{q} - \mathbf{k}_j\rangle, \quad (8.14)$$

where $U_{j,j'}(\mathbf{q}) = |U_{j,j'}(\mathbf{q})| \exp(i\phi_{j,j'}^{(\text{pulse})}(\mathbf{q}))$ is the matrix element of the unitary transformation $\exp(i\hat{H}_{\text{R}}(\mathbf{q})t_{\text{pulse}})$ associated to the Raman pulse. At the end of this procedure, the population in a final state $|l, \mathbf{q}\rangle$ is

$$P_l(\mathbf{q}, t) = \sum_{i \neq j} |U_{l,i}| |U_{j,l}| \sqrt{a_{n,i} a_{n,j}} \cos(\omega_{i,j}(\mathbf{q})t + \phi_{n,i}(\mathbf{q}) - \phi_{n,j}(\mathbf{q}) + \phi_{l,i,j}^{(\text{pulse})}(\mathbf{q})), \quad (8.15)$$

which directly reads out the phase differences, independent of the output port l . Here $\phi_{l,i,j}^{(\text{pulse})} = \phi_{j,l}^{(\text{pulse})} - \phi_{l,i}^{(\text{pulse})}$ is a smoothly varying phase imprinted by the recombination pulse and is independent of \mathbf{q} in the limit of short, strong pulses. The angular frequencies

$$\omega_{i,j}(\mathbf{q}) = \hbar \mathbf{q} \cdot \mathbf{k}_{i,j} / m + \delta_{i,j} \quad (8.16)$$

result from the known free particle kinetic energy, the recoil momenta and detuning $\delta_{i,j}$ from the tripod resonance condition. Figure 8.13b shows the momentum-dependent populations in each output port at fixed $t_{\text{free}} = 160 \mu\text{s}$ and Figure 8.13c shows the populations as a function of t_{free} for a representative quasimomentum state $(q_1, q_2) = (0.55, -0.92) k_L$.

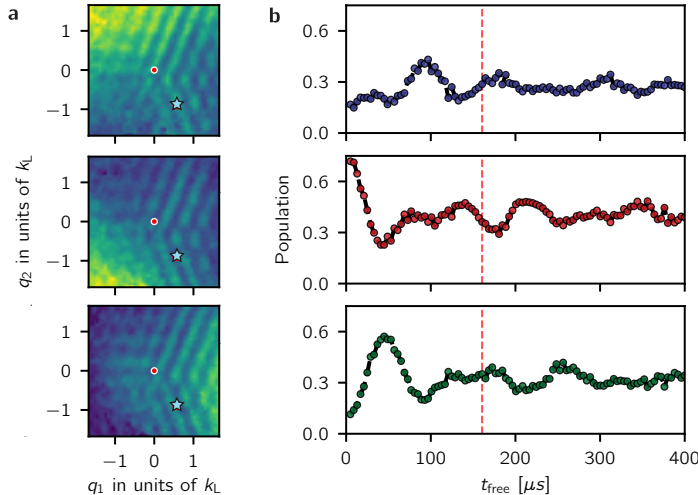


Figure 8.15: **a** Probabilities as a function of quasimomentum for the three output ports of the interferometer at $t_{\text{free}} = 160 \mu\text{s}$ **b** Probabilities as a function of free evolution time t_{free} for an input state with quasimomentum $(q_1, q_2) = (0.55, -0.92) k_L$ indicated by the blue star on **a** and in the topological ground branch ($n = 1$)

We obtained the relative phases $\Delta\phi_{n,i,j,l}(\mathbf{q}) = \phi_{n,i}(\mathbf{q}) - \phi_{n,j}(\mathbf{q}) + \phi_{l,i,j}^{(\text{pulse})}(\mathbf{q})$ from Equation 8.15 by fitting the measured populations to the sum of three cosines

with the known free particle frequencies but unknown amplitudes and phases.

8.5.2 Combining phases from different measurements

We combined the phases $\Delta\phi_{n,i,j,l}(\mathbf{q})$ obtained from fits to six different states (two initial states split into 3 states). Prior to combining all our data we had to take the phase the from the recombination pulse $\phi_{l,i,j}^{(\text{pulse})}(\mathbf{q})$ into account. This phase corresponds to a smooth \mathbf{q} -dependent variation along the Raman recoil axis $\mathbf{k}_{i,j}$ with an additional \mathbf{q} -independent offset that depends on the state index l . The presence of this extra term does change the measured topological index (see Appendix B). We got rid of the state dependent offset by shifting $\Delta\phi_{n,i,j,l}$ by a constant number such that all the individual phase measurements were maximally overlapped. This shift was constant in \mathbf{q} and therefore had no effect on the topological index.

Similar to the Fourier spectroscopy measurements, we performed a weighted average of the fitted relative phases

$$\Delta\phi_{n,i,j}(\mathbf{q}) = \frac{\sum_l \Delta\phi_{n,i,j,l}(\mathbf{q}) w_{i,j,l}(\mathbf{q})}{\sum_l w_{i,j,l}(\mathbf{q})}, \quad (8.17)$$

where the weights are a combination of uncertainties in the fits and the trajectory of the Dirac point during the loading procedure for the case of the topological branch. Figure 8.16 shows an example of two different weight arrays used to combine the phase difference associated to the $z \rightarrow x$ transition $i, j = z, x$ for the topological branch $n = 1$ ($\Delta_{1,z,x}$):

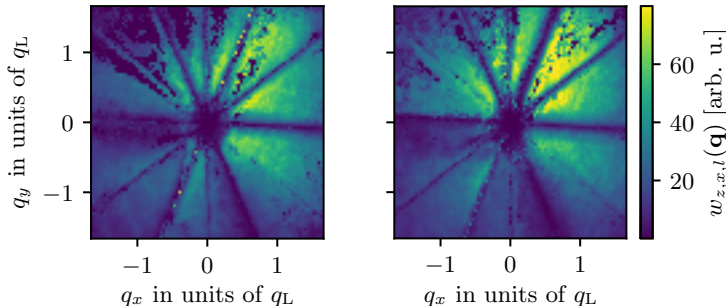


Figure 8.16: Two sample weight arrays $w_{i,j,l}(\mathbf{q})$ for $i, j = z, x$ and atoms prepared in the topological disperion branch. We obtained the weights using the uncertainties from the fits and the trajectory of the Dirac point during the state preparation. We combined the weights and the phase fits from the time dependance $\Delta_{n,i,j,l}$ using Equation 8.17 to obtain the phase maps displayed in Figure [TODO: make figure of all phase maps?]

The ‘spokes’ in the weight arrays correspond to high uncertainty regions. This uncertainty comes of our inability to resolve the phases of low frequencies $\omega_{ij}(\mathbf{q})$

as well as when two different frequencies $\omega_{ij}(\mathbf{q})$ and $\omega_{i'j'}(\mathbf{q})$ are close to each other which is limited by the largest value of t_{free} in the experiment.

8.5.3 Measuring the topological index

We recovered the phases $\phi_{n,j}$ of the full spinor wave function from the relative phases $\Delta\phi_{n,i,j}(\mathbf{q})$ by choosing a particular gauge such that $\phi_{n,0} = 0$. We then used the values of $a_{n,i}$ obtained from measuring the populations in the $|xyz\rangle$ states at $t_{\text{free}} = 0$ in combination with the phases of the wave function to compute the Berry connection [92]. Figure 8.17b shows the three phase differences as a function of polar angle for a loop of radius $q \approx 0.77 k_L$ for both the topological and non-topological branches. In addition to the smooth variations induced by the recombination which are present in both columns, the phases of the topological branch have two π valued jumps that lead to non-zero Berry phases when the Berry connection is integrated along a closed loop in momentum space. Figure 8.17c shows the integrated Berry phase as a function of loop radius. As mentioned earlier the largest value of t_{free} limits how well we can resolve the phases of small frequencies and this is reflected in the large variation in the Berry phase depicted in the shaded region of Figure 8.17c near $q = 0$. For loops with $q > 0.4 k_L$ we obtain an integrated Berry phase that suggests an asymptotic Chern number of $\Phi_B/2\pi = 0.01(1)$ for the non-topological branch and $\Phi_B/2\pi = 0.5(5)$ for the topological branch. However, Berry's phase measurements including ours includes the (potential) contribution of any Dirac strings traversing the integration area. In our system, these are possible at the Dirac point $*$, and each contributes $\pm 2\pi$ to Φ_B as was discussed in Chapter 7.6. Even with this 2π ambiguity we are able to associate a half-integer Chern number with the topological branch, which is possible only for a topological dispersion branch in the continuum.

8.6 Conclusion

In conventional lattices — for example graphene, or the topological Haldane model — it is well established that Dirac points each contribute a Berry's phase of $\Phi_B/2\pi = \pm 1/2$ [93], but crystalline materials conspire for these to appear in pairs [94], always delivering integer Chern numbers. In contrast, our continuum system contains a single Dirac point, resulting in a non-integer Chern number. This leads to intriguing questions about edge states at interfaces with non-integer Chern numbers with non-integer Chern number differences. Initial studies in the context of electromagnetic waveguides [95] and atmospheric waves [50] have applied Chern invariants and the bulk-edge correspondence to continuous media.

While the true Rashba Hamiltonian features a ring of degenerate eigenstates, our implementation including the quadratic and cubic Dresselhaus-like SOC lifts this macroscopic degeneracy giving three nearly degenerate minima [78]. Already these three minima could allow the study of rich ground state physics in many body systems of bosons, for example the formation of fragmented BECs [81] when

the system does not condense into a single-particle state. Furthermore, the use of additional spin states or larger Raman couplings can partially restore this degeneracy allowing the possible realization of fractional Hall like states [96].

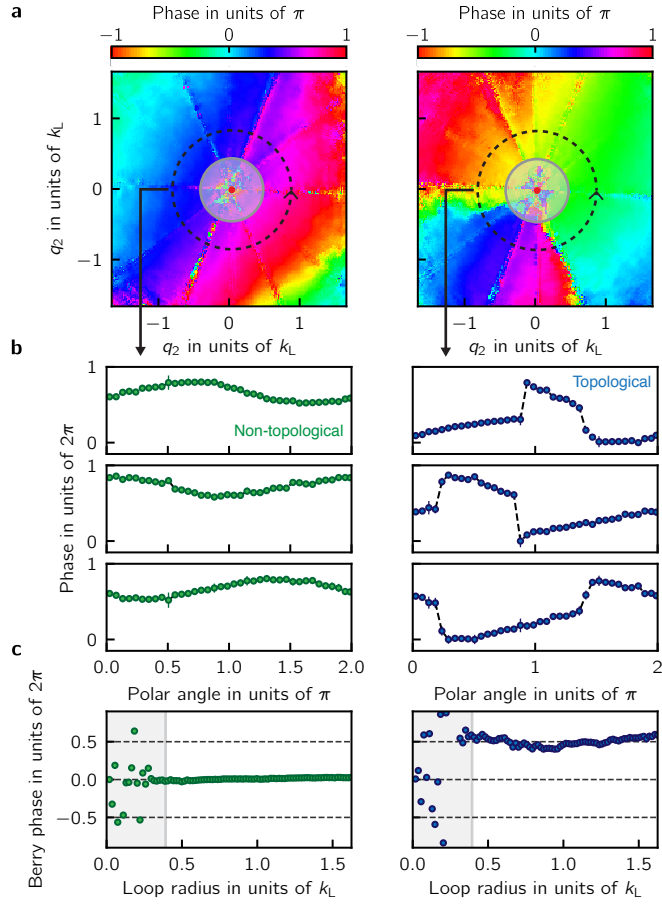


Figure 8.17: Topological invariants from quantum state tomography, for the non-topological branch ($n = 3$, left) and the topological branch ($n = 1$, right). **a** Phase differences as a function of quasimomentum from the $z \rightarrow x$ transition. **b** Phase differences as a function of polar angle for a loop radius $0.77 k_L$ from the $z \rightarrow x$ (top), $x \rightarrow y$ (middle) and $y \rightarrow z$ (bottom) transitions. The phases associated to the topological branch are characterized by two π valued discontinuities. Each row of phases was shifted by a constant value so that the three rows of phases share the same vertical axis. All phases shown here were binned and averaged using the fit uncertainties as weights. **c** Inferred Chern number as a function of loop radius. For loops with $q > 0.4 k_L$ we obtained an integrated Berry phase and asymptotic Chern number of $\Phi_B/2\pi = 0.01(1)$ for the non-topological branch and $\Phi_B/2\pi = 0.5(5)$ for the topological branch.

Chapter 9: Conclusions and outlook

The end!

Chapter 9: Realization of a fractional period adiabatic superlattice

This was an intermediate step to engineer topological matter with a lattice.

Appendix A: Full derivation of the Hamiltonian for Raman coupled $|xyz\rangle$ states

Appendix B: New Apparatus

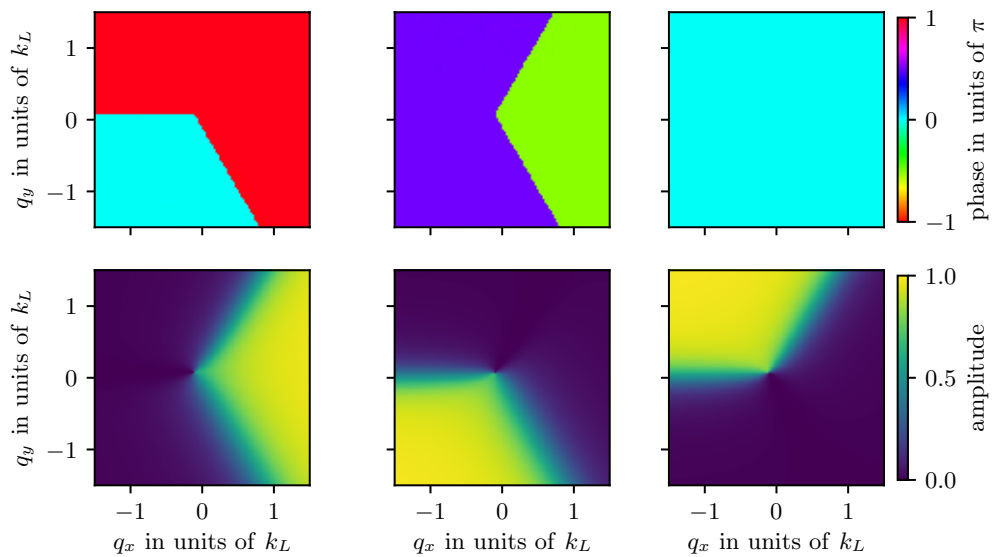


Figure B.1: **a** Probabilities as a function of quasimomentum for the three output ports of the interferometer at $t_{\text{free}} = 160 \mu\text{s}$ **b** Probabilities as a function of free evolution time t_{free} for an input state with quasimomentum $(q_1, q_2) = (0.55, -0.92) k_L$ indicated by the blue star on **a** and in the topological ground branch ($n = 1$)

B.1 Water cooling stuff

B.2 Electrical installation

B.3 New Rb ‘oven’

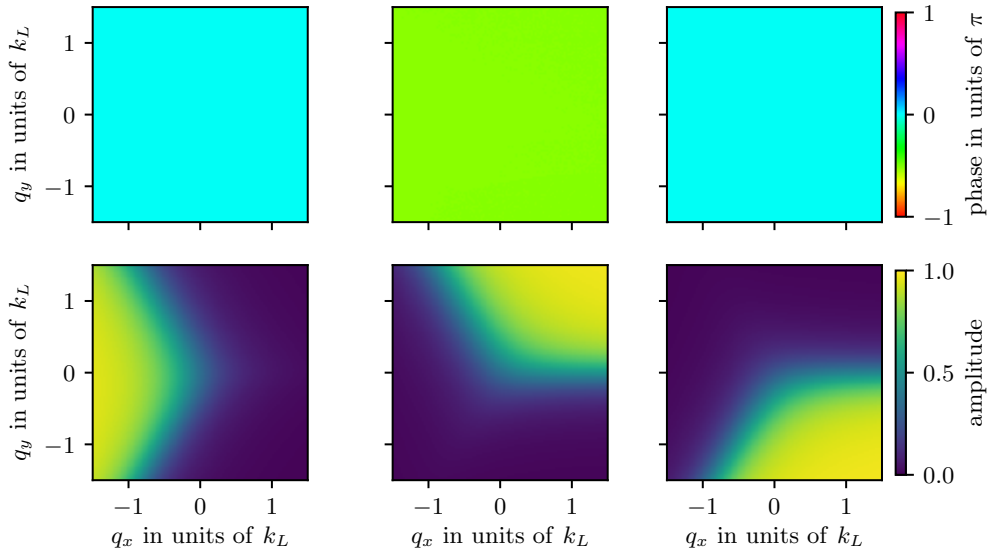


Figure B.2: **a** Probabilities as a function of quasimomentum for the three output ports of the interferometer at $t_{\text{free}} = 160 \mu\text{s}$ **b** Probabilities as a function of free evolution time t_{free} for an input state with quasimomentum $(q_1, q_2) = (0.55, -0.92) k_L$ indicated by the blue star on **a** and in the topological ground branch ($n = 1$)

Bibliography

- [1] Harold J. Metcalf and Peter van der Straten. Deceleration of an Atomic Beam. In Harold J. Metcalf and Peter van der Straten, editors, *Laser Cooling and Trapping*, Graduate Texts in Contemporary Physics, pages 73–86. Springer New York, New York, NY, 1999.
- [2] J. Stark. Beobachtungen über den Effekt des elektrischen Feldes auf Spektrallinien. I. Quereffekt. *Annalen der Physik*, 348(7):965–982, 1914.
- [3] L. J. LeBlanc, M. C. Beeler, K. Jiménez-García, A. R. Perry, S. Sugawa, R. A. Williams, and I. B. Spielman. Direct observation of zitterbewegung in a Bose–Einstein condensate. *New Journal of Physics*, 15(7):073011, 2013.
- [4] D. L. Campbell, R. M. Price, A. Putra, A. Valdes-Curiel, D. Trypogeorgos, and I. B. Spielman. Magnetic phases of spin-1 spin–orbit-coupled Bose gases. *Nature Communications*, 7:10897, March 2016.
- [5] K. Jiménez-García, L. J. LeBlanc, R. A. Williams, M. C. Beeler, C. Qu, M. Gong, C. Zhang, and I. B. Spielman. Tunable spin-orbit coupling via strong driving in ultracold-atom systems. *Phys. Rev. Lett.*, 114:125301, Mar 2015.
- [6] Doppler-Limited Absorption and Fluorescence Spectroscopy with Lasers. In Wolfgang Demtröder, editor, *Laser Spectroscopy: Vol. 2 Experimental Techniques*, pages 1–75. Springer Berlin Heidelberg, Berlin, Heidelberg, 2008.
- [7] I. I. Rabi. Space Quantization in a Gyrating Magnetic Field. *Physical Review*, 51(8):652–654, April 1937.
- [8] Lawrence W. Cheuk, Ariel T. Sommer, Zoran Hadzibabic, Tarik Yefsah, Waseem S. Bakr, and Martin W. Zwierlein. Spin-Injection Spectroscopy of a Spin-Orbit Coupled Fermi Gas. *Physical Review Letters*, 109(9):095302, 2012.

- [22] D. Trypogeorgos, A. Valdés-Curiel, N. Lundblad, and I. B. Spielman. Synthetic clock transitions via continuous dynamical decoupling. *Physical Review A*, 97(1):013407, January 2018.
- [23] R. P. Anderson, M. J. Kewming, and L. D. Turner. Continuously observing a dynamically decoupled spin-1 quantum gas. *Physical Review A*, 97(1):013408, January 2018.
- [24] E. L. Hahn. Spin Echoes. *Physical Review*, 80(4):580–594, November 1950.
- [25] Lorenza Viola and Seth Lloyd. Dynamical suppression of decoherence in two-state quantum systems. *Phys. Rev. A*, 58(4):2733–2744, October 1998.
- [26] I. Cohen, N. Aharon, and A. Retzker. Continuous dynamical decoupling utilizing time-dependent detuning. *Fortschr. Phys.*, 65(6-8):n/a–n/a, June 2017.
- [27] F. F. Fanchini, J. E. M. Hornos, and R. d J. Napolitano. Continuously decoupling single-qubit operations from a perturbing thermal bath of scalar bosons. *Physical Review A*, 75(2), February 2007. arXiv: quant-ph/0611188.
- [28] N. Aharon, I. Cohen, F. Jelezko, and A. Retzker. Fully robust qubit in atomic and molecular three-level systems. *New J. Phys.*, 18(12):123012, 2016.
- [29] Michael J. Biercuk, Hermann Uys, Aaron P. VanDevender, Nobuyasu Shiga, Wayne M. Itano, and John J. Bollinger. Optimized dynamical decoupling in a model quantum memory. *Nature*, 458(7241):996–1000, April 2009.
- [30] J.-M. Cai, B. Naydenov, R. Pfeiffer, L. P. McGuinness, K. D. Jahnke, F. Jelezko, M. B. Plenio, and A. Retzker. Robust dynamical decoupling with concatenated continuous driving. *New Journal of Physics*, 14(11):113023, November 2012. arXiv: 1111.0930.
- [31] A. Bermudez, P. O. Schmidt, M. B. Plenio, and A. Retzker. Robust trapped-ion quantum logic gates by continuous dynamical decoupling. *Phys. Rev. A*, 85(4):040302, April 2012.
- [32] I. Baumgart, J.-M. Cai, A. Retzker, M. B. Plenio, and Ch. Wunderlich. Ultrasensitive magnetometer using a single atom. *Phys. Rev. Lett.*, 116:240801, Jun 2016.
- [33] G. A. Kazakov and T. Schumm. Magic radio-frequency dressing for trapped atomic microwave clocks. *Phys. Rev. A*, 91(2):023404, February 2015.
- [34] L. Sárkány, P. Weiss, H. Hattermann, and J. Fortágh. Controlling the magnetic-field sensitivity of atomic-clock states by microwave dressing. *Phys. Rev. A*, 90(5):053416, November 2014.

- [35] Arne Laucht, Rachpon Kalra, Stephanie Simmons, Juan P. Dehollain, Juha T. Muhonen, Fahd A. Mohiyaddin, Solomon Freer, Fay E. Hudson, Kohei M. Itoh, David N. Jamieson, Jeffrey C. McCallum, Andrew S. Dzurak, and A. Morello. A dressed spin qubit in silicon. *Nat Nano*, 12(1):61–66, January 2017.
- [36] D. Farfurnik, N. Aharon, I. Cohen, Y. Hovav, A. Retzker, and N. Bar-Gill. Experimental realization of time-dependent phase-modulated continuous dynamical decoupling. *arXiv:1704.07582 [quant-ph]*, April 2017. arXiv: 1704.07582.
- [37] Atsushi Noguchi, Shinsuke Haze, Kenji Toyoda, and Shinji Urabe. Generation of a Decoherence-Free Entangled State Using a Radio-Frequency Dressed State. *Phys. Rev. Lett.*, 108(6):060503, February 2012.
- [38] D. Andrew Golter, Thomas K. Baldwin, and Hailin Wang. Protecting a Solid-State Spin from Decoherence Using Dressed Spin States. *Phys. Rev. Lett.*, 113(23):237601, December 2014.
- [39] N. Timoney, I. Baumgart, M. Johanning, A. F. Varón, M. B. Plenio, A. Retzker, and Ch Wunderlich. Quantum gates and memory using microwave-dressed states. *Nature*, 476(7359):185–188, August 2011.
- [40] S. C. Webster, S. Weidt, K. Lake, J. J. McLoughlin, and W. K. Hensinger. Simple Manipulation of a Microwave Dressed-State Ion Qubit. *Phys. Rev. Lett.*, 111(14):140501, October 2013.
- [41] A. Barfuss, J. Teissier, E. Neu, A. Nunnenkamp, and P. Maletinsky. Strong mechanical driving of a single electron spin. *Nat Phys*, 11(10):820–824, October 2015.
- [42] S. Rohr, E. Dupont-Ferrier, B. Pigeau, P. Verlot, V. Jacques, and O. Arcizet. Synchronizing the Dynamics of a Single Nitrogen Vacancy Spin Qubit on a Parametrically Coupled Radio-Frequency Field through Microwave Dressing. *Phys. Rev. Lett.*, 112(1):010502, January 2014.
- [43] Nigel R. Cooper and Jean Dalibard. Reaching Fractional Quantum Hall States with Optical Flux Lattices. *Physical Review Letters*, 110(18):185301, April 2013.
- [44] Gediminas Juzeliūnas, Julius Ruseckas, and Jean Dalibard. Generalized Rashba-Dresselhaus spin-orbit coupling for cold atoms. *Phys. Rev. A*, 81(5):053403, May 2010.
- [45] D. Bacon, J. Kempe, D. A. Lidar, and K. B. Whaley. Universal Fault-Tolerant Quantum Computation on Decoherence-Free Subspaces. *Phys. Rev. Lett.*, 85(8):1758–1761, August 2000.
- [46] Pablo Solano, Jeffrey A. Grover, Jonathan E. Hoffman, Sylvain Ravets, Fredrik K. Fatemi, Luis A. Orozco, and Steven L. Rolston. Chapter Seven

- Optical Nanofibers: A New Platform for Quantum Optics. In Chun C. Lin and Susanne F. Yelin Ennio Arimondo, editor, *Advances In Atomic, Molecular, and Optical Physics*, volume 66, pages 439–505. Academic Press, 2017. DOI: 10.1016/bs.aamop.2017.02.003.
- [47] Ze-Liang Xiang, Sahel Ashhab, J. Q. You, and Franco Nori. Hybrid quantum circuits: Superconducting circuits interacting with other quantum systems. *Rev. Mod. Phys.*, 85(2):623–653, April 2013.
 - [48] M. Z. Hasan and C. L. Kane. Colloquium: Topological insulators. *Reviews of Modern Physics*, 82(4):3045–3067, November 2010.
 - [49] Tomoki Ozawa, Hannah M. Price, Alberto Amo, Nathan Goldman, Mohammad Hafezi, Ling Lu, Mikael C. Rechtsman, David Schuster, Jonathan Simon, Oded Zilberberg, and Iacopo Carusotto. Topological photonics. *Reviews of Modern Physics*, 91(1):015006, March 2019.
 - [50] Pierre Delplace, J. B. Marston, and Antoine Venaille. Topological origin of equatorial waves. *Science*, 358(6366):1075–1077, November 2017.
 - [51] V. Peano, C. Brendel, M. Schmidt, and F. Marquardt. Topological Phases of Sound and Light. *Physical Review X*, 5(3):031011, July 2015.
 - [52] Zhaoju Yang, Fei Gao, Xihang Shi, Xiao Lin, Zhen Gao, Yidong Chong, and Baile Zhang. Topological Acoustics. *Physical Review Letters*, 114(11):114301, March 2015.
 - [53] N. R. Cooper, J. Dalibard, and I. B. Spielman. Topological bands for ultracold atoms. *Rev. Mod. Phys.*, 91:015005, Mar 2019.
 - [54] D. J. Thouless, M. Kohmoto, M. P. Nightingale, and M. den Nijs. Quantized Hall Conductance in a Two-Dimensional Periodic Potential. *Physical Review Letters*, 49(6):405–408, August 1982.
 - [55] F. D. M. Haldane. Model for a Quantum Hall Effect without Landau Levels: Condensed-Matter Realization of the "Parity Anomaly". *Physical Review Letters*, 61(18):2015–2018, October 1988.
 - [56] C. L. Kane and E. J. Mele. $\{Z\}_2$ Topological Order and the Quantum Spin Hall Effect. *Physical Review Letters*, 95(14):146802, September 2005.
 - [57] D. B. Newell, F. Cabiati, J. Fischer, K. Fujii, S. G. Karshenboim, H. S. Margolis, E. de Mirandés, P. J. Mohr, F. Nez, K. Pachucki, T. J. Quinn, B. N. Taylor, M. Wang, B. M. Wood, and Z. Zhang. The CODATA 2017 values of h, e, k, and N A for the revision of the SI. *Metrologia*, 55(1):L13–L16, January 2018.
 - [58] Chetan Nayak, Steven H. Simon, Ady Stern, Michael Freedman, and Sankar Das Sarma. Non-Abelian anyons and topological quantum computation. *Reviews of Modern Physics*, 80(3):1083–1159, September 2008.

- [59] Yu A. Bychkov and E. I. Rashba. Oscillatory effects and the magnetic susceptibility of carriers in inversion layers. *Journal of Physics C: Solid State Physics*, 17(33):6039, 1984.
- [60] Eduardo Nahmad-Achar. *Differential Topology and Geometry with Applications to Physics*. 2053-2563. IOP Publishing, 2018.
- [61] L. Landau. The Theory of Phase Transitions. *Nature*, 138(3498):840–841, November 1936.
- [62] K. v. Klitzing, G. Dorda, and M. Pepper. New Method for High-Accuracy Determination of the Fine-Structure Constant Based on Quantized Hall Resistance. *Physical Review Letters*, 45(6):494–497, August 1980.
- [63] David Tong. Lectures on the Quantum Hall Effect. *arXiv:1606.06687 [cond-mat, physics:hep-th]*, June 2016. arXiv: 1606.06687.
- [64] Barry Simon. Holonomy, the Quantum Adiabatic Theorem, and Berry’s Phase. *Physical Review Letters*, 51(24):2167–2170, December 1983.
- [65] Mikio Nakahara. CRC Press, New York, NY, 2003.
- [66] Berry Michael Victor. Quantal phase factors accompanying adiabatic changes. *Proceedings of the Royal Society of London. A. Mathematical and Physical Sciences*, 392(1802):45–57, March 1984.
- [67] Y. Aharonov and D. Bohm. Significance of Electromagnetic Potentials in the Quantum Theory. *Physical Review*, 115(3):485–491, August 1959.
- [68] G. Dresselhaus. Spin-Orbit Coupling Effects in Zinc Blende Structures. *Physical Review*, 100(2):580–586, October 1955.
- [69] Dirac Paul Adrien Maurice. Quantised singularities in the electromagnetic field,. *Proceedings of the Royal Society of London. Series A, Containing Papers of a Mathematical and Physical Character*, 133(821):60–72, September 1931.
- [70] Ralph M. Kaufmann, Dan Li, and Birgit Wehefritz-Kaufmann. Notes on topological insulators. *Reviews in Mathematical Physics*, 28(10):1630003, November 2016. arXiv: 1501.02874.
- [71] Hirokazu Miyake, Georgios A. Siviloglou, Colin J. Kennedy, William Cody Burton, and Wolfgang Ketterle. Realizing the Harper Hamiltonian with Laser-Assisted Tunneling in Optical Lattices. *Physical Review Letters*, 111(18):185302, October 2013.
- [72] M. Aidelsburger, M. Atala, M. Lohse, J. T. Barreiro, B. Paredes, and I. Bloch. Realization of the Hofstadter Hamiltonian with Ultracold Atoms in Optical Lattices. *Physical Review Letters*, 111(18):185301, October 2013.

- [73] Gregor Jotzu, Michael Messer, Rémi Desbuquois, Martin Lebrat, Thomas Uehlinger, Daniel Greif, and Tilman Esslinger. Experimental realization of the topological Haldane model with ultracold fermions. *Nature*, 515(7526):237–240, November 2014.
- [74] H.-I Lu, M. Schemmer, L. M. Aycock, D. Genkina, S. Sugawa, and I. B. Spielman. Geometrical pumping with a bose-einstein condensate. *Phys. Rev. Lett.*, 116:200402, May 2016.
- [75] M. Lohse, C. Schweizer, O. Zilberberg, M. Aidelsburger, and I. Bloch. A Thouless quantum pump with ultracold bosonic atoms in an optical superlattice. *Nature Physics*, 12(4):350–354, April 2016.
- [76] Zhan Wu, Long Zhang, Wei Sun, Xiao-Tian Xu, Bao-Zong Wang, Si-Cong Ji, Youjin Deng, Shuai Chen, Xiong-Jun Liu, and Jian-Wei Pan. Realization of two-dimensional spin-orbit coupling for Bose-Einstein condensates. *Science*, 354(6308):83–88, October 2016.
- [77] Wei Sun, Bao-Zong Wang, Xiao-Tian Xu, Chang-Rui Yi, Long Zhang, Zhan Wu, Youjin Deng, Xiong-Jun Liu, Shuai Chen, and Jian-Wei Pan. Highly Controllable and Robust 2d Spin-Orbit Coupling for Quantum Gases. *Physical Review Letters*, 121(15):150401, October 2018.
- [78] D. L. Campbell, G. Juzeliūnas, and I. B. Spielman. Realistic Rashba and Dresselhaus spin-orbit coupling for neutral atoms. *Physical Review A*, 84(2):025602, August 2011.
- [79] Lianghui Huang, Zengming Meng, Pengjun Wang, Peng Peng, Shao-Liang Zhang, Liangchao Chen, Donghao Li, Qi Zhou, and Jing Zhang. Experimental realization of two-dimensional synthetic spin-orbit coupling in ultracold Fermi gases. *Nature Physics*, 12(6):540–544, June 2016.
- [80] Zengming Meng, Lianghui Huang, Peng Peng, Donghao Li, Liangchao Chen, Yong Xu, Chuanwei Zhang, Pengjun Wang, and Jing Zhang. Experimental Observation of a Topological Band Gap Opening in Ultracold Fermi Gases with Two-Dimensional Spin-Orbit Coupling. *Physical Review Letters*, 117(23):235304, December 2016.
- [81] Tudor D. Stanescu, Brandon Anderson, and Victor Galitski. Spin-orbit coupled Bose-Einstein condensates. *Physical Review A*, 78(2):023616, August 2008.
- [82] Tigran A. Sedrakyan, Alex Kamenev, and Leonid I. Glazman. Composite fermion state of spin-orbit-coupled bosons. *Physical Review A*, 86(6):063639, December 2012.
- [83] Hui Hu, Lei Jiang, Xia-Ji Liu, and Han Pu. Probing Anisotropic Superfluidity in Atomic Fermi Gases with Rashba Spin-Orbit Coupling. *Physical Review Letters*, 107(19):195304, November 2011.

- [84] Victor Galitski and Ian B. Spielman. Spin-orbit coupling in quantum gases. *Nature*, 494(7435):49–54, February 2013.
- [85] N. Goldman, G. Juzeliūnas, P. Öhberg, and I. B. Spielman. Light-induced gauge fields for ultracold atoms. *Reports on Progress in Physics*, 77(12):126401, November 2014.
- [86] Tudor D. Stanescu and Victor Galitski. Spin relaxation in a generic two-dimensional spin-orbit coupled system. *Physical Review B*, 75(12):125307, March 2007.
- [87] Y.-J. Lin, A. R. Perry, R. L. Compton, I. B. Spielman, and J. V. Porto. Rapid production of $\text{\^87}\text{Rb}$ Bose-Einstein condensates in a combined magnetic and optical potential. *Physical Review A*, 79(6):063631, June 2009.
- [88] Satoshi Tojo, Taro Hayashi, Tatsuyoshi Tanabe, Takuya Hirano, Yuki Kawaguchi, Hiroki Saito, and Masahito Ueda. Spin-dependent inelastic collisions in spin-2 Bose-Einstein condensates. *Physical Review A*, 80(4):042704, October 2009.
- [89] N. Goldman and J. Dalibard. Periodically Driven Quantum Systems: Effective Hamiltonians and Engineered Gauge Fields. *Physical Review X*, 4(3):031027, 2014.
- [90] N. Fläschner, B. S. Rem, M. Tarnowski, D. Vogel, D.-S. Lühmann, K. Sengstock, and C. Weitenberg. Experimental reconstruction of the Berry curvature in a Floquet Bloch band. *Science*, 352(6289):1091–1094, May 2016.
- [91] Clément Godfrin, Rafik Ballou, Edgar Bonet, Mario Ruben, Svetlana Klyatskaya, Wolfgang Wernsdorfer, and Franck Balestro. Generalized Ramsey interferometry explored with a single nuclear spin qudit. *npj Quantum Information*, 4(1):53, October 2018.
- [92] Takahiro Fukui, Yasuhiro Hatsugai, and Hiroshi Suzuki. Chern Numbers in Discretized Brillouin Zone: Efficient Method of Computing (Spin) Hall Conductances. *Journal of the Physical Society of Japan*, 74(6):1674–1677, June 2005.
- [93] L. Duca, T. Li, M. Reitter, I. Bloch, M. Schleier-Smith, and U. Schneider. An Aharonov-Bohm interferometer for determining Bloch band topology. *Science*, 347(6219):288–292, January 2015.
- [94] H. B. Nielsen and Masao Ninomiya. The Adler-Bell-Jackiw anomaly and Weyl fermions in a crystal. *Physics Letters B*, 130(6):389–396, November 1983.
- [95] Mário G. Silveirinha. Chern invariants for continuous media. *Physical Review B*, 92(12):125153, September 2015.

- [96] Tigran A. Sedrakyan, Victor M. Galitski, and Alex Kamenev. Statistical Transmutation in Floquet Driven Optical Lattices. *Physical Review Letters*, 115(19):195301, November 2015.